With Vibrationally Excited Thiophosgene Molecule and Double-Well Ion Traps

Dmytro Shyshlov
Marquette University

WITH VIBRATIONALLY EXCITED THIOPHOSGENE MOLECULE

AND DOUBLE-WELL ION TRAPS

by

Dmytro Shyshlov

A Dissertation submitted to the faculty of the Graduate School,

Marquette University,

in partial fulfillment of the requirements for

the degree of Doctor of Philosophy

Milwaukee, Wisconsin

December, 2015

ABSTRACT

QUANTUM INFORMATION PROCESSING
WITH VIBRATIONALLY EXCITED THIOPHOSGENE MOLECULE
AND DOUBLE-WELL ION TRAPS

Dmytro Shyshlov, B.S., M.S.

Marquette University, 2015

For practical realization of quantum information processing we need a quantum system that provides reliable preparation of the initial state, high-fidelity quantum gate operations, error tolerance, readout of the result of quantum computation and scalability of the system to increase the number of qubits. In this dissertation we show how these requirements can be addressed for molecular quantum computer. For computational study of quantum information processing with molecules we employ thiophosgene ($SCCl_2$) molecule that has been used as a test system for quantum control experiments [Mol. Phys. **105**, 1999 (2007)]. We investigate the gateway scheme of control in which transitions between the vibrational states that encode qubits are only allowed through the intermediate "gateway" state in the B electronic state. This scheme of control provides reliable preparation of the initial qubit state and allows using UV/vis laser pulses. We demonstrate that high-fidelity quantum gates are possible to achieve in molecular quantum computer. The optimal control theory is employed to obtain a shape of laser pulse that performs CNOT gate with ~0.9999 fidelity. Analysis of frequency profile of the optimal pulse shows that preparation of the high-fidelity computational pulse requires only 64 frequency channels. Error tolerance of the computational pulse is studied by modifying amplitudes and phases of frequency components. It is shown that gate fidelity remains high after small modifications are introduced to the optimal pulse. The scheme of readout of quantum information using quantum beat spectroscopy is proposed. The quantum beat signal is obtained from excitation of the final superposition of the qubit states to a readout state in the B electronic state with a time-delayed pulse. We find that fitting the quantum beat signal with a standard fitting expression produces a phase error and propose a new accurate expression that includes phase correction term. The system of two atomic ions trapped in a double-well potential is also studied as a first step towards scalable quantum computation with trapped molecular ions. The rigorous computational treatment of the system provides explanation of the vibrational energy transfer between the ions in terms of wave packet dynamics in the accurate asymmetric potential.

ACKNOWLEDGEMENTS

Dmytro Shyshlov, B.S., M.S.

LIST OF TABLES

LIST OF FIGURES

Contents

Chapter 1: Introduction

1.1 Quantum control in chemistry

Many molecular processes depend on quantum states of the molecules involved. Influencing these states in a controlled manner with laser radiation makes the considered process more efficient or even can change its outcome completely. This is the objective of study in the field of quantum control [1-5]. This subject continues to develop with the improvement of laser technology, the discovery of new approaches and the discovery of new control scenarios for both experimental and theoretical studies.

One of the most studied chemical problems for quantum control is photodissociation [6-8]. Photodissociation occurs when a chemical bond in a molecule breaks as a result of interaction with photons of light. Photodissociation can often go via various reaction channels that lead to different products. The simplest example is photodissociation of a diatomic molecule. For example, the photodissociation of NaI molecule produces a ground state Na atom or an electronically excited Na* [7]. The branching ratio of products can be controlled. It is possible to do so with two transform-limited ultrafast laser pulses with a time delay between them. The first pulse induces a transition to an electronically excited state of NaI, where molecule evolves during the time between pulses. The second pulse induces a transition back to the ground state of NaI. The control of branching ratios is done by adjusting the time delay between pulses. This scheme is called a pump-dump scheme. A more complicated example is illustrated by Figure 1.1, where a triatomic molecule ABC dissociates into two possible channels:

AB+C or A+BC. Again, in order to achieve a certain dissociation scenario, the time delay between the pump and the dump pulses (vertical yellow lines) varies.

Another application for quantum control is selective product formation with shaped laser pulses. Laser pulses can be tailored to maximize the yield of one of the possible products for a reaction. This was demonstrated in Ref. [9], where a number of reactions with organic compounds were studied. For example, the formation of toluene ($C_6H_5CH_3$) from acetophenone ($C_6H_5COCH_3$) is illustrated in Figure 1.2a. As we can see not only does the CO group have to be cleaved (by breaking two single bonds), but the bond between the methyl and phenyl substituents also must be formed. A strong-field laser pulse was optimized with closed-loop control scheme to enhance desirable reaction outcome over the other two possible pathways (Fig. 1.2b).
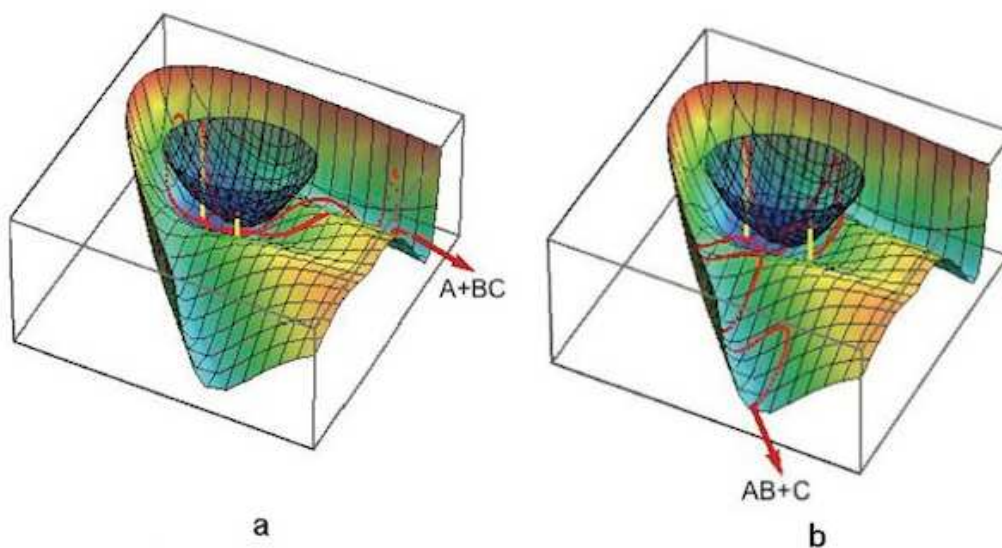
Figure 1.1: Pump-dump scheme of control of dissociation of molecule ABC to products A+BC (a) and AB+C (b). [10]

The ideas of quantum control can also be applied to bimolecular collision processes [11]. It can be used to achieve control of chirality, asymmetric synthesis of chiral products [12], and other chemical processes. The focus of particular interest for this work is quantum control of transitions between molecular vibrational states for the purpose of quantum information processing. Successful implementation of quantum control scenarios may lead to the era of quantum computers [13].

1.2 Quantum computer and quantum information processing

The idea of the quantum computer was introduced by Richard Feynman in 1982. Such a device, if it could be built, would provide extraordinary speed-up for a number of computational problems in cryptography, in data base searches and in simulation of quantum systems [14]. What is the difference between classical and quantum computers? Both perform operations on the information stored in a memory register. Classical computers use bits, memory units that can be in one of two possible states, either "0" or "1". Bits are implemented in practice by using two different levels of voltage or current in

a   b
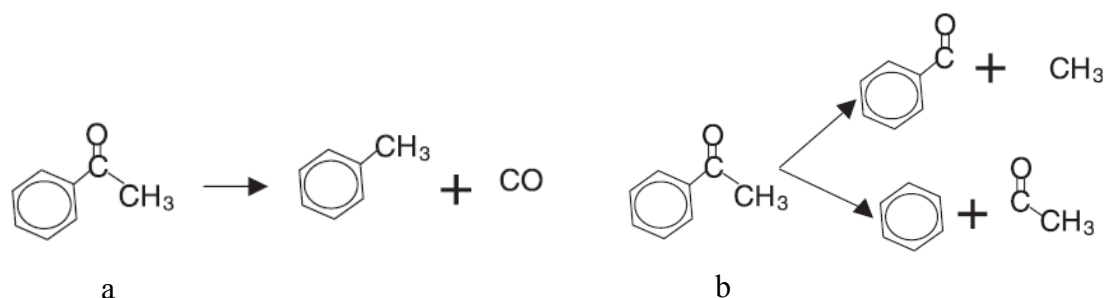
Figure 1.2: Reaction channels of dissociation of acetophenone: (a) with formation of toluene; (b) two side reaction channels. [9]

a circuit. Quantum computers have analogous units – quantum bits, or *qubits*. Qubits can be realized in any quantum two-level system, e.g. electron spin, photon polarization, ground and excited electronic states of atom etc. The state of qubit can be $|0\rangle$ or $|1\rangle$, but, according to the *superposition* principle of quantum mechanics, it also can be in any linear combination of states $|0\rangle$ and $|1\rangle$:

$$|\psi\rangle = \alpha|0\rangle + \beta|1\rangle, \tag{1.2.1}$$

$$\alpha^2 + \beta^2 = 1, \tag{1.2.2}$$

where α and β are complex probability amplitudes, α^2 and β^2 are probabilities or populations of two quantum levels. The superposition state of a qubit can also be notated in a vector form:

$$|\psi\rangle = \begin{pmatrix} \alpha \\ \beta \end{pmatrix}. \tag{1.2.3}$$

For example, equally-weighted superpositions of states $|0\rangle$ and $|1\rangle$ would be described as

$$|\psi\rangle = \begin{pmatrix} \dfrac{1}{\sqrt{2}} \\ \dfrac{1}{\sqrt{2}} \end{pmatrix} \tag{1.2.4}$$

when in phase, and as

$$|\psi\rangle = \begin{pmatrix} \dfrac{1}{\sqrt{2}} \\ -\dfrac{1}{\sqrt{2}} \end{pmatrix}, \tag{1.2.5}$$

when out of phase. In vector notation eigenstates $|0\rangle$ and $|1\rangle$ will look as following:

$$|1\rangle = \begin{pmatrix} 1 \\ 0 \end{pmatrix}, \tag{1.2.6a}$$

$$|0\rangle = \begin{pmatrix} 0 \\ 1 \end{pmatrix}. \qquad\qquad (1.2.6b)$$

Vector notations are useful to describe the states of qubits and their transformations in a concise form, suitable for implementing quantum operators.

Where does the incredible speed-up of quantum computers come from? One of the sources of the speed-up is quantum parallelism, which is related to the superposition principle illustrated above. This feature allows quantum computers to calculate a function $f(x)$ for many different values of x simultaneously. Imagine what the result of some arbitrary function $f(x)$ will produce when the input is a superposition $x = \frac{1}{\sqrt{2}}|0\rangle + \frac{1}{\sqrt{2}}|1\rangle$:

$$f(x) = \frac{1}{\sqrt{2}}f(|0\rangle) + \frac{1}{\sqrt{2}}f(|1\rangle). \qquad\qquad (1.2.7)$$

We can see that the resultant state contains information about both possible values $f(|0\rangle)$ and $f(|1\rangle)$. However, quantum parallelism is not useful immediately on its own, as measurement of the final state would give either $f(|0\rangle)$ or $f(|1\rangle)$. Quantum *algorithms* makes it possible to extract information about more than one state of $f(x)$. For example, it can be the result of addition *modulo 2* of $f(|0\rangle)$ and $(|1\rangle)$ [14]. Quantum computers can determine that result in a single evaluation of $f(x)$, which classical computers cannot do.

Just like in classical computation, the state of the quantum information register can be transformed with logic gates. Classical gates are usually implemented with diodes

or transistors in electric circuits. One of the simplest examples of classical gates is NOT. This gate flips the state of the bit:

$$NOT(0) \rightarrow 1, \tag{1.2.8a}$$

$$NOT(1) \rightarrow 0. \tag{1.2.8b}$$

Gate NOT is an example of a reversible gate. Classic logic gates can also be irreversible, while all quantum gates must be reversible, which follows from the unitary nature of the Schrodinger equation. All classic computation can be constructed from reversible gates only, thus quantum computers would be able to perform all the calculations classical computers do. Since gate NOT is reversible it is present in quantum logic as well:

$$NOT|0\rangle \rightarrow |1\rangle, \tag{1.2.9a}$$

$$NOT|1\rangle \rightarrow |0\rangle. \tag{1.2.9b}$$

The action of this quantum gate would be seen as a state-to-state transitions in a two-state quantum system.

Every quantum gate can be represented in matrix form. The gate NOT matrix form would look as following:

$$NOT \equiv \begin{pmatrix} 0 & 1 \\ 1 & 0 \end{pmatrix}. \tag{1.2.10}$$

To find the result of a logic gate action on a value of the qubit, we just need to look at the product of a gate matrix and qubit vector. This product gives new state vector

and shows the final state of the qubit. In this interpretation action of the gate NOT (Eq. 1.2.9) can be described as following:

$$\text{NOT}|0\rangle = \begin{pmatrix} 0 & 1 \\ 1 & 0 \end{pmatrix}\begin{pmatrix} 1 \\ 0 \end{pmatrix} = \begin{pmatrix} 0 \\ 1 \end{pmatrix} \rightarrow |1\rangle, \qquad (1.2.11a)$$

$$\text{NOT}|1\rangle = \begin{pmatrix} 0 & 1 \\ 1 & 0 \end{pmatrix}\begin{pmatrix} 0 \\ 1 \end{pmatrix} = \begin{pmatrix} 1 \\ 0 \end{pmatrix} \rightarrow |0\rangle. \qquad (1.2.11b)$$

There are quantum gates specific to quantum logic, that have no analogues in classical computation. The most important among them are Hadamard transform and phase rotation. The Hadamard transform creates superposition states out of eigenstates:

$$\text{Had}|0\rangle \rightarrow \frac{1}{\sqrt{2}}|0\rangle + \frac{1}{\sqrt{2}}|1\rangle, \qquad (1.2.12a)$$

$$\text{Had}|1\rangle \rightarrow \frac{1}{\sqrt{2}}|0\rangle - \frac{1}{\sqrt{2}}|1\rangle, \qquad (1.2.12b)$$

or in the matrix form:

$$\text{Had} = \frac{1}{\sqrt{2}}\begin{pmatrix} 1 & 1 \\ 1 & -1 \end{pmatrix}, \qquad (1.2.13)$$

and its action is:

$$\text{Had}|0\rangle = \frac{1}{\sqrt{2}}\begin{pmatrix} 1 & 1 \\ 1 & -1 \end{pmatrix}\begin{pmatrix} 1 \\ 0 \end{pmatrix} = \frac{1}{\sqrt{2}}\begin{pmatrix} 1 \\ 1 \end{pmatrix} \rightarrow \frac{1}{\sqrt{2}}|0\rangle + \frac{1}{\sqrt{2}}|1\rangle, \qquad (1.2.14a)$$

$$\text{Had}|1\rangle = \frac{1}{\sqrt{2}}\begin{pmatrix} 1 & 1 \\ 1 & -1 \end{pmatrix}\begin{pmatrix} 0 \\ 1 \end{pmatrix} = \frac{1}{\sqrt{2}}\begin{pmatrix} 1 \\ -1 \end{pmatrix} \rightarrow \frac{1}{\sqrt{2}}|0\rangle - \frac{1}{\sqrt{2}}|1\rangle. \qquad (1.2.14b)$$

Another quantum gate is the phase rotation. It introduces a phase shift into the superposition of eigenstates, but leaves probabilities of measuring $|0\rangle$ or $|1\rangle$ unchanged. The most common example of these gates is π-rotation:

$$R_\pi = \begin{pmatrix} 1 & 0 \\ 0 & e^{i\pi} \end{pmatrix}. \qquad (1.2.15)$$

It acts as follows:

$$R_\pi|0\rangle \rightarrow |0\rangle, \qquad (1.2.16a)$$

$$R_\pi|1\rangle \rightarrow -|1\rangle; \qquad (1.2.16b)$$

or in the matrix form:

$$R|0\rangle = \begin{pmatrix} 1 & 0 \\ 0 & e^{i\pi} \end{pmatrix}\begin{pmatrix} 1 \\ 0 \end{pmatrix} = \begin{pmatrix} 1 & 0 \\ 0 & -1 \end{pmatrix}\begin{pmatrix} 1 \\ 0 \end{pmatrix} = \begin{pmatrix} 1 \\ 0 \end{pmatrix} \rightarrow |0\rangle, \qquad (1.2.17a)$$

$$R|1\rangle = \begin{pmatrix} 1 & 0 \\ 0 & e^{i\pi} \end{pmatrix}\begin{pmatrix} 0 \\ 1 \end{pmatrix} = \begin{pmatrix} 1 & 0 \\ 0 & -1 \end{pmatrix}\begin{pmatrix} 0 \\ 1 \end{pmatrix} = \begin{pmatrix} 0 \\ -1 \end{pmatrix} \rightarrow -|1\rangle. \qquad (1.2.17b)$$

The gate NOT, the Hadamard transform and the phase rotation operate with states of a single qubit. *Multi-qubit* gates also play important role in quantum computation. The most important, for reasons discussed below, is the 2-qubit gate CNOT (conditional NOT). CNOT operates with two qubits, one of which is the *control* qubit and the other is the *target* qubit. The target qubit is left unchanged when the control qubit is in the state $|0\rangle$, but it is flipped when control qubit is in the state $|1\rangle$. Therefore four different transitions are possible:

$$CNOT|00\rangle \rightarrow |00\rangle$$
$$CNOT|01\rangle \rightarrow |00\rangle$$
$$CNOT|10\rangle \rightarrow |11\rangle \qquad (1.2.18)$$
$$CNOT|11\rangle \rightarrow |10\rangle$$

In order to encode two qubits, the quantum system must have $2^2=4$ different eigenstates. Hence, four vectors are needed to represent states of the two qubits, for example:

$$|00\rangle = \begin{pmatrix} 1 \\ 0 \\ 0 \\ 0 \end{pmatrix}, \quad |01\rangle = \begin{pmatrix} 0 \\ 1 \\ 0 \\ 0 \end{pmatrix}, \quad |10\rangle = \begin{pmatrix} 0 \\ 0 \\ 1 \\ 0 \end{pmatrix}, \quad |11\rangle = \begin{pmatrix} 0 \\ 0 \\ 0 \\ 1 \end{pmatrix}. \qquad (1.2.19)$$

In matrix form gate CNOT is represented by a 4x4 matrix:

$$\text{CNOT} \equiv \begin{pmatrix} 1 & 0 & 0 & 0 \\ 0 & 1 & 0 & 0 \\ 0 & 0 & 0 & 1 \\ 0 & 0 & 1 & 0 \end{pmatrix}. \qquad (1.2.20)$$

One can check that this matrix transforms the vectors from Eq. 1.2.19 according to Eq. 1.2.18.

The importance of the CNOT gate, as well as the Hadamard transform and the phase rotation gates, is that they from a *universal gate set*, e.g. any quantum algorithm can be built using only these three gates. To show how a particular algorithm is implemented with basis gates, circuit diagrams are used. Qubits are shown on circuit diagrams with horizontal lines. Each gate is labeled with a pictogram. A few pictograms are presented on Figure 1.3. is the preparation of equally weighted superpositions in
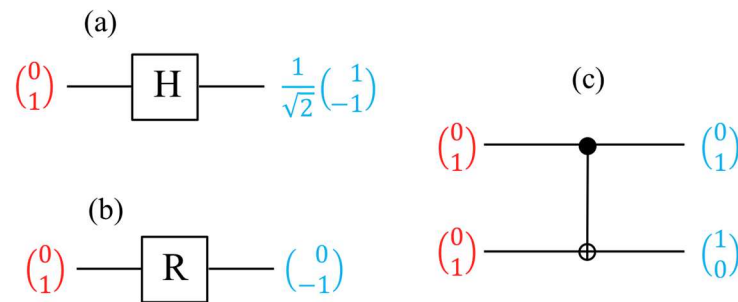
Figure 1.3: Pictograms of quantum gates: (a) Hadamard transform; (b) phase rotation; (c) CNOT. Horizontal lines represent states of qubits, red and blue are input and output qubit states accordingly. Examples of outputs are shown for input state $|1\rangle$. In panel (c) the black dot labels the control qubit and the white dot labels the target qubit of the CNOT gate.

qubits 1 and 2. The next step, blue, is the modular exponentiation with qubits 2, 3 and 4. The following section, green, performs the inverse quantum Fourie transform with qubits 1 and 2. The last block, pink, is the preparation of qubits 1 and 2 for measurement. Any arbitrary quantum algorithm can be presented in a similar manner.

1.3 Physical realization of quantum computer

Physical implementation of quantum computer is a non-trivial problem and it is the center of attention of numerous researches. DiVincenzo [16] formulated five requirements a scalable quantum computer (that can be expanded on large number of qubits) must comply with:

1) well-defined physical qubits;
2) reliable initial state preparation;
3) low decoherence rates;
4) accurate quantum gate operations;
5) reliable measurement.
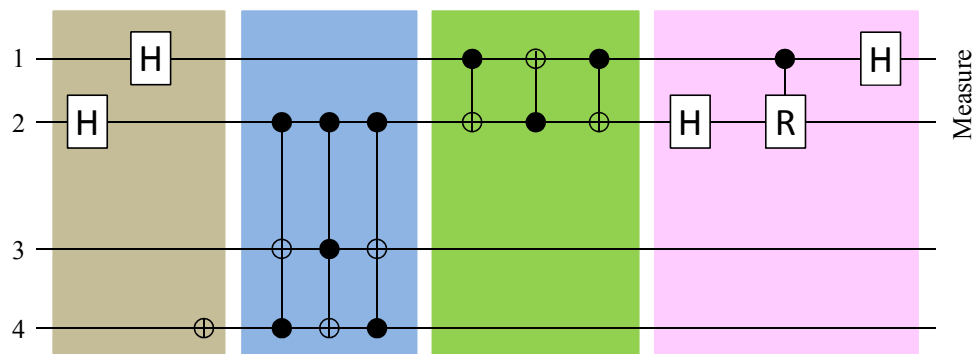
Figure 1.4: Quantum circuit diagram for the phase estimation part of Shor's algorithm for factorizing number 15 using four qubits (read from left to right) [15]. See text for details.

Different candidates for appropriate physical system to realize quantum computations are being studied. Quantum computer based on nuclear magnetic resonance was the first. The NMR quantum computing operates with nuclear spin states of atoms in a molecule as qubits. Logical gates are implemented with RF pulses that are applied perpendicular to a strong magnetic field. In 2001, a group at IBM successfully implemented Shor's algorithm for factorization number 15 with 7 qubits using perfluorobutadienyl iron complex [17]. It was found later that NMR quantum computer cannot consist of a large number of qubits, due to the decreasing signal to noise ratio with increasing size of the molecule.

One of the leading approaches for quantum computation now is the *ion-trap* quantum computer. It employs atomic ions confined in electric field as a quantum system for computations. Qubits are stored in the electronic levels of ions and qubit transformations are done with laser pulses. The first scheme of quantum computation with ion trap was proposed in 1995 by I. Cirac and P. Zoller. Since then a lot of progress has been made on exploring this approach. Nowadays, the ion-trap scheme can implement 14 qubits in a single trap [18], and researchers are looking for methods to combine quantum information from several independent traps.

A variety of other possible implementations of quantum computation is being studied. These include superconductor-based quantum computer [19], optical lattices [20], cavity quantum electrodynamics [21], quantum dots [16] etc.

1.4 Molecular quantum computer

Molecular quantum computation is relatively new but is a promising approach for the realization of quantum computer. It employs quantum states (electronic, vibrational, rotational) of individual molecules to encode qubits. Ultrafast laser pulses are used to control state-to-state transitions to perform quantum computation. This architecture offers an unprecedented speed of gate operations on the femto-second time-scale.

The idea of using molecules for quantum computation was first proposed by R. Vivie-Riedle in 2001 [22]. This work was done using a model of acetylene molecule C_2H_2. Vibrational states of acetylene were used to encode qubits. The molecule of acetylene has five vibrational modes. Two of them are IR-active and could be controlled. These two modes (*cis*-bending and assymetric CH-stretching) were used to encode qubits (Figure 1.5). One quantum of excitation is each mode corresponded to the state $|0\rangle$, two quanta correspond to the state $|1\rangle$. This results in total of four states of the two-qubit system: $|00\rangle$, $|01\rangle$, $|10\rangle$ and $|11\rangle$. Each of these states is a *combination state* of two chosen vibrational modes (Figure 1.6).
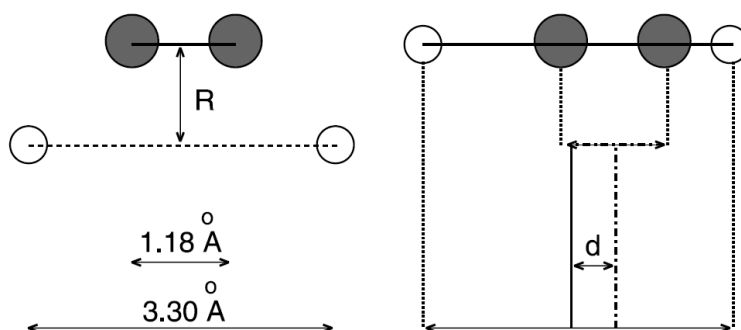
Figure 1.5: IR-active vibrational modes of acetylene. *Cis*-bending is described with coordinate R, assymetric CH-streching is described with coordinate d. [22]

Computation is performed through direct state-to-state transitions induced by a shaped femtosecond IR laser pulse. In order to find the optimal pulse shape, the optimal control theory (OCT) was used. OCT is based on maximizing objective functional, specific to an optimizational problem. OCT optimization is performed in a time domain where the value of electric field can be varied in every point on the time grid. Optimization was performed for two-qubit versions of gates NOT and Hadamard. Their first results for gate fidelity were ~70%. In their second paper [23] CNOT gate was optimized and the fidelity of the gates was improved to 99% by implementing the multi-target version of objective functional.

Figure 1.6: Qubit assignment for vibrational states of acetylene. v_b and v_s indicate number of quanta of excitation in bending and stretching modes, respectively. Qubit states are highlighted with green color.

This computational study of acetylene showed a general approach for molecular quantum computation. It generated large interest in molecular quantum computation. The group of Vivie-Riedle had extensively studied acetylene in the past and parameters, such as vibrational energy spectrum and transition dipole moments were well known, which influenced the choice of molecule. A number of diatomic and polyatomic molecules were studied theoretically during the past decade by several researchers: OH [24], I_2 [25], NH_3 [26], CO [27], HF [28], $MnBr(CO)_5$ [29], C_2H_2BrCl [30], and even such a large biomolecule as retinal [31]. In particular, such important aspects as the influence of anharmonicity of the molecule and the possibility of phase control of qubit transformations were studied by the group of D. Babikov [24,32].

Controlling transitions between vibrational states directly requires shaped IR laser pulses. Pulse shaping in IR range is a very challenging experimental problem and a reliable technique has yet to be developed. An alternative approach for implementation of qubit transformations in molecular quantum computer was proposed by M. Gruebele in 2007 [33]. Instead of direct state-to-state transitions, populations could be transferred from one vibrational state to another via an excited electronic state (the *gateway* state), which makes the use of UV/vis lasers for control possible. Technology of pulse shaping in UV/vis range is well established [33]. This approach brings the idea of molecular quantum computer much closer to the experimental realization.

Spectroscopy of thiophosgene, $SCCl_2$, has been studied in the group of M. Gruebele for a long time [34,35]. Vibrational energy spectra and transition dipole moments of thiophosgene have been experimentally determined [36]. The proposed scheme of quantum computation is shown on Figure 1.7. Assignment of qubit states was

done using a group of vibrationally excited states in the ground electronic state. The energy range of the vibrational states that were used was $8,000 - 8,500$ cm^{-1}. Transitions between states are not direct, but go via the electronically excited "gateway" state. A shaped laser pulse induces population cycling between the vibrational states and the gateway to perform computation. When the final superposition of computational states is achieved, another pulse projects this superposition to the electronically excited readout state. Analysis of the fluorescence from the readout state discloses the result of the computation.

In the experiment of M. Gruebele a laser pulse is shaped using genetic algorithm (GA). GA performs optimizations of a laser pulse in the frequency domain using techniques such as inheritance, mutation, selection, and crossover. GA can also be used for computational study of pulse shaping. Therefore GA calculations can give good estimation of what results can be obtained experimentally. The first results of optimization for CNOT gate were promising, but the gate fidelity was not high enough for reliable quantum computation.

The study of thiphosgene demonstrated the possible advantages of molecular quantum computation. Heavy molecules such as thiophosgene have a large number of vibrational states, which means that multi-qubit system can be encoded into a single molecule. Molecular vibrational states are stable against spontaneous emission and using them to assign qubit states allows performing reliable computation. Introducing the gateway state as a intermediate state for population transfer enables control of transitions with UV/vis laser.
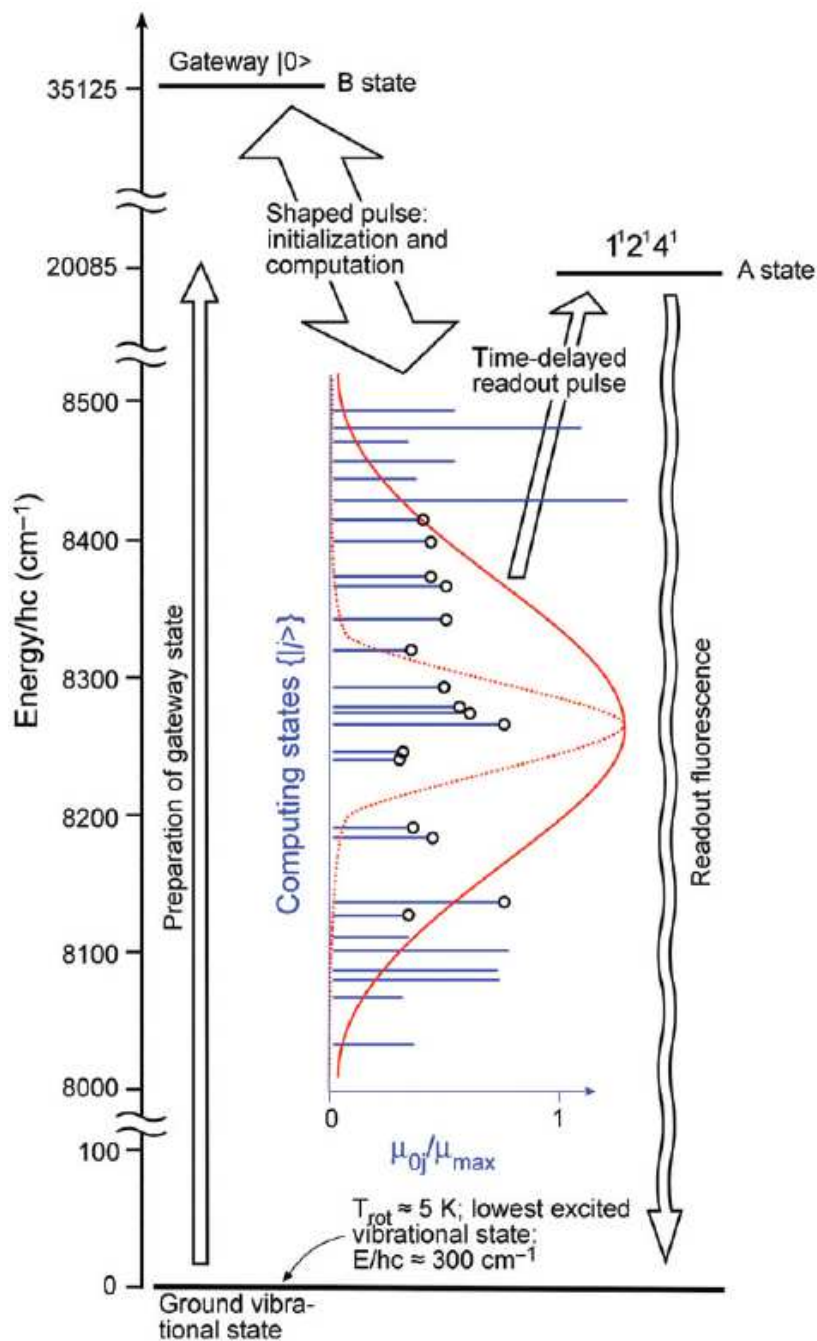
Figure 1.7: Quantum computation scheme with thiophosgene molecule. Blue lines indicate vibrational states in considered energy range; lengths of the blue lines correspond to the transition dipole moment to the gateway state. Arrows indicate the action of laser pulses through different stages of computational process. [33]

1.5 Ions trapped in a double-well potential

One of the main obstacles on the way of implementation of practical quantum computer is scalability. For molecular quantum computer to be scalable there needs to be a way to entangle multiple molecules while having individual access to them in order to control vibrational state-to-state transitions. Similar challenge is in the focus of the research in the field of ion trap quantum computing. A significant progress has been achieved in the experiments with ion traps demonstrating control of strings with up to 9 ions in a single trap [37-38] as well as interaction between ions in separated traps [39-40].

A possible way to tackle the problem of scalability in quantum computing is to combine the advantages of molecular quantum computer with the achievements in the field of ion traps. With trapped molecular ions we would have access to control a large number of internal vibrational states increasing the number of available qubits. At the same time control over trap parameters could enable interaction between multiple molecular ions and also allow to transfer molecular ions between separated traps.

In the context of possible application of ion traps for molecular quantum computer the recent experiments at NIST [39] and in Innsbruck [40] with two ions trapped in a double-well potential are of particular interest. In these experiments two ions were confined within potential wells separated by a large distance ($40 - 54$ µm) and high potential barrier ($\sim 10^5$ quanta of vibrational excitation) that prevents tunneling between the wells (see Figure 1.8). However the experiments showed that ions exchange vibrational energy because of the Coulomb coupling. The vibrational exchange was demonstrated on a level of a few quanta of vibrational excitation and it was shown that ions swap their vibrational

states completely. The period of this swap is determined by the splitting between the frequencies of the normal vibrational modes of the system.

The demonstration of the direct coupling between the ions is a crucial result in the pursuit of a scalable quantum computation with trapped ions. Application of this approach for molecular ions would further increase the number of available qubits by using the vibrational states of individual molecular ions for encoding qubit states.
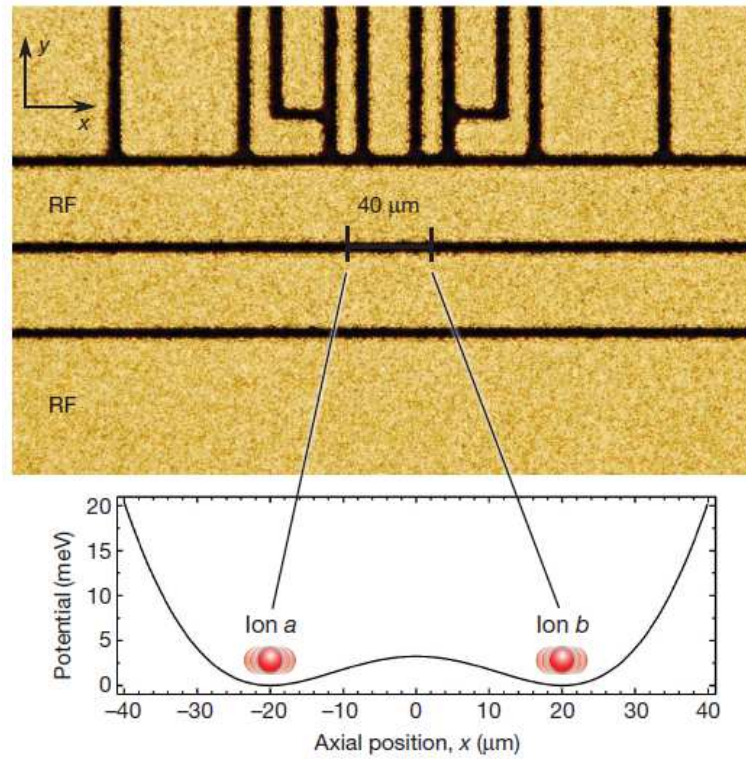
Figure 1.8: Experimental setup of two ions trapped in a double-well potential [38].

1.6 Summary of our project

Practical realization of molecular quantum computer is a very challenging problem. Experiments in this field are expensive and limited by a number of constraints. While experiments on molecular quantum computation are works in progress, theoretical studies can give very detailed and valuable insight. Using computational methods we can predict the optimal shapes of laser pulses, analyze the pulses in time and frequency domains, monitor evolution of state populations during the pulse action on the molecule, and check how molecular characteristics and laser pulse parameters affect gate fidelity. Modeling of molecular quantum computer using classic computers requires extensive computations, but successful theoretical studies bring us closer to the ultimate experimental realization of this idea.

In the work conducted so far, we examined what gate fidelity can be achieved in molecular quantum computation. This question is important in order to understand if reliable quantum computation can be achieved using molecules. The nature of quantum computer is probabilistic but quantum error correction methods enable fault-tolerant quantum computation. Quantum error correction can be used when fidelity of quantum gates is >0.9999 [41]. We focus on a computational scheme based on thiophosgene molecule as described above.

In Chapter 2, we compare the results of two pulse optimization strategies: OCT and GA optimizations for CNOT gate [42]. We can see that high-fidelity qubit transformations can be achieved at least in theory. Results obtained with both methods show similar features. Since OCT and GA employ completely different approaches to

optimization, we can conclude that the results obtained by calculations are method-independent.

In Chapter 3, we analyze in detail the final highly accurate pulse, optimized for a two-qubit gate CNOT [43]. We focus on representation of the optimized pulse in the frequency domain and look at what effect the possible experimental constraints would have on gate fidelity. We modify the optimized pulse by removing frequency components, changing amplitudes of the frequency components in a uniform or random manner, and by reducing the accuracy of the phase representation of the pulse. We find that the optimized pulse maintains high fidelity in a significant range of modifications.

In Chapter 4 we investigate the process of readout of quantum information from molecular vibrational states by the means of quantum beat spectroscopy. We analyze the accuracy of determination of populations and relative phase between two vibrational states from a numerical quantum beat signal using a fitting expression, obtained from perturbation theory. We find a phase error produced by the fitting expression and introduce a modification into the fitting formula that allows accurate phase determination.

In Chapter 5 we rigorously model quantum dynamics of a system of two ions in a double-well potential. We investigate the effective vibrational energy transfer between the ions separated by a high potential barrier and large distance. We study the time evolution of the vibrational wave packets on the accurate potential energy surface. We successfully confirm the results of two experiments [39, 40], provide new insights on the vibrational energy transfer and offer an interpretation of the efficient energy swap.

References for Chapter 1

1. P. Brumer and M. Shapiro, *Chem. Phys. Lett.*, **1986**, *126*, 541.

2. M. Shapiro and P. Brumer, *J. Chem. Phys.*, **1986**, *84*, 4103.

3. D. J. Tannor and S. A. Rice, *J. Chem. Phys.*, **1985**, *83*, 5013.

4. R. Kosloff, S. A. Rice, P. Gaspard, S. Tersigni and D. J. Tannor, *Chem. Phys.*, **1989**, *139*, 201.

5. M. Shapiro and P. Brumer, *J. Chem. Soc.*, *Faraday Trans*., **1997**, 93, 1263-1277.

6. K. Mishima and K. Yamashita, *J. Chem. Phys*. **1999**, *110*, 7756.

7. C. J. Bardeen, J. Che, K. R. Wilson, V. Yakovlev, P. Cong, B. Kohler, J. L. Krause, and M. Messina *J. Phys. Chem. A* **1997**, *101,* 3815-3822.

8. R. de Nalda, J. Durá, A. García-Vela, J. G. Izquierdo, J. González-Vázquez, and L. Bañares, *J. Chem. Phys*. **2008**, *128*, 244309.

9. R. Levis, G. Menkir, and H. Rabitz, *Science* **2001**, *27,* 709-713.

10. Web page of Prof. S. Varganov at University of Nevada, Reno website: http://www.chem.unr.edu/faculty/sav/.

11. J. L. Krause, M. Shapiro and P. Brumer, *J. Chem. Phys.*, **1990**, *92*, 1126.

12. M. Shapiro, E. Frishman and P. Brumer, *Phis. Rev. Lett.*, **2000**, *84*, 1669.

13. D. Lidar, *Chem. Eng. News*, **2003**, *81* ,36–37

14. M. A. Nielsen and I. L. Chuang, *Quantum Computation and Quantum Information* Cambridge University Press, Cambridge, **2000**.

15. L. Wang and D. Babikov, *J. Chem. Phys.*, **2012**, *137*, 064301.

16. D. Loss and D. P. DiVincenzo, *Phys. Rev. A*, **1998**, *57*, 120-126.

17. L.M.K. Vandersypen, M. Steffen, G. Breyta, C.S. Yannoni, M.H. Sherwood, I.L. Chuang, *Nature*, **2001**, *414*, 883–887.

18. T. Monz, P. Schindler, J. T. Barreiro, M. Chwalla, D. Nigg, W. A. Coish, M. Harlander, W. Hänsel, M. Hennrich and R. Blatt, *Phys. Rev. Lett.* **2011**, *106*, 130506.

19. J. Clarke and F. Wilhelm, *Nature*, **2008**, *453*, 1031–1042.

20. G. K. Brennen, C. Caves, P. S. Jessen, I. H. Deutsch, *Phys. Rev. Lett.,* **1999**, *82*, 1060–1063.

21. Q. A. Turchette, C. J. Hood, W. Lange, H. Mabuchi, and H. J.Kimble, *Phys. Rev. Lett*., **1995**, *75*, 4710.

22. C. M. Tesch, L. Kurtz, R. de Vivie-Riedle, *Chem. Phys. Lett.*, **2001**, *343*, 633-641.

23. U. Tropmann, R. de Vivie-Riedle, *J. Chem. Phys*. **2005**, *122*, 154105.

24. D. Babikov, *J. Chem. Phys*., **2004**, *121*, 7577.

25. Y. Ohtsuki, *Chem. Phys. Lett*., **2005**, *404*, 126-131.

26. M. Scroder, A. Brown, *J. Chem. Phys*., **2009**, *131*, 034101.

27. R. Zaari, A. Brown, *J. Chem. Phys*., **2010**, *132*, 014307.

28. S. Sharma, H. Singh, *J. Chem. Phys*., **2010**, *132*, 064108.

29. B. M. Korff, U. Troppmann, K. L. Kompa, and R. de Vivie-Riedle, *J. Chem. Phys*., **2005**, *123*, 244509.

30. L. Bomble *et al*., *J. Chem. Phys*., **2008**, *128*, 064110.

31. L. Bomble *et al*., *Phys. Rev. A*, **2007**, *76*, 043424.

32. M. Zhao and D. Babikov, *J. Chem. Phys*. **2006**, *125*, 024105.

33. D. Weidinger, M. Gruebele, *Mol. Phys*., **2007**, *105*, 1999.

34. P. D. Chowdary, B. Strickler, S. Lee and M. Gruebele, *Chem. Phys. Lett*. **2007**, *434*, 182-187.

35. S. Lee, M. Engel and M. Gruebele, *Chem. Phys. Lett*. **2006**, *420*, 151-156.

36. B. Strickler and M. Gruebele, *Phys. Chem. Chem. Phys*. **2004**, *6*, 3786.

37. R. Islam *et al*, Nature Commun. **2**, 377 (2011).

38. K. Kim *et al*, New J. Phys. **13**, 105003 (2011).

39. K. R. Brown *et al*, Nature **471**, 196 (2011).

40. M. Harlander, R. Lechner, M. Brownnutt, R. Blatt and W. Hansel, Nature **471**, 200 (2011).

41. E. Knill, *Nature* **2005**, *434*, 39.

42. E. Berrios, M. Gruebele, D. Shyshlov, L. Wang, and D. Babikov, J. Phys. Chem. A, **116**, 46 (2012).

43. D. Shyshlov, and D. Babikov, J. Chem. Phys. **137**, 194318 (2012).

Chapter 2: High fidelity quantum gates with vibrational qubits

2.1 Introduction

As discussed in detail by Deutsch,[1] the unitary propagation of quantum states can be usefully thought of as manipulation of information in certain contexts. In principle any switchable two-state system[2] can represent a qubit of information, which may be in a state $|0\rangle$, a state $|1\rangle$, or a linear superposition thereof.[3] Multiple qubits can be entangled, meaning a state $|ab\rangle$ cannot be separated into a product state $|a\rangle|b\rangle$. Superposition and entanglement distinguish quantum computing from classical computing with bits of either "0" or "1." Superposition allows quantum computing (QC) to represent many numerical scenarios at once – although questions about how well QC can solve general complex problems remain.[4]

Real systems implementing QC have sources of error: 'parasitic' quantum states coupled to the qubits can dephase them; a dissipative environment can relax the coherent population, destroying the entanglement of qubits. There is an abundance of mechanisms to decrease the fidelity F of the desired unitary transformations below 1. F generally can be defined as

$$F = \frac{1}{K} \sum_{k=0}^{K>2^n} |\langle \phi_k | \Psi_k(t) \rangle|^2, \qquad (2.1.1)$$

where $\{\phi_k\}$ is a set of K target states that the initial states $\{\Psi_k(0)\}$ must reach at time t when the quantum computation is complete. For example, the 'gate'

$$NOT = \begin{pmatrix} 0 & 1 \\ 1 & 0 \end{pmatrix} \qquad (2.1.2)$$

would transform $|0\rangle = \begin{pmatrix} 1 \\ 0 \end{pmatrix}$ to $\text{NOT}|0\rangle = |1\rangle = \begin{pmatrix} 0 \\ 1 \end{pmatrix}$. For initial states $|0\rangle$ and $|1\rangle$ it acts in

analogy to a classical NOT gate, but for superposition states new nonclassical results are

achieved. The fidelity of this gate from initial states, for example $\begin{pmatrix} 0 \\ 1 \end{pmatrix}$, towards targets, in

this example $\begin{pmatrix} 1 \\ 0 \end{pmatrix}$, is unity. But an actual implementation may have an error $\delta > 0$, for

example a phase error

$$\text{NOT} = \begin{pmatrix} \sin \delta & \cos \delta \\ \cos \delta & -\sin \delta \end{pmatrix} \qquad (2.1.3)$$

This would yield a fidelity $F < 1$ for the same initial states and desired targets, read out

at the same time t.

The gold standard for QC errors is > 0.9999 fidelity.[5] When the infidelity, defined

as $1 - F$, drops significantly below 10^{-4}, it becomes possible to implement error

correction algorithms that sacrifice some qubits to increase the accuracy of others.[6] Such

infidelities have not been reached experimentally in fully coherent QC systems, which

begs the question of how hard it would be with actual implementation.

We examine this question using a well-studied system for the effects of

dissipation and dephasing on QC fidelity: molecular vibrational qubits.[7] As first

suggested by de Vivie-Riedle,[8] entire vibrational modes of molecules can be used to

encode a qubit: the mode-to-qubit representation. Alternatively, as discussed by Kosloff

and us, qubits can be multiplexed over vibrational eigenstates, each corresponding to

excitation of several different modes.[9,10] Figure 2.1 shows how it is done. The one-

dimensional cut through the multidimensional potential surface of a polyatomic molecule

highlights four vibrational eigenstates. Four states can implement two qubits, such that

$|00\rangle = |\mathbf{n}\rangle$, $|01\rangle = |\mathbf{n'}\rangle$, $|10\rangle = |\mathbf{n''}\rangle$ and $|11\rangle = |\mathbf{n'''}\rangle$ maps the four linearly independent qubit configurations into vibrational states with quantum numbers $\mathbf{n}$ through $\mathbf{n'''}$. The four states are prepared in the desired initial state (for example $|00\rangle$ if both qubits are "off"). The a shaped laser pulse (the control field $\varepsilon(t)$) evolves the initial state to the desired target (for example $|11\rangle$ if the gate switches both qubits to "on"). The pulse $\varepsilon(t)$ does the computation using the molecular energy levels. Finally a probe laser then reads out the result (here: is all the population in state $|11\rangle$?).
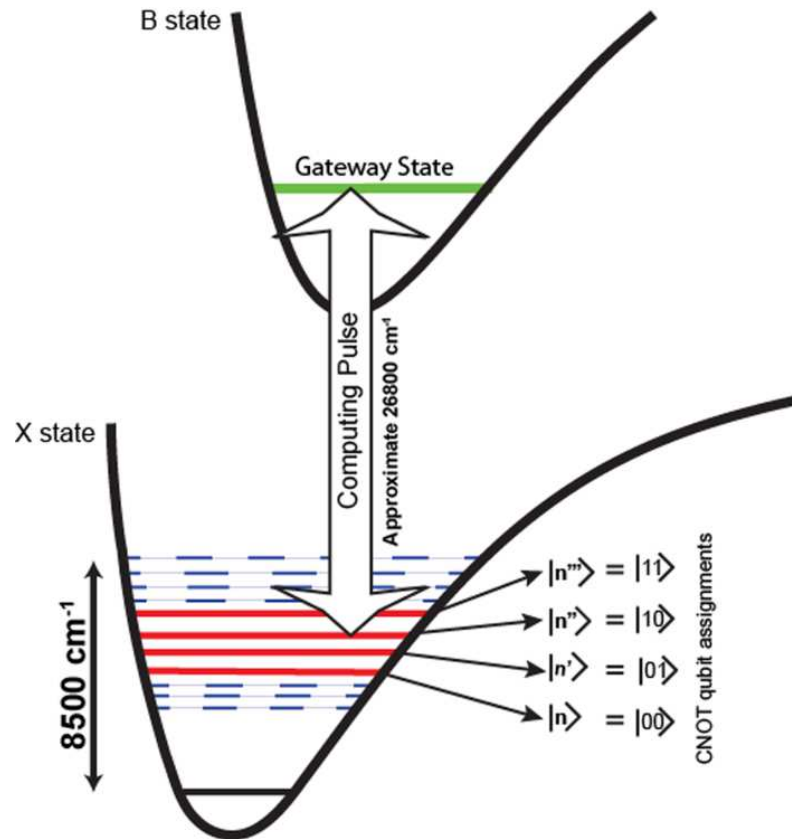
Figure 2.1: Quantum computing scheme. Population is initialized in the computing states (solid red lines). Then the computing pulse $\varepsilon(t)$ cycles population between these states and the gateway state (solid green line), while avoiding population of parasitic states (dashed blue lines).

We specifically consider the CNOT gate implemented on the ground electronic state surface of thiophosgene ($SCCl_2$), a molecule already extensively studied for low-fidelity QC.[9] The CNOT gate is one of the three fundamental gates from which any QC algorithm can be constructed.[3] In a CNOT gate, the state of qubit #1 decides whether qubit #2 is inverted or not. For example, if qubit #1 is "on" (in state $|1\rangle$), qubit #2 will switch from $|0\rangle$ to $|1\rangle$ or *vice-versa*. Such a gate requires 4 vibrational states to encode the two qubits.

We highlight two calculations, both with 24 parasitic vibrational states in addition to the four vibrational states that encode the two qubits. First we use optimal control theory (OCT)[11] to find the most optimal control field. Then we study a physical model that simulates a liquid crystal pulse shaper pumped by a regenerative amplifier and optimized by a genetic algorithm.[12] These calculations, utilizing very different methodologies, contrast what is possible in principle with what may be possible in practice. We do not consider rotational dephasing or field inhomogeneity here, as their effect has been discussed in detail elsewhere already (they can be circumvented because many near-optimal solutions $\varepsilon(t)$ exist).[9] We discuss what training input set works best to achieve good results across the board, given that the gate implementation is not perfect and that only a finite number of training states can be used. We conclude that fidelities needed for QC error correction are possible in principle, but will be challenging to achieve. At least in the context of molecular vibrations excited with current laser instrumentation driven by a genetic algorithm, convergence towards the optimal solution is a slow power law once the optimization gets beyond 99% fidelity.

2.2 Hamiltonian, qubits and gates

We simulate the action of a quantum gate on qubits encoded in molecular vibrations with two different methods: optimal control theory (OCT) and a physical pulse shaper model. These two simulations use a common set of vibrational states and transitions dipole moments to encode qubits, as well as similar field bandwidth. However, they calculate optimized solutions in different ways, as discussed further below, once we have summarized the common aspects.

In figure 2.1, the solid red lines represent four computing vibrational states and their qubit assignments for two qubits to be processed by a CNOT gate. Computation happens when the electric field of a shaped laser pulse ($\sim 26,800$ cm^{-1}) cycles an initial population between the four computing states (~ 8200 cm^{-1} above the zero point energy of the electronic ground state) and a single gateway state, here in the $\tilde{B}$ electronic state of thiophosgene. The result is read out at a specified time (the initialization and readout pulses are not simulated here – the limitations of the quantum computing process itself are the focus here). Ideally, the four computing states would be isolated from other non-computing states. However, this condition is hard to achieve in a real molecule. Therefore, we include parasitic states in our simulations (dashed blue lines in fig. 2.1), based on the real vibrational eigenstate distribution of SCCl$_2$.[13] Table 2.1 shows the contiguous set of vibrational state energies in the ground electronic state of SCCl$_2$ and their transition dipole moments to the gateway state, obtained from SCCl$_2$ experimental data, and identical to those used in a previous study of low-fidelity QC.[9] The four states of the two-qubit system

Table 2.1: SCCl$_2$ vibrational energy levels and transition dipole moments. Hadamard and CNOT qubit assignments.

Wavenumber (cm^{-1})	μ (Debye)	1-qubit assignments	2-qubit assignments
8032.86	0.47		
8067.17	0.41		
8080.09	0.96		
8087.79	0.94		
8101.18	1.00		
8111.49	0.44		
8126.73	0.42		
8136.98	0.96		
8182.75	0.55		
8191.03	0.44		
8239.53	0.36		
8246.35	0.38		$|00\rangle$
8264.26	0.96	$|0\rangle$	$|01\rangle$
8273.98	0.75	$|1\rangle$	$|10\rangle$
8278.82	0.70		$|11\rangle$
8292.89	0.61		
8319.93	0.43		
8342.37	0.62		
8366.49	0.62		
8372.81	0.54		
8398.00	0.53		
8414.60	0.29		
8427.80	1.00		
8444.25	0.29		
8457.20	0.42		
8471.08	0.26		
8481.07	0.84		
8492.72	0.42		

lie in a 32.47 cm^{-1} window, and the energy spacing between them are 4.84, 9.72 and 17.91 cm^{-1}. The 24 "parasitic" states span a 459.86 cm^{-1} wide range. The gateway state in the $\tilde{B}$ electronic state is separated by over ± 100 cm^{-1} from other vibrational states, so little population is lost in that part of the cycle.

The electric field $\varepsilon(t)$ performs a computation by manipulating the qubit amplitudes and phases coherently through time evolution under the quantum-classical Hamiltonian

$$\hat{H} = \hat{H}_0 - \hat{\mu} \cdot \hat{\varepsilon}(t). \tag{2.2.1}$$

H_0 is the vibrational Hamiltonian operator of SCCl$_2$, μ is the transition dipole moment operator between the gateway state and the set of computing states and $\hat{\varepsilon}(t)$ is the Hermitian field operator. Our field intensities are high enough to justify the classical approximation for the control field. The field bandwidth was chosen to match approximately the energy range of the four computing states in Table 2.1.

A quantum gate such as CNOT is represented by $\varepsilon(t)$ only if $\varepsilon(t)$ is trained so that all possible input states evolve according to the required unitary transformation. Consider the two-qubit gate CNOT, whose matrix representation in the basis set $\{|00\rangle, |01\rangle, |10\rangle, |11\rangle\}$ is:

$$\text{CNOT} = \begin{pmatrix} 1 & 0 & 0 & 0 \\ 0 & 1 & 0 & 0 \\ 0 & 0 & 0 & 1 \\ 0 & 0 & 1 & 0 \end{pmatrix}. \tag{2.2.2}$$

This quantum gate flips the second qubit when the first control qubit is "on" (lower right 2x2 block of the matrix), and leaves the second qubit unchanged if the first

control qubit is "off" (upper left 2x2 block of the matrix). The same electric field must take care of four different transitions:

$$\text{CNOT}|00\rangle \rightarrow |00\rangle$$
$$\text{CNOT}|01\rangle \rightarrow |01\rangle$$
$$\text{CNOT}|10\rangle \rightarrow |11\rangle \qquad (2.2.3)$$
$$\text{CNOT}|11\rangle \rightarrow |10\rangle$$

Since the four initial states in eq. (2.2.3) form a complete basis, it would seem to be sufficient to optimize only these four transitions given that the gate acts by linear unitary transformation. However, an $\varepsilon(t)$ optimized for the neighborhood of these initial qubits does not necessary provide the desired global phase relationship because of the phase difference imposed by the pulse.[14] Adding one more transition to the 2^n transitions for $n=2$ qubits constrains the phases:

$$\text{CNOT}\frac{1}{2}(|00\rangle + 01\rangle + 10\rangle + 11\rangle) \rightarrow \frac{1}{2}(|00\rangle + 01\rangle + 10\rangle + 11\rangle). \quad (2.2.4)$$

As we shall see later, adding this transition also improves performance for untrained inputs when the infidelity of the basic four state training set is not zero, which will always be the case in practice.

To what extent $\varepsilon(t)$ has been optimized to correspond to the desired gate is quantified by calculating the gate fidelity F according to equation (2.1.1). F is the average overlap between the target wavefuntions ϕ_k and the propagated wavefunctions $\Psi_k(t_{\text{Target}})$ at readout time t_{Target}. We now consider the differences between the OCT simulation and the physical model simulation.

2.3 Optimal Control Theory

Rabitz *et al.* developed an iterative algorithm to design the electric field $\varepsilon(t)$ that maximizes the transition probability from an initial state into a final target state while constraining the field intensity.[15] In OCT, calculating $\varepsilon(t)$ requires multiple iterations because the field has to induce multiple transitions (non-pertubative limit). The objective functional to be maximized in this case is:[16]

$$F_{OCT} = \sum_{k=1}^{K} |\langle \phi_k | \psi_k(t) \rangle|^2 - \int_0^{t_{\text{Target}}} \alpha |\varepsilon(t)|^2 dt$$

$$- \sum_{k=1}^{K} 2\text{Re} \left\{ \langle \phi_k | \psi_k(t_{\text{Target}}) \rangle \int_0^{t_{\text{Target}}} \left\langle \psi_k(t) \left| \frac{i}{\hbar} \hat{H} + \frac{\partial}{\partial t} \right| \psi_k(t) \right\rangle dt \right\}. \qquad (2.3.1)$$

Here the index k labels the transitions to be optimized, $K=5$ for our CNOT gate. The first term represents the overlap F between a laser-driven wave function $\psi_k(t)$ and a target final state ϕ_k at time $t = t_{\text{Target}}$. The second term in the functional minimizes the necessary electric field intensity. Finally, the last term ensures that wave functions evolve according to the Schrödinger equation.

The function α is a penalty function for the electric field smooth switching-on and switching-off. We use a simple, previously proposed function:[17]

$$\alpha = \frac{\alpha_0}{\sin^2(\pi t / t_{\text{Target}})}. \qquad (2.3.2)$$

This function ensures that the field goes to zero at $t=0$ and $t = t_{\text{Target}}$. The optimal pulse $\varepsilon(t)$ is obtained by maximizing equation (2.3.1) with respect to variations

in the wavefunctions and the electric field. This leads to a set of K time-dependent Schrödinger equations to be propagated forward and backward in time. The optimal field $\varepsilon(t)$ is then determined iteratively.[18-20]

In order to integrate the time-dependent Schrödinger equations, the time-dependent wavefunctions are expanded as a linear combinations of the vibrational eigenfunctions basis set with complex time-dependent coefficients $c_i(t)$. The set of coupled differential equations for the $c_i(t)$'s are solved by fourth-order Runge-Kutta with a 83 attosecond time step. The readout time t_{Target} is 25 ps. The norm error in the numerical wave packet propagation did not exceed 10^{-6}.

2.4 Physical Model

The above OCT iterative procedure to find $\varepsilon(t)$ is equivalent to experimentally shaping the electric field in the time domain with a time resolution given by the time step. With a fine step size and a suitable initial condition, the converged result is essentially the best pulse achievable in the targeted time window.

This freedom is not available in the laboratory because there is no electronic device with such high frequency response. Commonly, electro-optic or liquid crystal pulse shapers are employed in the laboratory. These devices attenuate and phase-shift the input pulse in the frequency domain in a finite number of frequency channels (256 to 1024 is typical). The input pulse is a fixed, nearly transform-limited ultrafast laser pulse (e.g. from a regenerative amplifier). The pulse is dispersed by a grating to spread it into its frequency components, each of which can then be attenuated or phase-shifted by a

pixel of the pulse shaper. The pulse is then recompressed into a shaped ultrafast pulse by another grating. Our physical model aims to take into account these experimental constraints, so we can see what can be achieved relative to ideal control.

We start with a transform-limited Gaussian pulse in the frequency domain,

$$\varepsilon_0(v) = E e^{\left(-(v-v_0)/(\sigma_v/2)\right)^2}.$$

(2.4.1)

We choose the bandwidth σ_v=15 cm^{-1} and peak field E=1·10^9 V m^{-1} to simulate a 2 μJ, ~1 ps pulse focused to a 25 μm diameter. Our carrier frequency v_0 is 13430 cm^{-1} in wavenumber units. The available bandwidth was chosen to be similar to the OCT optimum. Our input pulse characteristics are easily achieved with a high repetition rate regenerative amplifier pumped by a titanium:sapphire laser. We model the pulse shaper action by applying an amplitude and phase mask to $e_0(n)$ at a set of 1024 discrete frequencies v_i in steps of 1.25 cm^{-1}:

$$\varepsilon(v) = \varepsilon_0(v) A(v) e^{i\varphi(v)},$$

(2.4.2)

where $A(v)$ is the discrete amplitude mask that takes values between 0 and 1 and $\varphi(v)$ is the discrete phase mask that varies from $-\pi$ to π. The laser pulse $\varepsilon(v)$ is conveniently defined as a complex quantity to facilitate the rotating wave approximation,[21] which we will make to speed up quantum propagation. The shaped pulse $\varepsilon(v)$ is then Fourier transformed to get $\varepsilon(t)$. We oversample four-fold to obtain a smoothly decaying $\varepsilon(t)$, but the shaping has only 1024 discrete frequency channels, each with constant attenuation and a constant phase shift across the frequency step.

To optimize $\varepsilon(t)$, a genetic algorithm (GA), based on the FORTRAN subroutine pikaia,[22] evolves a family of $m=254$ different pulse shaper configurations. Each family member has different amplitudes and phases at 1024 frequencies to generate a different electric field $\varepsilon(t)$, whose performance is characterized by the fidelity defined in equation (2.1.1). The GA ranks the fitness of each family member according to its fidelity and proceeds to breed a new generation, closing the optimization cycle. To accelerate convergence, we employed in some cases a wavelet representation of the field so resolution could be gradually increased to the full 1024 pixels by factors of 2, and we used elitist selection[23] of the next generation of m computing pulses. A constant mutation rate equal to 0.001 was used because an adaptive mutation rate was prone to get trapped in local minima due to the small family of pulses (254) relative to the number of control channels (2×1024 for amplitude and phase).

Time evolution of the wavepacket under interaction with $\varepsilon(t)$ is calculated using the Shifted-Update Rotation (SUR) propagator.[24] SUR is a second order symplectic propagator acting in the energy representation by matrix-vector multiplication. The propagator is fast, compact to code, and allows implementation of a time-dependent electric field and of the rotating wave approximation[21] for larger time steps. The zero of energy for the rotating wave approximation was the average vibrational energy among the set of molecular states. The propagation time step was 40 attoseconds in order to ensure wavepacket propagation convergence to the fifth significant figure as measured by convergence of $\langle \phi_k | \Psi_k(t) \rangle$ real and imaginary parts. Fidelity is evaluated at $t_{\text{Target}} = 25$ ps, similar to the OCT simulations.

2.5 Results: Global OCT optimization

The CNOT gate is optimized for the five transitions defined in equations (2.2.3) and (2.2.4). As discussed in Methods, a 5th target state is added to the minimal complete set to lock the phases of different input qubit combinations.[14] The 4 computing states and 24 parasitic states nearby in energy were included in the computation. The pulse at ~ 26,800 cm^{-1} cycles population between computing states at ~8200 cm^{-1} and a gateway state at 35,000 cm^{-1} (Table 2.1). The fidelity of qubit transformation depended somewhat on the penalty factor α_0. Thus, several calculations were carried out with different α_0 values. Figure 2.2 is a Log-Log plot for results obtained with three different values of α_0, the parameter constraining electric field amplitude. The best fidelity obtained is $F = 0.999905$ with $\alpha_0 = 40.7$ (blue in fig. 2.2). Slightly stronger fields (lower penalties) lead to slightly lower fidelities. For example, with $\alpha_0 = 33.5$ we obtained $F = 0.99985$. If only four transitions of equation (2.1.3) are optimized, instead of five transitions, a slightly better fidelity of $F = 0.99993$ is obtained, at the cost of different phases between different training outputs. The OCT fidelities are close to the quantum accuracy threshold of $F > 0.9999$ by one standard estimate.[25]

Convergence in Figure 2.2 approximately obeys an inverse power law $1/g^{1.17}$, where g is the number of iterations. No leveling-off was observed at ~80,000 iteration, so performance with infidelity $1-F < 10^{-5}$ is likely with more iterations. The drawback, which will be even more evident in the physical model, is that power law convergence is rather slow. The origin of the power law behavior, as opposed to exponential convergence, is unknown (but see Discussion).

The optimized $\varepsilon(t)$ is shown in panel A in figure 2.3. It has field amplitudes fluctuating between ±40 MV m^{-1}. Panel B plots the vibrogram associated to $\varepsilon(t)$. The vibrogram was calculated by sliding a window of 16,384 time points in 500 point increments and calculating its discrete Fourier transform (windowed with a Hamming function[26]). The highest amplitude components are centered at 26850 cm^{-1}, so $\varepsilon(t)$ has no frequency chirp across the control pulse. Intensities around $5.3 \cdot 10^{11}$ J m^{-2} s^{-1} overlap the transition frequency region between the computing states and the gateway states around 26850 cm^{-1}.

Figure 2.2: Logarithmic plot of average infidelity as a function of OCT iteration number for optimization of CNOT. The results obtained with three slightly different penalty factors α_0 are presented. Convergence occurs as a power law (Iteration number)^m.
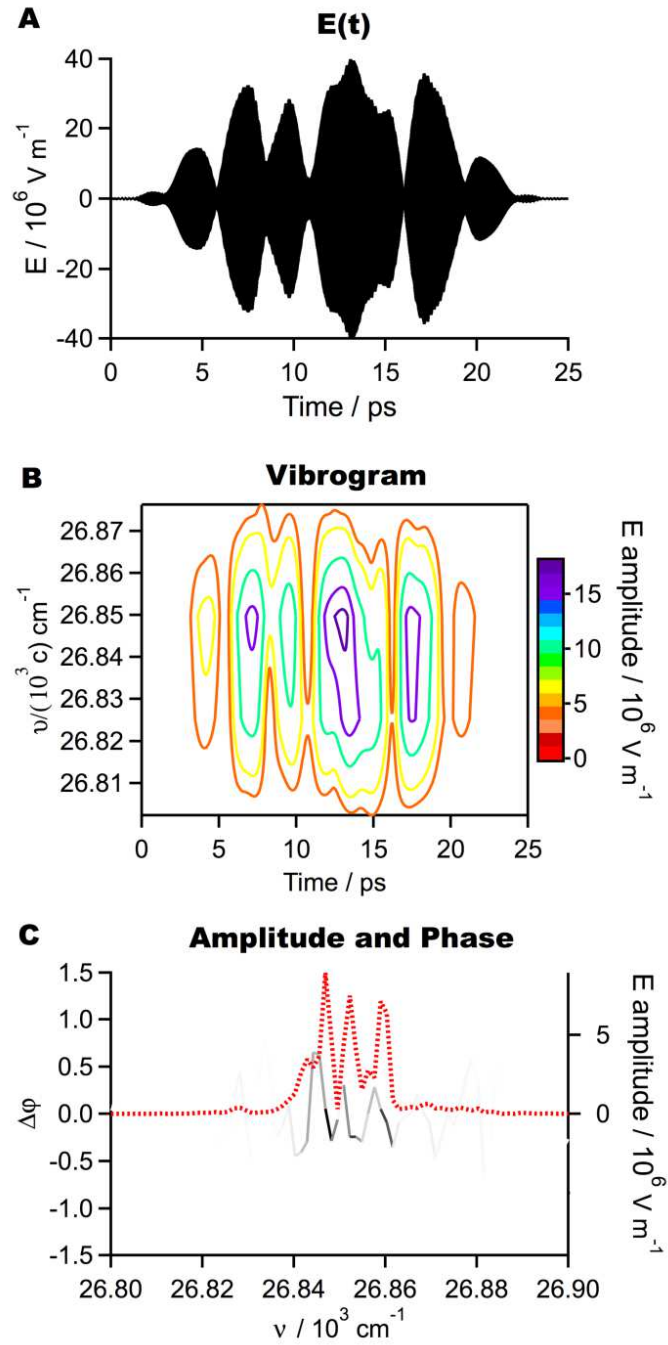
Figure 2.3: Electric field properties for the OCT optimized CNOT gate. The ε(t) in time domain is plotted in panel A; readout occurs at 25 ps when the pulse has died off and phases of states evolve freely. Panel B shows the windowed Fourier transform of ε(t). The amplitude and phase difference of the Fourier transform of $\varepsilon(t)$ are shown in panel C. The amplitude is used as grey color scale for the phase difference (black = largest magnitude, white = smallest magnitude).

The optimized $\varepsilon(t)$ is shown in panel A in figure 2.3. It has field amplitudes fluctuating between ± 40 MV m^{-1}. Panel B plots the vibrogram associated to $\varepsilon(t)$. The vibrogram was calculated by sliding a window of 16384 time points in 500 point increments and calculating its discrete Fourier transform (windowed with a Hamming function[26]). The highest amplitude components are centered at 26850 cm^{-1}, so $\varepsilon(t)$ has no frequency chirp across the control pulse. Intensities around $5.3 \cdot 10^{11}$ J m^{-2} s^{-1} overlap the transition frequency region between the computing states and the gateway states around 26850 cm^{-1}.

Panel C in figure 2.3 shows the amplitude and the phase derivative of the optimized electric field in the frequency-domain after Fourier transforming $\varepsilon(t)$. Three well-defined peaks correspond to the transitions frequencies for $\{|01\rangle, |10\rangle, |11\rangle\}$ at 26860.74, 26851.02 and 26846.18 cm^{-1}, respectively. The amplitude for the $|00\rangle$ transition frequency is small with respect to the rest, as might be expected for a CNOT gate. The phase derivative is gray scale-coded according to the corresponding electric field amplitude. The phase derivatives around the $|01\rangle, |10\rangle, |11\rangle$ peaks oscillate between ± 0.5 and present a negative phase shift across the peak field amplitudes.

Figure 2.4 demonstrates how state populations evolve under interaction with the CNOT optimized $\varepsilon(t)$. Panels A and B illustrate population dynamics for transitions, that leave target qubit state unchanged. Although nature of these transitions is similar, theirs population evolutions are drastically different from each other. Panel A (transition CNOT $|00\rangle \rightarrow |00\rangle$) indicates almost no change in states population during the pulse. Panel B shows that population of the initial state $|01\rangle$ decreases to ~0.2 on the mark
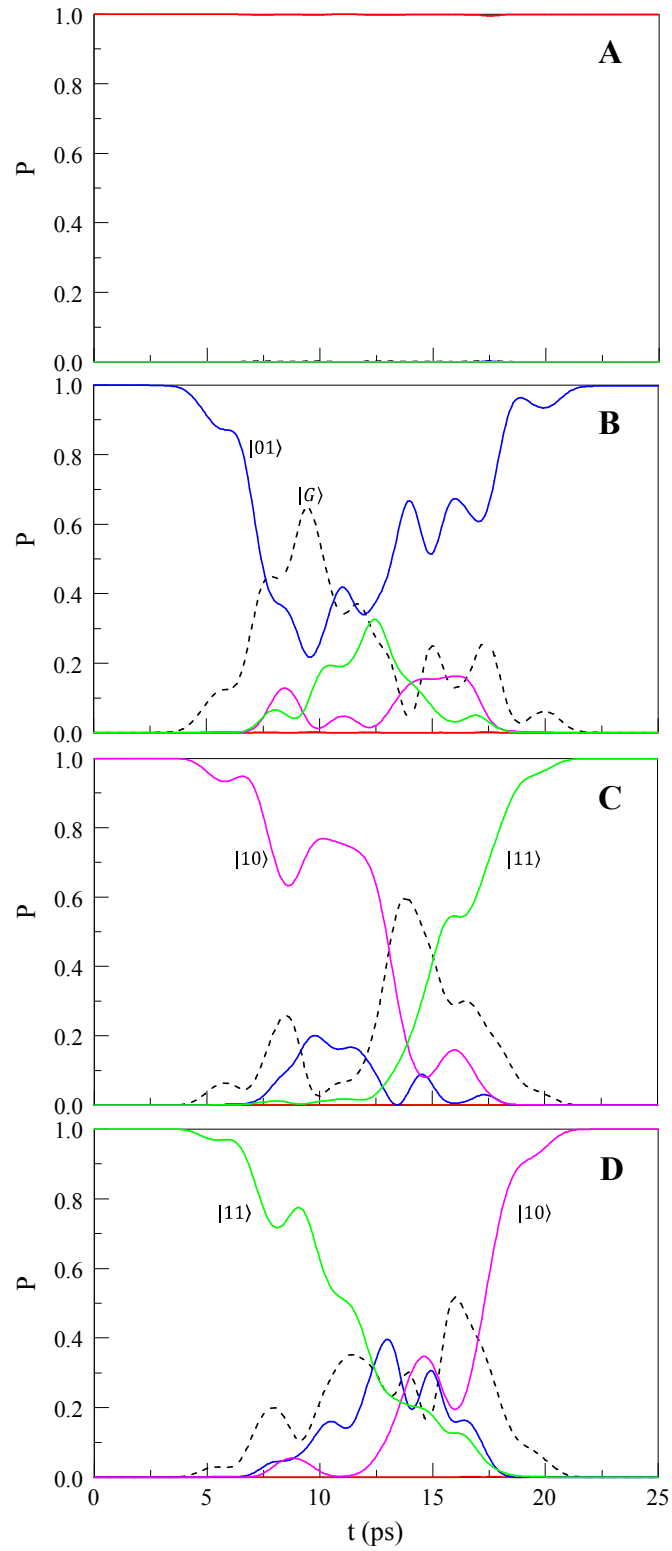
Figure 2.4: Population evolution for transitions of CNOT gate. Transitions shown: A) CNOT $|00\rangle \rightarrow |00\rangle$, B)CNOT $|01\rangle \rightarrow |01\rangle$, C) CNOT $|10\rangle \rightarrow |11\rangle$, D) CNOT $|11\rangle \rightarrow |10\rangle$.

about 10 ps, and then increases back at the end of the pulse. That can be explained with the fact that state $|01\rangle$ has larger energy gap from states $|10\rangle$ and $|11\rangle$ that must be flipped, and it also has the lowest dipole moment out of all four computational states.

Panels C and D illustrate population dynamics for transitions, that flip the state of the target qubit. They display similar features that can be discussed on example of transition CNOT $|11\rangle \rightarrow |10\rangle$ (panel D). At the beginning of the computation the quantum state corresponds to $|11\rangle$ as the whole wavepacket population is at the corresponding vibrational state. In order to transfer population to the vibrational state assigned to $|10\rangle$, the gateway state needs to be populated first. Due to the low electric field amplitude at the pulse start, this transfer is not appreciable until around 5 ps. At this time, the gateway state and $|01\rangle$ begin to be populated. It is not until 16 ps that $|10\rangle$ population increases rapidly to reach almost unity. It is worth noticing that the vibrational state assigned to $|00\rangle$ remains unpopulated through time evolution. Population in the parasitic states also remains very small throughout the computation.

2.6 Results: Physical model optimization

The physical model was used to compute what can be achieved with the same number (~80,000) iterations when 1024 preset, discrete frequency channels can be shaped. A constant Gaussian input pulse corresponding to a typical μJ output of a high repetition rate regenerative amplifier focused to ~500 μm^2 was implemented, and a genetic algorithm (GA) optimized the fidelity F in equation (2.1.1). The same 4 computing states and 24 non-computing parasitic vibrational states as in the OCT calculation were included in the physical model simulation (Table 2.1). The optimized

fidelity for a CNOT gate reached 0.99924 at 25 ps after ~80000 GA generations (Figure

2.5). Note that the readout in this case is done in the middle of the pulse, as opposed to

when the pulse has died of to zero intensity.

As in the case of the OCT calculations, an inverse power law describes the

convergence of $1 - F$. No leveling off of $1 - F$ is seen, but the slope in Figure 2.5 (-

0.56) is considerably smaller than for the OCT calculation. The even slower convergence

is due to the availability of fewer degrees of freedom in the electric field, and may be

further exacerbated because many frequency channels near the edge of the pulse shaper

use up GA time while not contributing significantly to the pulse.

The optimized electric field is shown in panel A of figure 2.6. The electric field is

represented by a complex valued function corresponding to the cos and sin phases. The

black (red) trace shows the envelope of the real part (imaginary part). Their amplitudes
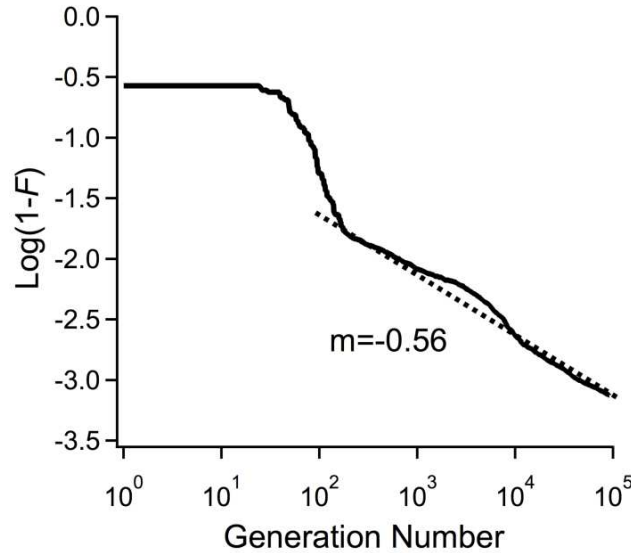
Figure 2.5: Average infidelity vs. number of generations for physical model optimization for CNOT gate. Both axes are in logarithmic scale. Convergence occurs with a power law ~ (Generation number)^m.

agree with the amplitude of the pulse optimized by OCT. The windowed Fourier transform of the complex $\varepsilon(t)$ yields the vibrogram plotted in panel B. It is calculated like the vibrogram in figure 2.3, but employing a 128 points window and 16 points separation between centers of two adjacent windows. The central frequency is located at 26860 cm^{-1}. Again no chirp was observed, just as in the OCT solution.

Panel C plots the amplitude and phase derivative of the Fourier transform of $\varepsilon(t)$. The width of the pulse is similar to the OCT solution (Fig. 2.3 panel C). However, there are more frequency components with significant amplitude, and the phase derivative shows larger fluctuations. The frequency components that connect the gateway state to state $|00\rangle$ are small. On the other hand, the frequency components for $|01\rangle$ frequency are relatively larger than in the OCT solution.

Figure 2.7 plots the population evolution of computing and non-computing states under interaction with the optimized $\varepsilon(t)$. The four computing state populations are shown in panel A. They corresponds to the transition CNOT$|11\rangle \rightarrow |10\rangle$. The population of state $|11\rangle$ starts out equal to unity at time zero (black trace) and it should be transferred completely towards state $|10\rangle$ (red trace). The vibrational state population, assigned to qubit $|00\rangle$ remains very small (<0.5%), as in the OCT optimization. The gateway state population reaches up to approximately 40% of the total population around the time $|10\rangle$ starts increasing its own population. The main population transfer stage takes place between 15 and 25 ps. The time evolution of the 8 most populated parasitic states is plotted
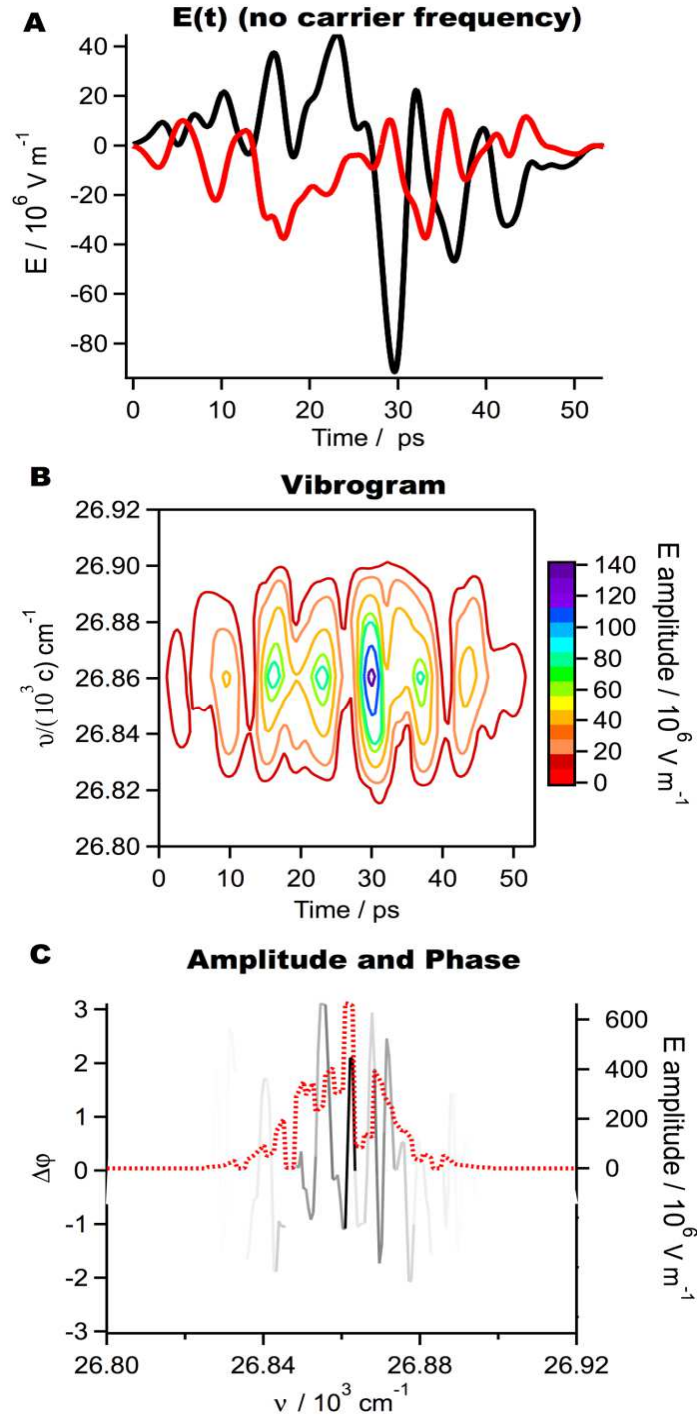
Figure 2.6: Physical model optimized pulse. Panel A shows the real (black) and imaginary (red) parts of the pulse envelope of $\varepsilon(t)$ without the carrier wave; readout occurs at 25 ps, when phases and populations still evolve under the input pulse. Panel B shows the windowed Fourier transform. Panel C plots the magnitude (red) and phase difference (gray). The magnitude is used as a color scale for the phase difference (black = largest magnitude, white = smallest magnitude).
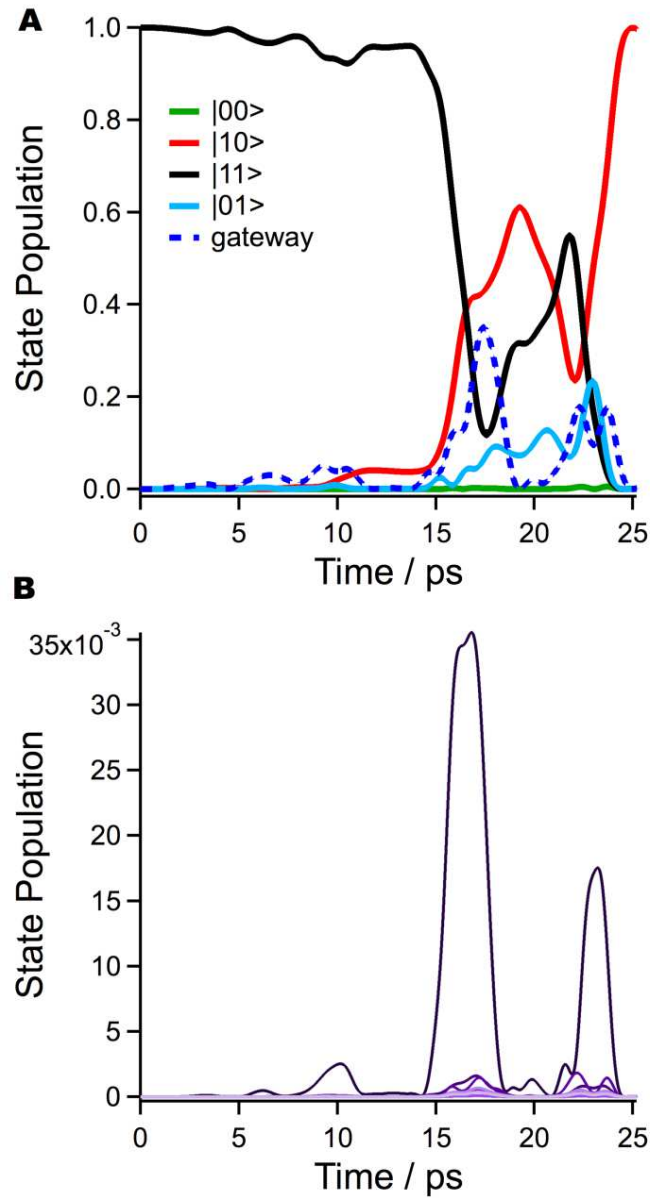
Figure 2.7: Population evolution for the transition CNOT|11⟩ → |10⟩ subject to the laser pulse $\varepsilon(t)$ optimized using the physical model. Panel A plots the computing states population as well as the gateway state. Panel B shows the population in eight non-computing states.

in panel B. Most of the states do not exceed 0.15% population, although the vibrational state adjacent to $|11\rangle$ in Table 2.1 is populated up to 0.35% at about 15 ps (dark purple trace). As expected form the fidelity >0.999, at readout time (25 ps), all eight states populations drop below 0.001%. Thus even the physical model with its fewer frequency channels is mostly able to avoid parasitic vibrational states whose excitation interferes with accurate quantum computing.

2.7 Discussion

Electric field optimization to perform quantum gate unitary transformations on vibrational qubits was accomplished successfully with Optimal Control Theory. Quantum gate fidelity as high as 0.999905 is obtained for five training states, even though a significant numbers of non-computing parasitic states are placed above and below the energy of the computing states. Very little population is transferred by the optimal control field to these parasitic vibrational energy levels. The fidelity achieved is close to the error threshold estimation to perform fault-tolerant quantum computations.[5]

On the other hand, the physical model with genetic algorithm does not achieve such high fidelity with a similar number of iterations. Only F=0.99924 was achieved. There are at least two possible reasons for this difference.

Although the physical model and OCT have similar pulse duration (and hence resolution in the frequency domain), the frequency channel positions are fixed in the physical model, and the genetic algorithm spends time randomly switching the phase and intensity of channels that are not resonant with computing states. The physical model can

be aided by zeroing out the amplitude of non-resonant frequency channels *a priori,* but at the cost of reduced pulse flexibility.

Both the OCT and physical model had to contend with 24 parasitic vibrational states in a ~500 cm^{-1} window around the 4 computing states. The OCT as well as physical model had to suppress population entering these states, in addition to optimizing the transfer of population among the four computing states. The OCT achieved this by keeping the field amplitude low and narrowly centered on the four computing states. The physical model did the same, but was not able to suppress population transfer into parasitic states as effectively. The ≈0.001% amplitude remaining at readout time in several parasitic energy levels largely accounts for the <0.999 fidelity obtained. The loss of computing population corresponds to unwanted relaxation, if we considered the parasitic states a 'bath' into which population from the computing states leaks.

Both types of calculations approach the optimal solution as an inverse power law of infidelity *vs.* the number of iterations or generations. The physical model does so particularly slowly, probably for the two reasons outlined above. This is of practical importance. Even if very small infidelities eventually can be reached by GA optimization of a pulse shaper, it could take prohibitively many iterations to reach a gate quality close to what is theoretically possible. The reason for the inverse power law convergence, as opposed to exponentially fast convergence, is not clear. Additional GA optimizations with different initial conditions also yielded inverse power law convergence with an exponent near 0.5, so this behavior is robust. We surmise the following: the optimization landscape is 'glassy,' that is, multiple optimal solutions exist that correspond to significantly different fields $\varepsilon(t)$. Once a very good solution has been found, it is very

hard to climb out of that local minimum to find a very slightly better solution that is far away on the optimization landscape.

Figure 2.8 plots a histogram of physical model CNOT gate fidelities, evaluated for 8000 randomly chosen input states not included in the training set. The augmented training set minimizes errors over the whole ensemble of possible input states. The fidelity of the augmented training set is 0.99793, 0.99982, 0.99965, 0.99944 for the training states in equation (2.2.3), and 0.99934 for the training state in equation (2.2.4). The average fidelity over all possible inputs was 0.9992, close to the average value for the training set (a red dashed line in Figure 2.8). Of course, if $F=1$ could be achieved for a complete minimal training set, all outputs would be perfect because of the linear superposition principle; this cannot be achieved in practice, one more reason why inclusion of state (2.2.4) is useful.
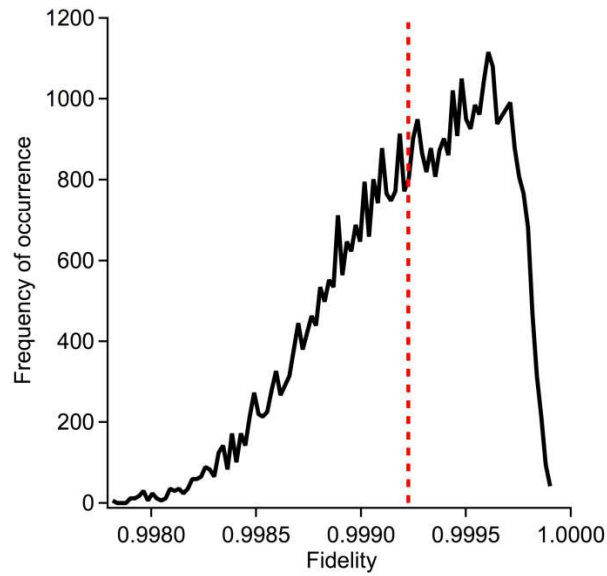
Figure 2.8: Histogram of fidelities for 8000 random input qubits interacting with the electric field $\varepsilon(t)$ optimized using the physical model. The red dashed line represents the average fidelity of the five training maps.

Gate complexity is a factor in the physical model simulations. To test this, we optimized a one qubit Hadamard gate. Along with CNOT, the Hadamard gate is one of the three fundamental gates suitable for constructing any QC algorithm.[3] The Hadamard gate returns a linear superposition with identical amplitudes of input states $|0\rangle$ and $|1\rangle$. Its unitary matrix representation is given by

$$\text{Had} = \frac{1}{\sqrt{2}}\begin{pmatrix} 1 & -1 \\ 1 & 1 \end{pmatrix}. \tag{2.7.1}$$

We used similar input pulse parameters and number of channels as in the CNOT physical model calculation. For this one-qubit gate, we obtained a fidelity of 0.999916 after only 18000 generations of the GA, significantly faster than for the CNOT gate. The 1024 control channels available to the physical model are better able to optimize population transfer for 2 states than for 4 states.

To conclude, it is possible for laser pulses of realistic duration, intensity and frequency bandwidth to implement simple gates for 1 and 2 vibrational qubits with >0.9999 fidelity, reaching the limit where error correction is possible. However, the 256 to 2048 frequency channels typically available for control present a problem: the number of channels is small enough to reduce control of population leaking into parasitic states, yet it is large enough to slow down GA optimization (at least when the family of pulses being optimized is smaller than the number of control channels). $F>0.99$ control is reached quite easily even within a short target time (~100 generations), but higher fidelities will require special measures to overcome the slow power law convergence of pulse-shaper/GA combinations: the bandwidth of the input field must be carefully tailored to the computing pulse to minimize excitation of parasitic molecular states;

excessive input intensity should be avoided even if in principle the pulse shaper can reduce the intensity to the desired level, to make best use of the pulse shaper amplitude resolution. Selecting only frequency channels near computing states for GA optimization (too many slows down GA convergence, too few makes control too coarse-grained) could also help.[27]

References for Chapter 2

1. Deutsch, D. *Proc. Roy. Soc. London Series A* **1985**, *400*, 97.

2. Doslic, N.; Kuhn, O.; Manz, J. *Ber. Bunsengesellschaft* **1998**, *102*, 292.

3. Nielsen, M. A.; Chuang, I. L. *Quantum Computation and Quantum Information*, 1 ed.; Cambridge University Press: Cambridge, 2000.

4. Bernstein, E.; Vazirani, U. *Siam Journal on Computing* **1997**, *26*, 1411.

5. Knill, E. *Nature* **2005**, *434*, 39.

6. Shor, P. W. *Physical Review A* **1995**, *52*, R2493.

7. Troppmann, U.; Gollub, C.; de Vivie-Riedle, R. *New Journal of Physics* **2006**, *8*.

8. Troppmann, U.; de Vivie-Riedle, R. *J. Chem. Phys.* **2005**, *122*.

9. Weidinger, D.; Gruebele, M. *Mol. Phys.* **2007**, *105*, 1999.

10. Amitay, Z.; Kosloff, R.; Leone, S. R. *Chem. Phys. Lett.* **2002**, *359*, 8.

11. Zhu, W.; Botina, J.; Rabitz, H. *J. Chem. Phys.* **1998**, *108*, 1953.

12. Charbonneau, P. *Ap. J. Supplement Series* **1995**, *101*, 309.

13. Strickler, B.; Gruebele, M. *PCCP* **2004**, *6*, 3786.

14. Zhao, M. Y.; Babikov, D. *J. Chem. Phys.* **2006**, *125*.

15. Zhu, W.; Botina, J.; Rabitz, H. *J. Chem. Phys.* **1998**, *108*, 1953.

16. Tesch, C. M.; de Vivie-Riedle, R. *Phys. Rev. Lett.* **2002**, *89*, 157901.

17. Sundermann, K.; de Vivie-Riedle, R. *J. Chem. Phys.* **1999**, *110*, 1896.

18. Babikov, D. *J. Chem. Phys.* **2004**, *121*, 7577.

19. Zhao, M. Y.; Babikov, D. *J. Chem. Phys.* **2007**, *126*.

20. Gu, Y.; Babikov, D. *J. Chem. Phys.* **2009**, *131*, 034306.

21. Allen, L.; Eberly, J. H. *Optical Resonance and Two-Level Atoms*, 2 ed.; Dover: New York, 1987.

22. Metcalfe, T. S.; Charbonneau, P. *J. Comput. Phys.* **2003**, *185*, 176.

23. Zitzler, E.; Deb, K.; Thiele, L. *Evolutionary Computation* **2000**, *8*, 173.

24. Bigwood, R.; Gruebele, M. *Chem. Phys. Lett.* **1995**, *235*, 604.

25. Aliferis, P.; Gottesman, D.; Preskill, J. *Quant. Inf. Comput* **2006**, *6*, 97.

26. Press, W. H.; Teukolsky, S. A.; al., e. *Numerical Recipes in Fortran*; Cambridge University Press: New York, 1992.

27.   Gruebele, M.; Wolynes, P. G. *Phys. Rev. Lett.* **2007**, *99*, 060201.

Chapter 3: Complexity and simplicity of OCT pulses shaped for controlling

vibrational qubits

3.1 Introduction

It is often argued that shaped laser pulses, prepared theoretically using the Optimal Control Theory (OCT), would be hard or even impossible to reproduce in experiments. In such calculations, the OCT pulse "shaping" is carried out in the time domain with the number of "tuning knobs" equal to the number of time-steps within the total pulse duration [1-3]. For example, for a 25 picosecond laser pulse the number of time steps (used for accurate propagation of time-dependent Schrodinger equation and optimization of pulse shape) may be close to 2^{20} [4]. Indeed, such flexibility is usually unavailable in experiments [5-7], where the number of frequency channels never exceeds 2^{10}. For this reason it is sometimes suggested that theoreticians migrate from the OCT methods towards the evolutionary genetic algorithms [8-10] that, similar to experiments, carry out pulse optimization in the frequency domain.

In this chapter, using standard techniques of Fourier transform, we show that the OCT pulses, seemingly complicated in time domain, are in fact very simple in the frequency domain. We demonstrate by calculations that a very accurate pulse, optimized in time domain for coherent manipulation of vibrational states of the molecule, can be reproduced surprisingly well using as few as 2^5 frequency channels. This is well within the reach of today's pulse shaping techniques, which justifies the use of OCT method as a predictive practical tool.

Another focus of this chapter is on robustness of the OCT solutions. It is sometimes argued that such pulses are very fragile, so that changing the pulse shape just slightly would change dramatically the result of action of the pulse on a molecule. In our numerical experiments we take a very accurate OCT pulse and modify it in several different ways, using filters in the frequency domain. The effect of modification is then studied by acting, with the modified pulse, on a molecule.

The issues of accuracy, reproducibility and robustness are particularly important in context of molecular quantum computing [11-32], where the requirements to fidelity of state-to-state transformations are very high. Thus, the examples studied here are drawn from the field of quantum information processing with vibrational qubits, where the optimized laser pulses are used to manipulate vibrational wave packets coherently, providing the desired unitary transformations of qubit states. For these cases, the effects of systematic and random errors of pulse shaping are studied.

This chapter is organized as follows. In Section 3.2 we describe in detail the physical model of vibrational quantum computer. Section 3.3 gives details of OCT pulse preparation. Results are presented and discussed in Section 3.4. Section 3.5 summarized major findings of this work.

3.2 The model system and quantum gates

We use vibrational eigenstates of thiophosgene ($SCCl_2$) to encode qubits. Vibrational spectrum and dipole moment matrix of this molecule are known from the experiment [33]. We focus on 28 vibrational eigenstates in energy range from 8,032 to 8,493 cm^{-1}. Four states close to the center of this interval, in the range from 8,246 to

8,279 cm^{-1}, are used to encode two qubits (computing states) but the remaining 24 states are also included in optimization in order to ensure that no population is transferred to other vibrational states (interfering states). Also, including all 28 vibrational states, in a ~ 450 cm^{-1} energy range, provide a realistic description of this physical system.

In the model of quantum computer considered here there is no direct population transfer between the computational states. Instead, all transitions go through the electronically exited state at energy 35,125 cm^{-1}, the gateway state referenced further as $|G\rangle$. This choice allows using laser pulses in the UV/vis range and makes experimental realization of this scenario possible, based on mature pulse shaping technology [34-37]. Table 3.1 gives energies and dipole moments for the most important states in our calculations. This includes four states of the two-qubit system and two interfering states, energetically closest to the computing states. Assignments of the qubit states are also given in Table 3.1. Energies and dipole moments of the remaining states can be found in Ref. [8].

Large number of vibrational eigenstates in thiphosgene makes it feasible to implement multi-qubit quantum gates or even simple quantum algorithms [8]. Here we focus on two-qubit gate CNOT (conditional NOT) which plays a very important role in quantum computation [38].

The action of this gate can be described as follows: If the first qubit (the control qubit) is in state $|0\rangle$ then the second qubit (the target qubit) is left unchanged but, if the first qubit is in state $|1\rangle$, than the state of second qubit is flipped. In a concise form this can be written as:

Table 3.1: Relevant vibrational energy levels and transition dipole moments of $SCCl_2$ molecule.

Energy (cm^{-1})	Dipole moment (Debye)	Two-qubit assignment
8191.03	0.44	--
8239.53	0.36	--
8246.35	0.38	$|00>$
8264.26	0.96	$|01>$
8273.98	0.75	$|10>$
8278.82	0.70	$|11>$
8292.89	0.61	--
8319.93	0.43	--

$$\text{CNOT } |00\rangle \rightarrow |00\rangle, \tag{3.2.1a}$$
$$\text{CNOT } |01\rangle \rightarrow |01\rangle, \tag{3.2.1b}$$
$$\text{CNOT } |10\rangle \rightarrow |11\rangle, \tag{3.2.1c}$$
$$\text{CNOT } |11\rangle \rightarrow |10\rangle. \tag{3.2.1d}$$

As explained in the next section, the laser field is optimized such that a single universal pulse is capable of carrying out each of these four transitions. Which one is actually performed, depends only on the initial state of the molecule. It should also be remembered that quantum system can be in any superposition of these states, and the laser pulse should be able to transform appropriately the superposition state as well. This is achieved by optimizing, in addition to four transitions above, the action of quantum gate onto an equally weighted superposition of qubit states:

$$\text{CNOT } \frac{1}{2}(|00\rangle + |01\rangle + |10\rangle + |11\rangle) \rightarrow \frac{1}{2}(|00\rangle + |01\rangle + |10\rangle + |11\rangle). \tag{3.2.2}$$

It has been demonstrated that, if all five transitions are optimized simultaneously, the common phase is enforced for all transitions and the resultant laser pulse is indeed capable of carrying out a unitary and coherent transformation of any arbitrarily chosen qubit state [16,39].

In practice, when optimization is never perfect, the accuracy of optimized pulse can be characterized by computing the average transition probability:

$$P = \frac{1}{K} \sum_{k=1}^{K} |\langle \varphi_f | \psi(T) \rangle|^2 . \qquad (3.2.4)$$

Each term of this sum represents an overlap of the actual the laser driven wave function $\psi(T)$ at the final moment of time T with the desirable perfect final state φ_f. Summation is over the set of transitions optimized simultaneously. For optimization of phase-corrected the CNOT gate K = 5, as discussed above. Another quality used to assess the optimized pulse is gate fidelity:

$$F = \frac{1}{K^2} \left| \sum_{k=1}^{K} \langle \varphi_f | \psi(T) \rangle \right|^2 . \qquad (3.2.4)$$

Note that in this expression different overlaps are added coherently, which takes into account the phase information. If the final phases of different optimized transitions are not perfectly aligned, the value of F can be low, even if the value of phase-insensitive P is high. Thus, monitoring F guaranties, and is usually done in conjunction with adding the fifth transition, Eq. (3.2.2), to the set of optimized transitions.

Our prior experience with this system and with other models of the vibrational quantum computer [40-43] tells that the multi-qubit conditional gate CNOT is usually the

hardest to optimize. If this gate is optimized and the result is satisfactory, then the other one-qubit quantum gates (such as unconditional NOT gate, the phase rotation gate and the Hadamard gate [38]) are relatively easy to optimize. So, in this paper we focus on the CNOT gate only. It is worth mentioning, that experimental demonstration of this one quantum gate would make a very important impact on the field of molecular QC, as it did in case of the ion-trap quantum computer [44,45].

3.3 OCT pulse optimization

We implement the multi-target version of the OCT as follows. We maximize the following functional

$$\Im \equiv \sum_{k=1}^{K} |\langle \phi_f | \psi(T) \rangle|^2 - \alpha \int_0^T \frac{\varepsilon^2(t)}{s(t)} dt$$

$$- \sum_{k=1}^{K} 2Re \left\{ \langle \phi_f | \psi(T) \rangle \int_0^T \left\langle \psi(t) \left| \frac{i}{\hbar} [\hat{H}_0 - \varepsilon(t)\mu] + \frac{\partial}{\partial t} \right| \psi(t) \right\rangle dt \right\}, \qquad (3.3.1)$$

with respect to variations in wave function $\psi(t)$ and the field $\varepsilon(t)$. The first term here is P from Eq. (3.2.3) and it is maximized. The second term represents energy of the laser field. It is minimized. Parameter α is a constant penalty factor and $s(t) = \sin^2\left(\pi \frac{t}{T}\right)$ is a variable penalty function. The last term of the functional (3.3.1) is constructed in such a way that system's dynamics is restricted to obey the time-dependent Schrödinger equation, while the system is driven from the initial state ϕ_i towards the final state ϕ_f. Note that this functional is a multi-target version [14,21], where the sum over k in the first and the last terms is taken over all optimized transitions, $1 \leq k \leq K$. Variations of

this functional with respect to the wave function and the field, one obtains the following

equations [1,46]: A set of K time-dependent Schrodinger equations propagated forward in

time:

$$i\hbar \frac{\partial}{\partial t} \vec{\psi}(t) = [\hat{H}_0 - \mu\varepsilon(t)]\vec{\psi}(t),$$
(3.3.2)

each with its own boundary condition $\vec{\psi}(0) = \phi_i$. A set of K analogous equation

propagated backward in time:

$$i\hbar \frac{\partial}{\partial t} \overleftarrow{\psi}(t) = [\hat{H}_0 - \mu\varepsilon(t)]\overleftarrow{\psi}(t),$$
(3.3.3)

each with its own boundary condition $\overleftarrow{\psi}(T) = \phi_f$. And one equation for the common

field:

$$\varepsilon(t) = -\frac{s(t)}{\alpha} \sum_{k=1}^{K} Im\langle\vec{\psi}(t)|\overleftarrow{\psi}(t)\rangle\langle\overleftarrow{\psi}(t)|\mu|\vec{\psi}(t)\rangle,$$
(3.3.4)

which uses information obtained from all these $2K$ equations.

In order to propagate the Schrödinger equation in time we use the basis set

expansion with time-dependent coefficients $c_n(t)$:

$$\psi(x,t) = \sum_{n=1}^{N} c_n(t) \cdot \varphi_n(x) \cdot e^{-iE_n t}.$$
(3.3.5)

Here $\varphi_n(x)$ are eigenfunctions of the system and E_n are their corresponding energy

eigenvalues. Substitution of this expansion into the time-dependent Schrödinger equation

leads to the following equations for the coefficients $c_n(t)$:

$$\dot{c}_n^R(t) = \varepsilon(t) \sum_m \left(c_m^R(t) \sin\theta_{m,n} - c_m^I(t) \cos\theta_{m,n} \right) \cdot M_{m,n},$$
(3.3.6a)

$$\dot{c}_n^I(t) = \varepsilon(t) \sum_m \left(c_m^R(t) \cos \theta_{m,n} - c_m^I(t) \sin \theta_{m,n} \right) \cdot M_{m,n}, \qquad (3.3.6b)$$

where $\theta_{m,n} = (E_m - E_n)t$ are phase shifts, $M_{m,n} = \langle \psi_m | \mu | \psi_n \rangle$ are the elements of the dipole moment matrix and c_m^R and c_m^I are real and imaginary parts of complex coefficient c_m. Equations (3.3.2-3.3.4) are then solved iteratively. The number of basis states in the expansion of Eq. (3.3.1) was $N = 29$. Those were 28 vibrational states in the ground electronic state of thiophosgene plus the gateway state. They all were included in the wave function propagation. The Runge-Kutta method of 4th order was used to propagate Eqs. (3.3.6). We start with backward propagation using the guess field in the following simple analytic form: $\varepsilon(t) = A \cdot \sin \omega t \cdot \sin^2 \left(\pi \frac{t}{T} \right)$, where A is amplitude of the guess field. Frequency of the guess field is $\omega = E_G - \bar{E}$, where E_G is energy of the gateway state and $\bar{E}$ is energy in the middle of the spectrum ($\bar{E} = 8269.12$ cm^{-1}). During the backward propagation, the program calculates new values of the field for each time step and this updated field is then used for the forward propagation, and so on. The pulse duration was set to $T = 25$ ps. This time interval was divided into 300,000 time steps for the Runge-Kutta propagation. This number was chosen as a compromise between the computational time and norm conservation. Thus, the time-step in our calculations is $\Delta t \approx 0.083$ fs. It was found that fidelity of propagation depends somewhat on the penalty factor α. Thus, several calculations were carried out with slightly different α values. Some of them were discarded. The "keeper" values follow: $\alpha = \{33.5, \ 34.7, \ 36.0, \ 37.1, \ 38.3, \ 40.1\}$.

Table 3.2: Average probabilities and fidelities for gate CNOT obtained with different values of the penalty factor.

α	P	F
33.5	0.999833	0.999690
34.7	0.999847	0.999746
36.0	0.999897	0.999780
37.1	0.999881	0.999728
38.3	0.999863	0.999794
40.1	0.999905	0.999837

3.4 Results and analysis

The probabilities and fidelities obtained for different values of penalty factor after 80,000 iterations are shown in Table 3.2. We found that for all values of the penalty factor used the probability of qubit transformation is slightly higher than fidelity. This behavior is expected, since calculation of fidelity takes phases of optimized transitions into account, and some small remaining phase errors lead to slight reduction of fidelity [38,39]. All probabilities are within 7.2×10^{-5} of each other and the same is true for fidelities. The best results were obtained with $\alpha = 40.1$, namely: $P = 0.999905$ and $F = 0.999837$. We see that the value of average probability slightly exceeds 0.9999, while the value of fidelity almost reaches 0.9999. We also saw that after ~ 80,000 iterations (when optimization was stopped) both probability and fidelity were still increasing, so, one can assume that even higher values of P and F are achievable, given appropriate

computational resources. In what follows, the best optimized pulse ($\alpha = 40.1$, $P = 0.999905$, $F = 0.999837$) is analyzed.

3.4.1 Analysis of unaltered optimized pulse

Shape of the optimized pulse $\varepsilon(t)$ is presented in Fig. 3.1. The field switches "on" and "off" smoothly, reaching the level of $\sim 6 \times 10^6$ V/m closer to the middle of the pulse. Although the frequency of the field is very high, and the peak-to-peak oscillations can't be resolved in Fig. 3.1, the pulse envelope is relatively smooth. Overall, in time-domain the pulse contains six clearly identified peaks, with only four dominant structures.

In order to analyze frequency content of the optimized pulse we used standard techniques of the FFT. In time domain our pulse consists of 300,001 points. The first point is at $t = 0$ and the last point is at $t = T$, where the field amplitude is exactly restricted to zero by means of the penalty function $s(t)$ as discussed above. The last point of the pulse was removed to ensure periodicity of the signal.
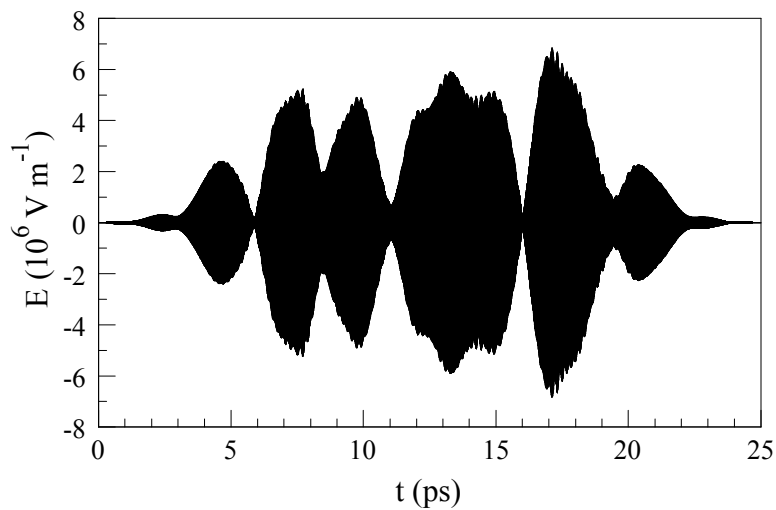
Figure 3.1: Laser pulse optimally shaped for CNOT gate (time domain).

The remaining 300,000 values of the field $\varepsilon(t)$ were used to define real parts of the complex signal. Imaginary parts of the complex signal were filled by zeros. This complex signal was Fourier-transformed into the frequency domain, giving 150,000 independent positive frequency components from $v_{min} = \Delta v = 1.35 \text{ cm}^{-1}$ to $v_{max} = 200,231 \text{ cm}^{-1}$ (and the corresponding 149,999 negative frequency components, plus one point at $v = 0$). The indicated value of v_{max} is very large, due to small time-propagation step Δt.

Discussion in the next section will emphasize that only the narrow part of spectrum (within the transition frequency range of the system) carries all physically relevant information. Indeed, first glance at the full frequency spectrum of the Fourier transformed pulse shows that amplitudes of the frequency components that lie in the range $26,850 \pm 40 \text{ cm}^{-1}$ are significantly higher than the rest of the spectrum. This part of spectrum is depicted in Fig. 3.2.

The spectrum of optimized pulse is dominated by three peaks that closely correspond to transition frequencies between the gateway state and states $|01\rangle$, $|10\rangle$ and $|11\rangle$ of the two-qubit system (blue sticks). In contrast, near the frequency of transition to state $|00\rangle$ the amplitude is very small. This is understood, due to nature of the gate CNOT, expressed by Eq. (3.2.1). Namely, the result of acting with CNOT gate onto state $|00\rangle$ is to leave the qubit unchanged (see Eq. (3.2.1a)) and the trivial solution for that is to not disturb the population of this state.

The OCT algorithm is capable of recognizing this, and excluding the frequency of $|G\rangle$-to-$|00\rangle$ transition from the pulse. Analysis of state populations during the pulse shows that, indeed, the optimized CNOT field hardly affects population of state $|00\rangle$.

Even in the cases of other three optimized transitions, Eqs. (3.2.1b-d), the population of state $|00\rangle$ remains unchanged (unpopulated in those cases) during the entire duration of the pulse.
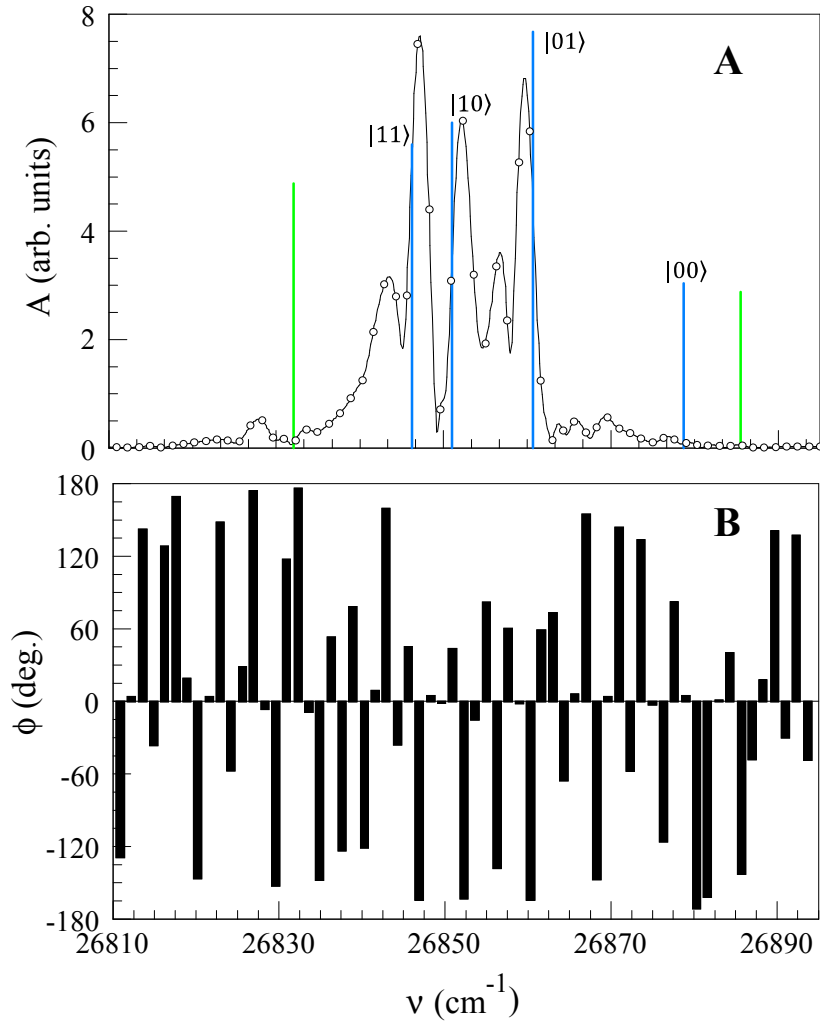
Figure 3.2: Results of Fourier transform of the optimized pulse in the narrow frequency range (64 channels). Panel A shows amplitudes of frequency components. Four transition frequencies for computing states (molecular eigenstates used to encode two-qubit system) are indicated by blue sticks. Transition frequencies for two interfering eigenstates are also shown, by green sticks. Heights of these sticks are proportional to the corresponding transition dipole moments. Panel B shows phases of frequency components.

One could expect same behavior for state $|01\rangle$ since CNOT gate transforms this state into itself as well (see Eq. (3.2.1b)). However, Fig. 3.2 shows an intense peak at this frequency, and we found that population of state $|01\rangle$ is changing significantly during all four optimized transitions of Eq. (3.2.1), even during the seemingly trivial CNOT $|01\rangle \rightarrow |01\rangle$ transition. This happens because state $|01\rangle$ is energetically closer to states $|10\rangle$ and $|11\rangle$ and its dipole moment is the largest. As result, this transition interferes significantly with other optimized transitions. The OCT algorithm can't exclude the corresponding frequency from the pulse, and has to optimize the transitions needed to control it. In contrast to this, state $|00\rangle$ discussed above lies furthest in energy and possesses smallest dipole moment (see Fig. 3.2).

Other features of spectrum in Fig. 3.2 include an intense broad wing on the low-frequency side, and a less intense wing on the high frequency side. Note, however, that the frequencies of transitions to the interfering states (green sticks) are completely suppressed by the OCT pulse optimization.

Finally, we looked at dynamics of population transfer between the qubit states during action of the optimized pulse. During this process state populations evolve very similar to what is illustrated in Fig. 3.3. From the figure 3.3 one can notice that state populations change smoothly, despite highly oscillatory behavior of the electric field of the pulse applied to the molecule (compare to Fig. 3.1). Here we will analyze in detail one of the optimized transitions, CNOT $|10\rangle \rightarrow |11\rangle$ (panel C on Fig. 3.3), see Eq. (3.2.1c). The population dynamics is not entirely monotonic, with some populations going up and down, but the overall picture is quite transparent. Figure 3.3C shows that during the initial ~ 3 ps, when the field smoothly rises, the populations stay almost

constant. Next, we observe the transfer of population from the initial state $|10\rangle$ into the gateway state $|G\rangle$. In the middle of the pulse population of $|G\rangle$ reaches ~ 0.6. At this point the population of target state $|11\rangle$ starts increasing (due to transfer from the gateway state) and does it rather monotonically. The "passive" state of the qubit, state $|01\rangle$, also receives some population during the pulse (up to ~ 0.2), but at the end of the pulse its population is entirely transferred to the target state, so that this process is well controlled. The other "passive" state $|00\rangle$ remains unpopulated for the reasons discussed above. Populations of the "interfering" states (in the vicinity of "computing" states of the two-qubit system) do not exceed 10^{-2} during the pulse, and they vanish almost entirely at $t = T$. During the last ~ 3 ps of the pulse the field smoothly decreases and no population transfer occur.

The population dynamics during the other optimized transition, CNOT $|11\rangle \rightarrow |10\rangle$ (Fig. 3.3D), is very similar to the CNOT $|10\rangle \rightarrow |11\rangle$ dynamics discussed in the previous paragraph, simply because these two processes represent the reverse of each other. Dynamics of the other two optimized transitions is simpler. Namely, if the initial qubit state is $|00\rangle$ then all the populations remain almost unaffected by the pulse (within 2×10^{-3}) (see Fig. 3.3A), which is a trivial scenario for CNOT $|00\rangle \rightarrow |00\rangle$ consistent with discussion at the beginning of this section. If the initial state is $|01\rangle$, the pulse induces some temporary excitation of $|G\rangle$, $|10\rangle$ and $|11\rangle$ (up to ~ 0.65), but it is returned back to $|01\rangle$ at the end of the pulse, consistent with CNOT $|01\rangle \rightarrow |01\rangle$ (see Fig. 3.3B). Again, in all cases populations of the interfering states do not exceed 10^{-2} during the pulse action.
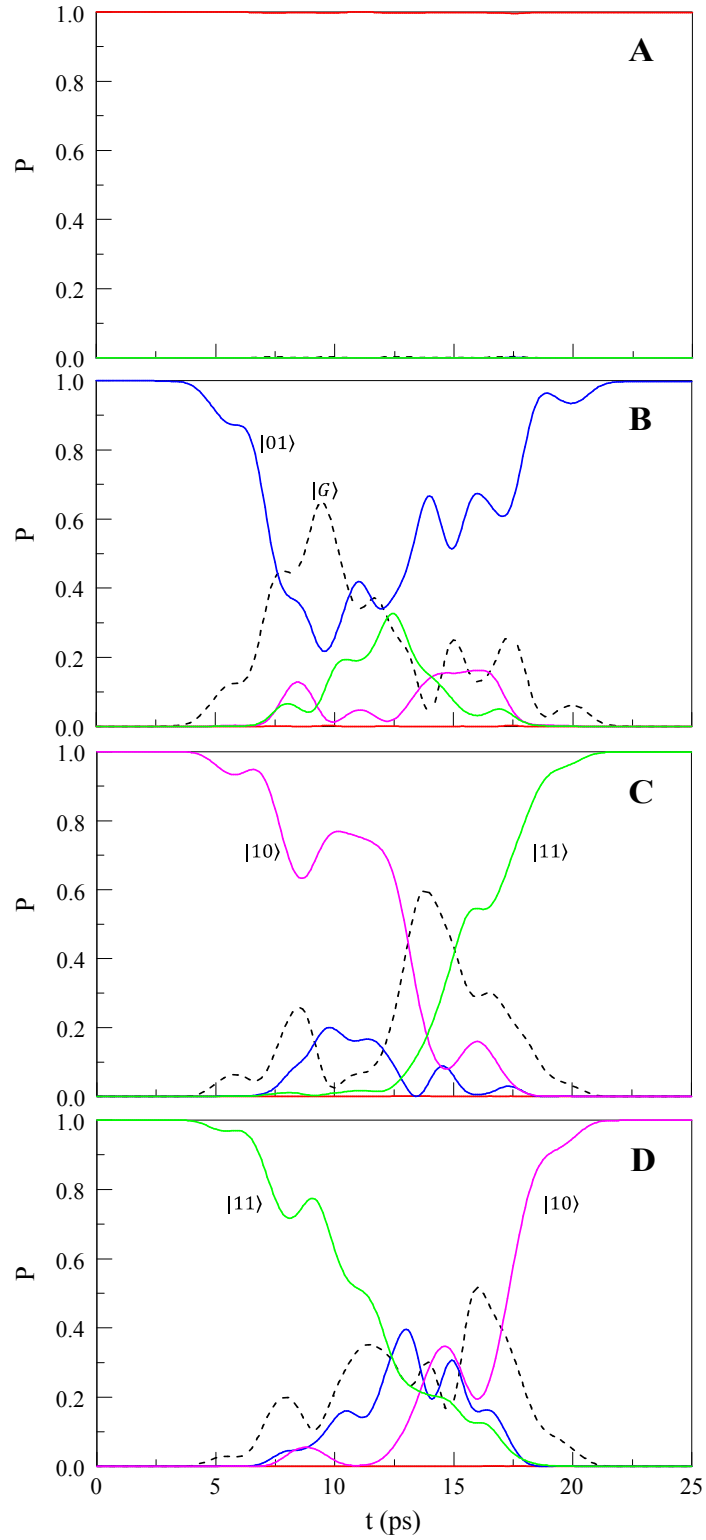
Figure 3.3: Dynamics of state populations during transformation of the two-qubit system for the case of 32 frequency channels. Transformations shown: A) CNOT $|00\rangle \to |00\rangle$, B) CNOT $|01\rangle \to |01\rangle$, C) CNOT $|10\rangle \to |11\rangle$, D) CNOT $|11\rangle \to |10\rangle$.

3.4.2 Effect of reduced bandwidth

The main goal of this work was to determine the requirements on frequency spectrum of the laser pulse (which also reflects requirements on characteristics of the pulse-shaper instrument) to achieve accurate and robust qubit transformations. In this section we study the effect of reducing bandwidth, by removing some of the frequency components from the optimized pulse. We do this by Fourier-transforming optimal pulse into frequency domain as discussed above, zeroing some of the amplitudes (at those frequencies that we want to remove), and Fourier-transforming the resultant filtered spectrum back to the time domain, producing new filtered laser pulse. Then, this new pulse is applied to the molecule in various initial states of the two-qubit system to perform four independent transitions of the CNOT gate, according to Eq. (3.2.1). For action of the filtered pulse the values of P and F are determined, and the time-dependent analysis of state populations is performed, in order to see the effect of modifications made.

As mentioned above, the unfiltered optimized pulse contains 150,000 frequency components in a very broad, physically irrelevant frequency range (see 1st row of Table 3.3). We tried to remove frequencies that do not contribute to qubit transformations by gradually narrowing frequency range of the pulse. Results of these tests are presented in Table 3.3. First, we tried to keep only those frequency components that correspond to state-to-state transitions in our system -- 352 frequency components in the 470 cm^{-1} wide range (see 2nd row of Table 3.3).

Table 3.3: Fidelities of CNOT gate for pulses with narrowed frequency range. First row shows results for the original optimized field without any filtering.

Left border (cm^{-1})	Right border (cm^{-1})	Number of frequency channels	Fidelity
1.35	200,231	150,000	0.999838
26,623	27,093	352	0.999838
26,815	26,895	64	0.999838
26,832	26,875	32	0.998953
26,845	26,862	13	0.846798

As expected, no changes of P or F, or the underlying state-to-state dynamics were observed. Next, we tried to cut off more from the spectrum, leaving only 64 unchanged frequency channels around the central frequency. This part of spectrum corresponds to Fig. 3.2 and is only 80 cm^{-1} wide. The results are given in 3rd row of Table 3.3 and, again, are entirely identical to those of unfiltered optimal pulse. Note that this frequency range contains, besides four states of the two- qubit system, two "interfering" vibrational states -- one on each side of the spectrum (green sticks in Fig. 3.2). In the next test we tried to remove even these two frequencies, reducing the number of frequency channels to just 32, which corresponds to the 43 cm^{-1} wide frequency range, shown in Fig. 3.4A. Note that this modification cuts-off two small spectral structures at the ends of the left and right wings of the optimized spectrum (see Fig. 3.4A). The results of this test are summarized in 4th row of Table 3.3, and we see that it leads to a reduction of gate fidelity. This demonstrates quite clearly that controlling transitions to the interfering states is important if one wants to obtain very accurate quantum gates. In the final test of this series we tried

to filter the spectrum as shown in Fig. 3.4B, keeping only the intense peaks in the spectrum (13 frequency channels) and removing both wings entirely. The results, summarized in 5th row of Table 3.3, show a significant drop in gate fidelity. This was expected since we removeda number of frequency components with relatively high amplitudes, in particular from the low-frequency side of spectrum (see Fig. 3.4B). Still, the gate CNOT is meaningful ($F > 0.8$).
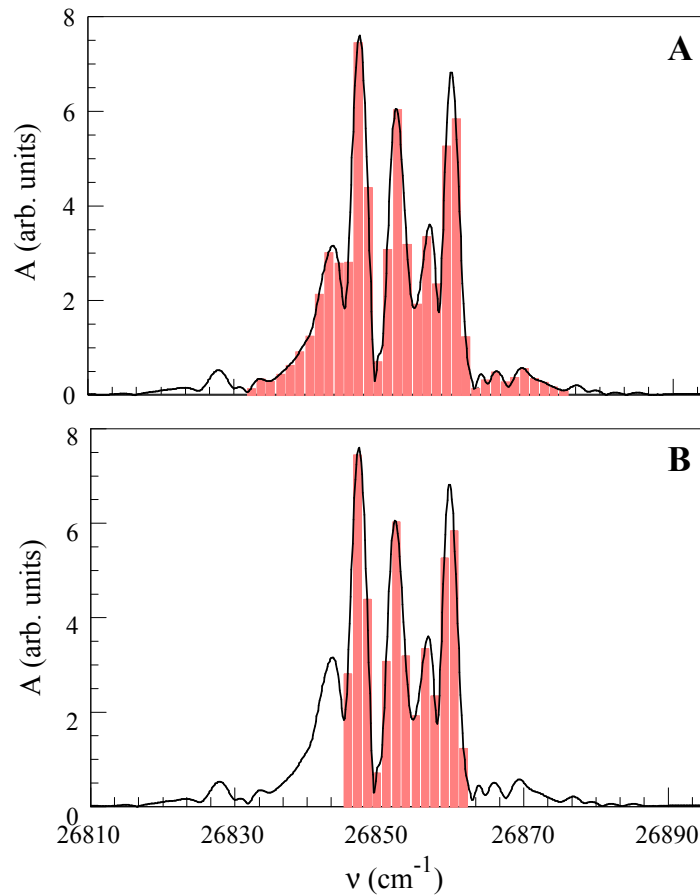
Figure 3.4: Frequency content of the filtered pulses. Panel A shows the case of 32 frequency channels. Panel B shows the case of only 13 frequency channels kept.

To gain further insight into the mechanism of fidelity loss in this test we analyzed the underlying population dynamics. The results are presented in Fig. 3.5, and can be directly compared to the high-fidelity 32-channels result of Fig. 3.3. Population dynamics of transition CNOT $|00\rangle \rightarrow |00\rangle$ look almost identical in both cases and for that reason it wasn't included in Fig. 3.5. To do comparison in details we take a look at transition CNOT $|10\rangle \rightarrow |11\rangle$ (Fig. 3.3C and Fig. 3.5B). In these two cases the population dynamics is similar during the first half of the pulse. The difference starts showing up at about $t =$ 15 ps, when the 13-channel case exhibits second increase of population of the gateway state. At the end of the pulse, in both cases, population of the gateway state is dumped onto the qubit states, but, in the 13-channel case some residual population is found in states $|10\rangle$ and $|01\rangle$, which explains low fidelity. Further analysis of the 13-channel case showed that no population has been transferred to the interfering states. This leads to conclusion that the erroneous population of the computing states of the two-qubit system is the main factor for fidelity loss in the case of the narrow-filtered pulse.

In the next series of tests we tried to understand the role of "wings" of the spectrum. For this purpose we filtered the optimized pulse by removing from the original spectrum either high-frequency, or low-frequency components only. Namely, the frequency spectrum shows two small peaks and a wide wing on the low-frequency side; on the high-frequency side, the spectrum shows four weak narrow peaks (see Fig. 3.2A). We wanted to check the importance of each of these structures by filtering them out one by one, and applying such filtered pulses to the molecule in a manner described above. The results of this series of tests are summarized in Table 3.4. Removing the low-frequency parts of spectrum maintains fidelity $F > 0.998$, up to the cut-off value of $v =$

26,835 cm^{-1}, where the wide wing begins (see Fig. 3.2A). Removing this wing results in

$F \sim 0.85$.
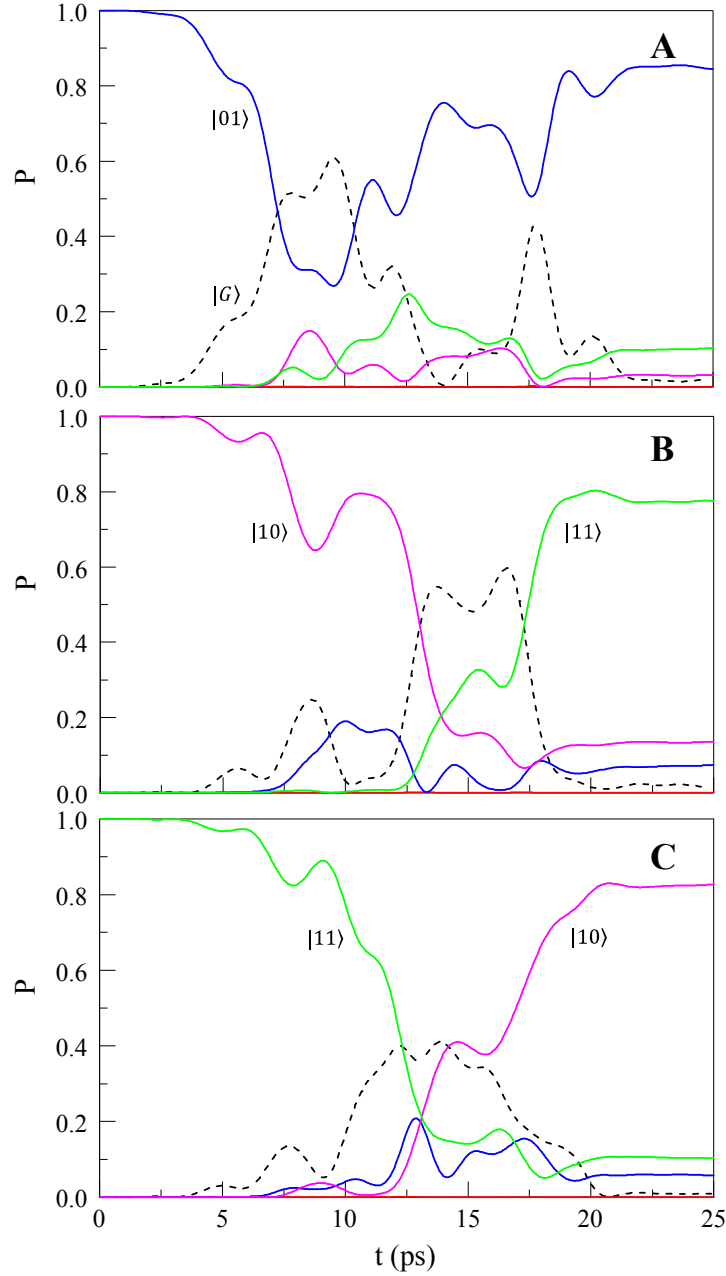
Figure 3.5: Dynamics of state populations during transformation of the two-qubit system for the case of 13 frequency channels. Transformations shown: A) CNOT $|01\rangle \rightarrow |01\rangle$, B) CNOT $|10\rangle \rightarrow |11\rangle$, C) CNOT $|11\rangle \rightarrow |10\rangle$.

Table 3.4: Fidelities of CNOT gate for pulses with frequency range narrowed from one side.

Cutoff method	Cutoff frequency (cm⁻¹)	Gate fidelity
Low-frequency	26,830	0.999410
	26,835	0.998365
	26,845	0.852487
High-frequency	26,880	0.999807
	26,875	0.999582
	26,868	0.998777
	26,865	0.998024
	26,862	0.960835

Removing only a part of this structure still results in significant decline of fidelity. On the high-frequency side we performed more tests, due to larger number of minor peaks. Fidelity of the filtered pulse remains at the level $F > 0.998$, up to the cutoff value of $v = 26,865 \, \text{cm}^{-1}$, when all but one minor peaks are removed. Removing this last peak reduces fidelity to $F \sim 0.96$. Therefore we can conclude that most important is to keep one minor peak (adjacent to the major peak) on each side of the spectrum. Including the more remote peaks is important only if the fidelity in excess of $F \sim 0.998$ is desired.

On the practical side, it is very encouraging and is almost surprising that with only 64 frequency channels we are able to achieve (in calculations) highly-accurate quantum gate CNOT. In fact, even with 32 channels, when we control just transitions between states of the two-qubit system and ignore the interfering transitions, we can

achieve a reasonable gate fidelity, closely approaching $F = 0.999$, which is well sufficient for the first proof-of-principle experiment.

3.4.3 Effect of amplitude errors

The second goal of this work was to determine how sensitive the results of molecule-pulse interaction are to deviations of pulse's shape from the ideal optimal shape. The first parameter to study is pulse's amplitude. We tried to construct new modified pulses, from the optimal one, by changing the values of amplitudes of all frequency components simultaneously, by a given amount. Figure 3.6 illustrates the results of increasing and, alternatively, decreasing the amplitudes by up to 10% of the optimal values. We observed monotonic decrease of fidelity of the gate CNOT in both cases. The effect is well described by quadratic function:

$$F = 1 + a|\Delta A| - b|\Delta A|^2. \qquad (3.4.1)$$
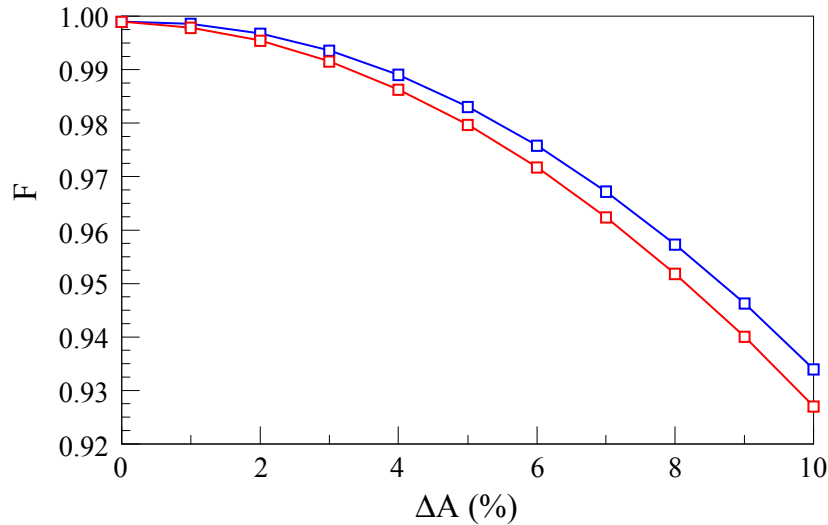
Figure 3.6: Fidelity of CNOT gate as a function of deviation of pulse's amplitude from its optimal value. Blue and red symbols correspond to increased and decreased amplitudes, respectively.

The values of fitting parameters are $a = 1.16 \cdot 10^{-4}$, $b = 6.65 \cdot 10^{-4}$ for positive ΔA and $a = 4.91 \cdot 10^{-4}$, $b = 6.75 \cdot 10^{-4}$ for negative ΔA values. For example, when the values of amplitudes are changed by 3-4%, the fidelity stays relatively high, at the level of $F \sim 0.99$. Even a very significant deviation from the optimal amplitude, like by $\pm 10\%$ or so, still results in the meaningful results characterized by $F \sim 0.93$. Since both positive and negative deviations lead to similar decreases of gate fidelity, one could hope that a random noise (with both positive and negative deviations of amplitudes of different frequency components occurring simultaneously) will not lead to larger decrease of fidelity. To check this assumption we carried out a series of 50 additional calculations where the amplitude of each frequency component underwent random error in the range from -5 to $+5\%$ of its optimal value. These randomly modified pulses were independently applied to the molecule. The fidelity, averaged over 50 runs, was $F = 0.998416$ which is significantly higher than the values obtained with systematically positive ($F = 0.983093$ for $+5\%$ error) or systematically negative ($F = 0.979696$ for -5% error) values. Thus, the results presented in Fig. 3.6 can be considered as "the worst case scenario" and serve as lower bound for estimation of fidelity loss due to amplitude errors.

3.4.4 Effect of phase errors

The last question to explore is the effect of phase errors. For this purpose we took the values of phases of different frequency components of the optimized pulse (see Fig.3.2B), and tried to modify them by rounding their values to a set of discrete equally spaced values in the range $-180° < \varphi < +180°$. The coarseness of phase rounding in our tests varied from only $\Delta \varphi = 1°$, up to $\Delta \varphi = 90°$ (see Fig. 3.7). Rounding phases of

the optimized pulse components introduces phase errors. For example, for $\Delta\varphi = 30°$ the optimal phases are modified by up to $\pm 15°$. Using the intrinsic routine NINT( ) of FORTRAN this rounding operation would be written as:

$$\bar{\varphi} = \Delta\varphi \cdot \text{NINT}\left(\frac{\varphi}{\Delta\varphi}\right), \tag{3.4.2}$$

where φ is the optimized value of phase and $\bar{\varphi}$ is value of phase after rounding.

When the rounding is very coarse it becomes important which discrete values of phases are chosen. For example, for $\Delta\varphi = 90°$ one can chose $\varphi = \{-90°,\ 0,\ 90°,\ 180°\}$ or, alternatively, the values of $\varphi = \{-135°, -45°,\ 45°, 135°\}$ obtained from the first set through $\Delta\varphi/2$ rotation. We tried both methods of rounding for each studied value of $\Delta\varphi$.
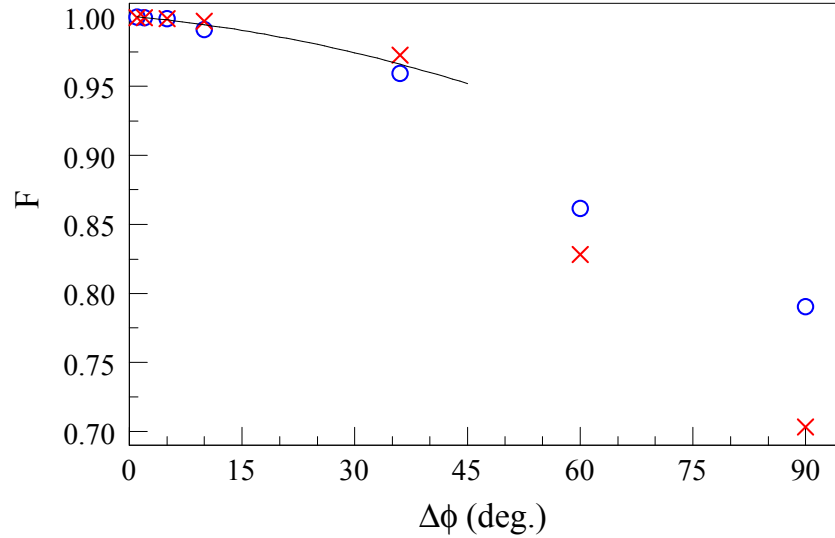
Figure 3.7: Fidelity of CNOT gate as a function of phase rounding error. Blue and red symbols correspond to two different ways of rounding (see text for further details). Solid curve shows analytic fit by quadratic function.

Our results for gate CNOT are summarized in Fig. 3.7. We see that as $\Delta\varphi$ increases, the value of gate fidelity F gradually drops. For example, relatively large phase errors introduced by $\Delta\varphi = 30°$ lead to only modest decrease of fidelity, down to $F \sim 0.97$. In the high fidelity region of Fig. 3.7 the results of simulations can be approximated by a quadratic function of the form:

$$F = 1 - a \cdot \Delta\varphi - b \cdot (\Delta\varphi)^2, \qquad (3.4.3)$$

with $a = 4.88 \cdot 10^{-4}$, $b = 1.32 \cdot 10^{-5}$.

When phases of frequency components of the optimal pulse are modified, the dynamics of state-to-state transitions also changes. Figure 3.8 illustrates this effect in the case of $\Delta\varphi = 60°$. This figure can be compared to Fig. 3.3 and Fig. 3.5. The effect of phase errors (Fig. 3.8) is different from the effect of reduction of number of frequency channels (Fig. 3.5).

Interestingly, for transition CNOT $|10\rangle \rightarrow |11\rangle$ phase errors lead to residual population of the gateway state $|G\rangle$ and reduced population of the target state $|11\rangle$, while populations of states $|01\rangle$ and $|10\rangle$ (and of the interfering states) are all accurately controlled.
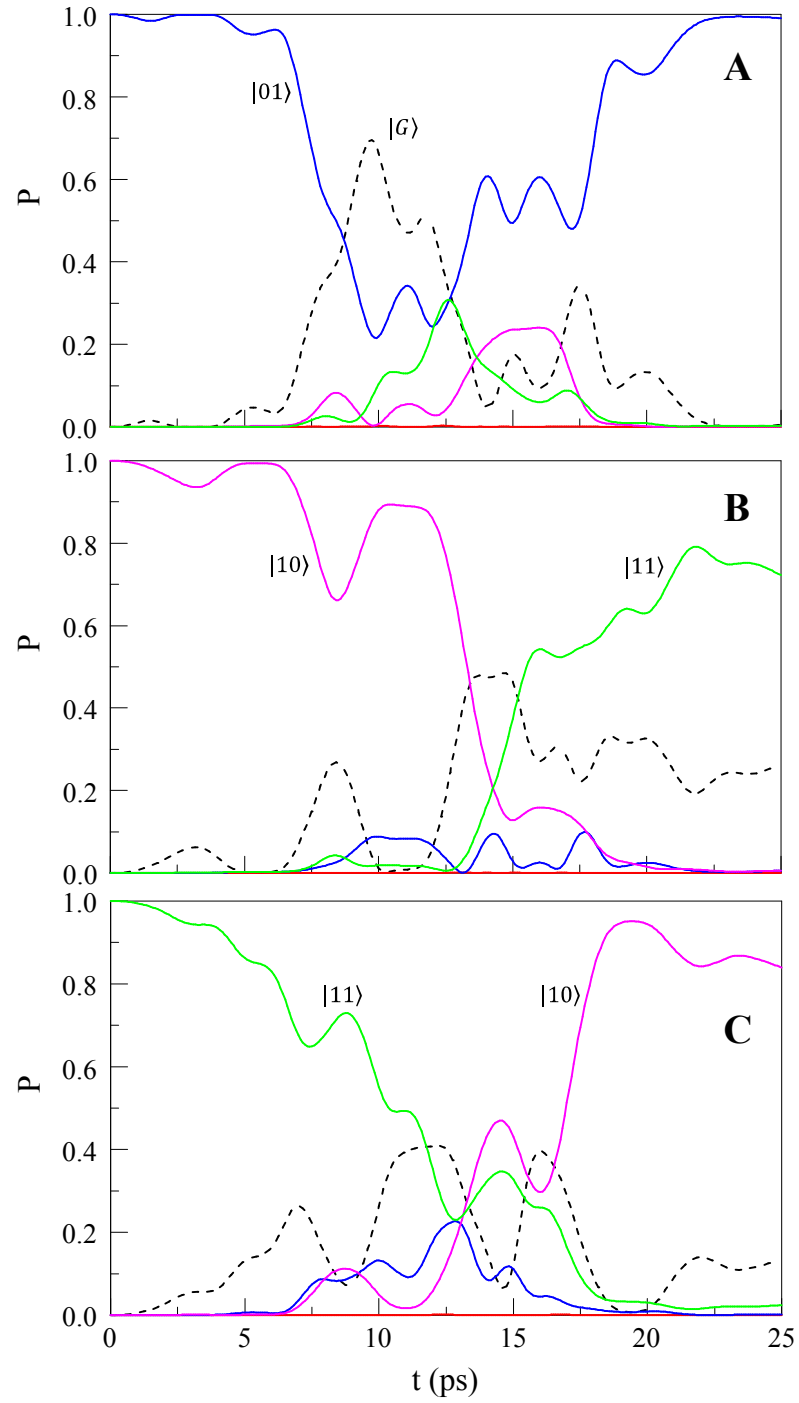
Figure 3.8: Dynamics of state populations during transformation of the two-qubit system for the case of 32 frequency channels in the presence of phase coursing with $\Delta\varphi = 60°$. Transformations shown: A) CNOT $|01\rangle \rightarrow |01\rangle$, B) CNOT $|10\rangle \rightarrow |11\rangle$, C) CNOT $|11\rangle \rightarrow |10\rangle$.

3.5 Conclusions

The purpose of this computational work is exploratory, rather than predictive. We do not really expect that the CNOT pulse obtained here by calculations can be exactly reproduced in the experiment and can lead to exactly the same result under experimental conditions. However, we feel it is reasonable to expect that employment of an advanced experimental pulse optimization technique, such as feedback loop with evolutionary algorithm, may lead to experimental result of acceptable quality. Computational results outlined in this paper could serve as prediction of a reasonable set of requirements for the pulse spectrum and, consequently, for the pulse shaping equipment. We found that the number of frequency channels needed for accurate two-qubit gate is not large. Calculations showed that 32 frequency channels may be well sufficient for moderate fidelity of qubit transformations, $F\sim0.999$. This result is reliable, because it is based on realistic experimental spectrum and transition moments of thiophosgene. If the frequency resolution Δv (defined by the pulse length T) is kept fixed, increasing the number of channels beyond 32 is not expected to be beneficial. However, it may be beneficial to increase the number of frequency components (within the same bandwidth) simultaneously with improving frequency resolution Δv. Effect of pulse shaping errors was studied separately for amplitudes and phases of frequency components. Moderate errors in amplitudes (within $\pm4\%$ of the optimal values) and phases (within $\pm5°$ of the optimal values) are not expected to reduce fidelity of qubit transformations below $F\sim0.99$, indicating favorable path to experimental implementation.

In calculations, such laser pulses can be readily constructed using OCT. Although the OCT has a huge bandwidth initially available for pulse construction, and there are no any constraints on use of this bandwidth, the optimal pulses come out restricted to surprisingly small bandwidth. The most intense frequency components are resonant to frequencies of controlled transitions, but the off-resonant wings on both sides of spectrum appear to be important for accurate qubit transformations. Transitions to energetically remote interfering states are simply avoided by OCT, through suppressing field amplitude at the corresponding frequencies, which is probably the main reason for small bandwidth of the optimized pulses. When we tried to limit the original bandwidth (manually, in the frequency domain) to only 64 frequency channels, we did not observe any decay of the pulse fidelity at the level of six significant figures: the gate average probability of CNOT remained at the level of > 0.9999, while the phase sensitive gate fidelity was very close to this value. This does bode well for robust solutions.

References for Chapter 3

1. W. Zhu, J. Botina, and H. Rabitz, *J. Chem. Phys.* **108**, 1953 (1998).

2. W. Zhu and H. Rabitz, *J. Chem. Phys.* **109**, 385 (1998).

3. H. Rabitz, M. Hsieh, C. Rosenthal, *Science* **303**, 1998 (2004).

4. E. Berrios, M. Gruebele, D. Shyshlov, L. Wang, and D. Babikov, J. Phys. Chem. A, **116**, 46 (2012).

5. H. Rabitz, R.de Vivie-Riedle, M. Motzkus, K. Kompa, *Science* **288**, 824 (2000).

6. A. Assion, T. Baumert, M. Bergt, T. Brixner, B. Kiefer, V. Seyfried, M. Strehle, G. Gerber, *Science* **282**, 919 (1998).

7. R. Bartels, S. Backus, E. Zeek, L. Misoguti, G. Vdovin, I. P. Christov, M. M. Murnane and H. C. Kapteyn, *Nature* **406**, 164 (2000).

8. D. Weidinger and M. Gruebele, *Mol. Phys.* **105**, 1999 (2007).

9. R. R. Zaari and A. Brown, *J. Chem. Phys.* **135**, 044317 (2011).

10. W. Zhu and H. Rabitz, *J. Chem. Phys.* **118**, 6751 (2003).

11. J. P. Palao and R. Kosloff. *Phys. Rev. Lett.* **89**, 188301 (2003).

12. J. P. Palao and R. Kosloff, *Phys. Rev. A* **68**, 062308 (2003).

13. C. M. Tesch, L. Kurtz, and R. de Vivie-Riedle, *Chem. Phys. Lett.* **343**, 633 (2001).

14. C. M. Tesch and R. de Vivie-Riedle, *Phys. Rev. Lett.* **89**, 157901 (2002).

15. U. Troppmann, C. M. Tesch, and R. de Vivie-Riedle, *Chem. Phys. Lett*. **378**, 273 (2003).

16. C. M. Tesch and R. de Vivie-Riedle, *J. Chem. Phys*. **121**, 12158 (2004).

17. B. Korff, U. Troppmann, K. Kompa, and R. de Vivie-Riedle, *J. Chem. Phys.* **123**, 244509 (2005).

18. U. Troppmann and R. de Vivie-Riedle, *J. Chem. Phys.* **122**, 154105 (2005).

19. U. Troppmann, C. Gollub, and R. de Vivie-Riedle, *New J. Phys.* **8**, 100 (2006).

20. Z. Amitay, R. Kosloff, and S.R. Leone, *Chem. Phys. Lett.* **359**, 8 (2002).

21. D. Babikov, *J. Chem. Phys.* **121**, 7577 (2004).

22. J. Vala, Z. Amitay, B. Zhang, S.R. Leone, and R. Kosloff, *Phys. Rev. A* **66**, 062316 (2002).

23. Y. Ohtsuki, *Chem. Phys. Lett.* **404**, (2005).

24. S. Suzuki, K. Mishima, and K. Yamashita, *Chem. Phys. Lett*. **410**, 358 (2005)

25. .Y. Teranishi, Y. Ohtsuki, K. Hosaka, H. Chiba, H. Katsuki, and K. Ohmori, *J. Chem. Phys.* **124**, 114110 (2006).

26. D. Weidinger and M. Gruebele, *Chem. Phys*. **350**, 139 (2008).

27. T. Cheng and A. Brown, *J. Chem. Phys*. **124**, 34111 (2006).

28. M. Schröder and A. Brown, *J. Chem. Phys*. **131**, 034101 (2009).

29. R. R. Zaari and A. Brown, *J. Chem. Phys*. **132**, 014307 (2010).

30. R. R. Zaari and A. Brown, *J. Chem. Phys*. **132**, 014307 (2010).

31. M. Zhao and D. Babikov, *J. Chem. Phys*. **126**, 204102 (2007).

32. Y. Y. Gu and D. Babikov, *J. Chem. Phys*. **131**, 034306 (2009).

33. B. Strickler and M. Gruebele, *Phys. Chem. Chem. Phys.* **6**, 3786 (2004)

34. T. Laarmann, I. Shchatsinin, P. Singh, N. Zhavoronkov, M. Gerhards, C. P. Schulz, and I. V. Hertel, *J. Chem. Phys*. **127**, 201101 (2007).

35. M. Kotur, T. Weinacht, B. J. Pearson, and S. Matsika, *J. Chem. Phys*. **130**, 134311 (2009).

36. A. Nemeth, F. Milota, T. Mančal, V. Lukeš, J. Hauer, H. F. Kauffmann, and J. Sperling, *J. Chem. Phys*. **132**, 184514 (2010).

37. A. du Plessis, C. A. Strydom, H. Uys, and L. R. Botha, *J. Chem. Phys*. **135**, 204303 (2011).

38. M. A. Nielsen and I. L. Chuang, *Quantum Computation and Quantum Information* (Cambridge University Press, Cambridge, 2000).

39. M. Zhao and D. Babikov, *J. Chem. Phys*. **125**, 024105 (2006).

40. M. Zhao and D. Babikov, *Phys. Rev. A* **77**, 012338 (2008).

41. L. Wang and D. Babikov, *Phys. Rev. A* **83**, 022305 (2011).

42. L. Wang and D. Babikov, *Phys. Rev. A* **83**, 052319 (2011).

43. L. Wang and D. Babikov, *J. Chem. Phys.* **137**, 064301 (2012).

44. J. I. Cirac and P. Zoller, *Phys. Rev. Lett.* **74**, 4091 (1995).

45. D. M. Meekhof, C. Monroe, B. E. King, W. M. Itano, and D. J. Wineland, *Phys. Rev. Lett*. **76**, 1796 (1996).

46. K. Sundermann and R. de Vivie-Riedle, *J. Chem. Phys*. **110**, 1896 (1999)

Chapter 4: On readout of vibrational qubits using quantum beats

4.1 Introduction

Quantum computation can be implemented by using shaped ultrafast laser pulses to control population transfer between molecular vibrational states [1-46]. In one type of implementation, a set of 2^n vibrational eigenstates in a molecule can represent n qubits that are inherently entangled [4], encoding several qubits on a single molecule, as shown in Fig. 4.1. High-fidelity quantum gates [2,3,9,16,17,40] and simple quantum algorithms [8,13,20,30,41] have been investigated computationally for 2-5 vibrational qubits per molecule, scaling up by a useful amount the number of qubits per information carrier over atomic two-level systems [20].

The result of a quantum computation leaves n qubits encoded in the superposition of 2^n computational states. But how do we read out the state of vibrational qubits to complete the computation carried out in a molecule? The goal of the readout step is to obtain information about populations and phases of the computational states. It can be achieved by employing quantum beat spectroscopy as follows. The superposition of the computational qubit states is pumped to a single readout state by a time-delayed laser pulse. Fluorescence from the readout state is then detected. Repeating this for different time delays one obtains a periodic quantum beat signal (see insert in Fig. 4.1) from which populations and relative phases of the computational states can be extracted by fitting this signal with analytic expression.

This readout scheme is destructive, meaning that molecules in a beam, once excited to the readout state, lose their qubit information and cannot be excited again with a different time delay. We see two ways of circumventing this problem. One is to repeat preparation of the qubit system, which can be done reliably with modern pulsed lasers and beam-cooled molecules. The overhead (number of readouts) will depend on the total frequency bandwidth ΔE and on the smallest difference δE among pairwise vibrational state energy differences roughly as $\Delta E/\delta E \cdot \ln(\Delta E/\delta E)$ if a fast Fourier transform algorithm is used to extract frequency components. This overhead is fixed and is not very large for 2-5 vibrational qubits. Alternatively, it is possible to reduce the pulse power in order to excite only a small fraction of the molecules from the beam, which will permit reading out from the same ensemble of molecules several times, with different time delays. Moreover, other approaches to the readout of vibrational qubits, such as non-destructive wave packet interferometry [47], can also be considered in the future.

Another often discussed requirement to practical quantum computation is scaling – opportunity to increase the number of qubits to hundreds or even thousands [48,49]. The prototypes of quantum computers created so far are still rather small. Latest achievements include fourteen entangled qubits in the ion trap [50], five superconducting qubits [51], and only two atomic qubits in an optical lattice [52]. Our goal with molecular qubits is not to replace methods such as atomic or ion trapping, but to enhance them by allowing 2-5 qubits per carrier instead of a single qubit. The possibility of encoding more than one qubit has been demonstrated computationally for molecular ions [23]. It seems quite feasible to create in the experiment a system of few vibrational qubits, fully entangled and well separated from the environment [4]. Such prototype systems by

themselves also could be used in the fundamental studies of quantum control, noise effects, decoherence, *etc*. For these small-scale (or test-bed) applications, the quantum beat approach to the readout, discussed in this paper, is also quite appropriate.

We consider the readout process using thiophosgene molecule, $SCCl_2$ shown in Fig. 4.1, as our model for a molecular carrier of several qubits. This molecule has already been
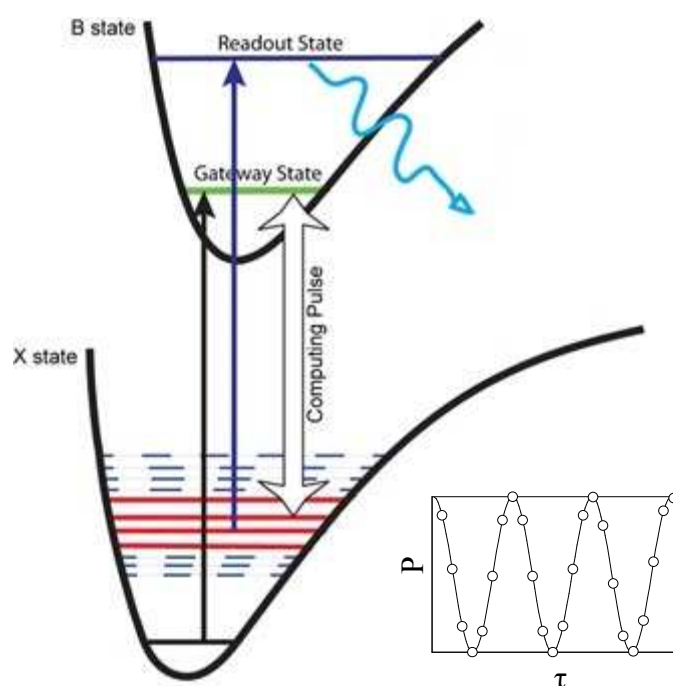
Figure 4.1: The model of molecular qubits is thiophosgene $SCCl_2$. Red lines show computational qubit states, dashed lines show vibrational eigenstates closest to the qubit states. Initialization is done by a laser pulse that excites molecule to the gateway state. The computational step is performed by a shaped laser pulse that circles population between the qubit states and an electronically excited gateway state until the final superposition is obtained. After computational step is finished the superposiotion of qubit states is excited to the readout state with time-delayed laser pulse. Fluorescence from the readout state is analyzed to extract information about populations and relative phases of qubit states. The insert demonstrates an example of quantum beat signal from one qubit, where circles indicate results of calculations and solid line is a numerical fit.

studied extensively as a platform for qubit manipulation, including such aspects as effects of rotation and laser power on population transfer [20], optimal shape of high-fidelity computational pulses [42] and their robustness [43], although readout has not been considered in detail before. Computational states (qubits, or q-words) are encoded in the vibrationally excited states in the ground electronic state of thiophosgene. The process of quantum computation itself is performed by a shaped laser pulse that cycles population between the computational states and the electronically excited "gateway" state (see Fig. 4.1). The shape of this computational pulse is optimized to implement a particular quantum gate [42], or an algorithm [20]. Another electronically excited state is used as a readout state. The difference in energy between the ground state, the readout state and the computational states allows convenient UV/vis laser pulses to be used. Thus there is no direct population transfer between the computational states, and only transitions from the computational states and to the readout state are significant.

As the simplest model system for the readout, we include two computational states in our calculations to study readout from one vibrational qubit, and four states for readout from the vibrational two-qubit system. The energy spectrum and transition dipole moments of our model are taken from the experiment [53,54] and are given in Table 4.1. The intensity of fluorescence from the readout state is linearly proportional to its population. Thus, we will analyze theoretically and computationally the population of the readout state after interaction with the time-delayed readout pulse.

Table 4.1: Energy spectrum and transition dipole moments of the computational states and the readout state in the model of thiophosgene molecule.

State		Energy, cm^{-1}	Transition moment, D	One-qubit assignment	Two-qubit assignment
Readout		36025	—		
Computational states	1	9197.0	0.174	$|0\rangle$	$|00\rangle$
	2	9230.7	0.176	$|1\rangle$	$|01\rangle$
	3	9247.1	0.185		$|10\rangle$
	4	9271.1	0.166		$|11\rangle$

The amplitudes and relative phases of computational states can be determined in principle by fitting the quantum beat signal with an analytical expression. In the simplest case of readout from one qubit we would need to determine the amplitudes of two computational states A_1 and A_2 and a single phase difference $\Delta\varphi$. To do that we need to fit the quantum beat signal with the analytical expression, obtained based on time-dependent perturbation theory [55]:

$$P(\tau) = K \cdot \left(\varepsilon_1{}^2\mu_1{}^2 A_1{}^2 + \varepsilon_2{}^2\mu_2{}^2 A_2{}^2 + 2\varepsilon_1\mu_1 A_1\varepsilon_2\mu_2 A_2 \cos(\Delta E\tau - \Delta\varphi)\right), \quad (4.1.1)$$

where ε_1 and ε_2 are laser pulse intensities at frequencies of transitions from two computational states to the readout state, μ_1 and μ_2 are corresponding transition dipole moments, $\Delta E = E_2 - E_1$ is the energy difference between the computational states in angular frequency units, τ is the variable time delay, and K is a fitting coefficient. Similar ideas have been implemented in the past for readout of the electron-spin qubits in the solid-state environments, such as a doped diamond crystal or a semiconductor quantum dot [56,57]. The origin of Eq. (4.1.1) is investigated in Appendix 4.1.

Variations of expression (4.1.1) are featured in a variety of publications on quantum beat spectroscopy [55,58-60]. Applications of quantum beat spectroscopy to molecules are usually focused on determining the energy difference ΔE [55,58-59] or on the extraction of population distribution [60], but rarely on the phase factor $\Delta\varphi$ [61]. Our goal is to extract the values of amplitudes of the computational states, A_1 and A_2, and of the phase difference between them, $\Delta\varphi$ (see Eq. (4.1.1)). The phase is a critical piece of information about the qubit-encoding states, and thus the state of the qubits they represent.

The goal of this paper is two-fold. One is to investigate the possibility of accurate determination of amplitudes and phase difference from Eq. (4.1.1) for quantum beat signals obtained from superpositions of vibrational states. Determining and, if possible, expanding the range of applicability of this simple formula also is important for many other applications of the quantum beat spectroscopy [55,58-60]: while exact numerical simulations are quite possible on modern computers in many cases, simple analytical models can provide additional insight. The second goal is to test Eq. (4.1.1) computationally in the application to a qubit readout, using parameters of a suitable real molecule (thiophosgene) and realistic parameters of the readout pulse. In this paper we use numerical simulation in order to mimic the process of experimental readout. Namely, we first produce the quantum beat signal numerically, using wavepacket propagation techniques, for some (known) final state of the vibrational qubit, or qubits. Then, we try to fit this signal with the expression (4.1.1) above in order to extract the values of A_1, A_2 and $\Delta\varphi$, now assumed to be unknown (the values of energies are assumed to be known, e.g., from another experiment). Repeating this procedure for various final qubit states, various pulse parameters, and even for various vibrational states used to represent qubits,

we can determine the accuracy of this readout procedure. Our important finding is that using the known formula (4.1.1) for the fit does not allow determining the phase accurately. We analyze the origin of this phase error and propose a simple fix to the problem.

4.2. Numerical propagation

To determine the result of interaction of the molecular system with a laser pulse we propagate the Schrödinger equation

$$i\hbar \frac{\partial}{\partial t}\Psi(t) = \left[\widehat{H}_0 - \mu\varepsilon(t)\right]\Psi(t), \tag{4.2.1}$$

in the quantum representation for the molecule and the classical representation for the field. The initial condition of these equations is given by the state of the qubit we want to read out. To expand the time-dependent wave function we use the vibrational eigenfunctions of the system $\psi_n(x)$ with the corresponding energy eigenvalues E_n and time-dependent coefficients $c_n(t)$:

$$\Psi(x,t) = \sum_{n=1}^{N} c_n(t) \cdot \psi_n(x) \cdot e^{-iE_n t}. \tag{4.2.2}$$

Substitution Eq. (4.2.2) into Eq. (4.2.1) leads to the equations for the coefficients $c_n(t)$:

$$\dot{c}_n^R(t) = \varepsilon(t) \sum_m \left(c_m^R(t) \sin\theta_{m,n} - c_m^I(t) \cos\theta_{m,n}\right) \cdot M_{m,n}, \tag{4.2.3a}$$

$$\dot{c}_n^I(t) = \varepsilon(t) \sum_m \left(c_m^R(t) \cos\theta_{m,n} - c_m^I(t) \sin\theta_{m,n}\right) \cdot M_{m,n}, \tag{4.2.3b}$$

where $\theta_{m,n} = (E_m - E_n)t$ are phase shifts, $M_{m,n} = \langle \psi_m | \mu | \psi_n \rangle$ are the elements of the dipole moment matrix and c_m^R and c_m^I are the real and imaginary parts of the complex coefficient c_m. At the end of the quantum computation, and just before interaction with the readout pulse, they represent the final state of vibrational qubit [22].

Population transfer from the qubit states to the readout state depends on the choice of the laser pulse $\varepsilon(t)$. We consider the readout pulse to be a transform-limited Gaussian pulse, created in the frequency domain:

$$\varepsilon(\omega) = \varepsilon_\omega \exp\left(-\frac{(|\omega| - \Omega)^2}{2\sigma^2}\right), \tag{4.2.4}$$

where Ω is the center frequency, ε_ω is the amplitude and σ is the width of the pulse in the frequency domain. The center frequency of the readout pulse Ω was set in the middle of two transition frequencies because for such a pulse the field intensities on both transition frequencies are equal. To obtain the time profile of the pulse $\varepsilon(t)$ we need to Fourier transform Eq. (4.2.4). Since the pulse must be purely real in the time domain, we need to prepare symmetrical pulse profile in the frequency domain. Therefore we include negative frequencies in Eq. (4.2.4) and after Fourier transform we obtain a pulse that is real in the time domain:

$$\varepsilon(t) = \varepsilon_\omega \frac{\sigma}{\sqrt{2\pi}} \exp\left(-\frac{\sigma^2 t^2}{2}\right) \cos \Omega t. \tag{4.2.5}$$

We can rewrite Eq. (4.2.5) for simplicity as:

$$\varepsilon(t) = \varepsilon_0 f(t) \cos \Omega t, \tag{4.2.6}$$

where we introduced

$$\varepsilon_0 = \varepsilon_\omega \frac{\sigma}{\sqrt{2\pi}} \tag{4.2.7}$$

and

$$f(t) = \exp\left(-\frac{\sigma^2 t^2}{2}\right). \tag{4.2.8}$$

Here ε_0 is the pulse amplitude in the time domain, Ω is a carrier frequency and $f(t)$ is the pulse envelope in the time domain, also a Gaussian.

The frequency resolution of the readout pulse is fixed at $2\ cm^{-1}$ (a typical value for the experimental setup and ro-vibrational profiles of SCCl$_2$). Frequency resolution determines pulse duration $T = 16.68\ ps$, however duration of the highest intensity part of the pulse is significantly shorter ($\sim 100\ fs$). The time grid for propagation was set in the range $\left(-{}^T/_2\ ,\ {}^T/_2\right)$, while the pulse reaches its peak at $t = 0$. The time delay between the shaped computation pulse (whose optimal shape was derived previously [42,43]) and the readout pulse is simply taken into account by the phases of the qubit-encoding vibrational eigenstates (their phases evolve freely after the computation pulse is over while the population in each qubit encoding state remains constant.)

Equations (4.2.3a-b) are propagated using the Runge-Kutta method of 4th order. To study the readout from one qubit we included $N = 3$ basis functions in Eq. (4.2.2), to account for two computational states and the readout state. This is the minimal number of states required for numerical test of Eq. (4.1.1). For readout from a two-qubit system we included all five states given in Table 4.1. In principle, one could study the influence of

the interfering vibrational states of the molecule onto the readout process, by including more states into the basis set expansion, but this was not our goal here.

We tried two fitting methods. In one of them, we used four independent tuning parameters in Eq. (4.1.1): K, A_1, A_2 and $\Delta\varphi$, to fit the quantum beat signal one qubit, and normalized A_1 and A_2 after the fitting. In the second method we had only three independent fitting parameters: K , A_1 and $\Delta\varphi$, while A_2 was computed from normalization as $A_2 = \sqrt{1 - A_1{}^2}$. We found that both methods produced identical results and, finally, adopted the second one, with smaller number of independent fitting parameters.

4.3. Results and analysis

For calculations with one qubit the central frequency of the readout pulse was chosen at $\Omega = 26811.15 \, cm^{-1}$, which is the middle between two frequencies for transitions from computational states 1 and 2 to the readout state (see Table 4.1). Other parameters of the readout pulse were: the amplitude $\varepsilon_\omega = 32 \, a.u.$ and the width $\sigma = 200 \, cm^{-1}$ in the frequency domain, which corresponds to the experimentally feasible pulse amplitude in the time domain $6 \times 10^9 \, V/m$, low enough to avoid ionization or excessive excited state absorption. The first set of numerical experiments was carried out for a model system (not a thiophosgene molecule), where we could vary energies of the computational states E_1 and E_2 in order to check how the energy difference ΔE affects the fitting of the quantum beat signal. Calculations with ΔE varying in the range from $15 \, cm^{-1}$ to $135 \, cm^{-1}$ are presented here. Note that for four states of thiophosgene in

Table 4.1 the value of ΔE varies in the range from $16.4 \ cm^{-1}$ to $74.1 \ cm^{-1}$, with $\Delta E =$ $33.7 \ cm^{-1}$ for states 1 and 2 chosen here to represent one qubit. So, the results of such model calculations are very relevant to the molecule we are studying. The energy of the readout state was fixed and equal to that of thiophosgene (see Table 4.1). For simplicity, the state of the qubit was an equally weighted superposition of computational states, $A_1 = A_2 = \frac{1}{\sqrt{2}}$, with no phase difference, $\Delta \varphi = 0$.

Once the simulation was run and the fit to equation (4.1.1) performed, we calculated the amplitude error as $\delta A = \frac{|A_{1f} - A_1|}{1.00} \times 100\%$, where A_1 is the exact (known) amplitude, and A_{1f} is an amplitude obtained by fitting. The phase error was calculated as $\delta \varphi = \frac{\Delta \varphi_f - \Delta \varphi}{360°} \times 100\%$, where $\Delta \varphi$ is the exact (known) phase difference, and $\Delta \varphi_f$ is a phase difference obtained by fitting. Our results are presented in Figs. 4.2 and 4.3. We found that the amplitude error δA of the fitting increases roughly exponentially with energy difference ΔE (see Fig. 4.2), but the value of δA remains relatively small even for large ΔE and does not exceed $10^{-2}\%$ in our tests. For energy difference between computational states 1 and 2 in thiophosgene, $\Delta E = 33.7 \ cm^{-1}$ (see Table 4.1), the amplitude error would be $\sim 5 \times 10^{-3}\%$. Thus, we can confidently conclude that it should be possible to determine the values of amplitudes of the qubit states with high precision.

However, we found that the value of phase error $\delta \varphi$ is significantly higher than that of the amplitude error. Figure 4.3 shows that $\delta \varphi$ increases roughly linearly with energy difference ΔE and reaches almost 5% at $\Delta E = 135 \ cm^{-1}$. For thiophosgene with $\Delta E = 33.7 \ cm^{-1}$ the phase error would be $\sim 1.2\%$. We also performed a series of fitting

tests for non-zero values of the phase difference $\Delta\varphi$ between the qubit states, increasing it gradually up to $180°$ (all with $A_1 = A_2 = \frac{1}{\sqrt{2}}$).
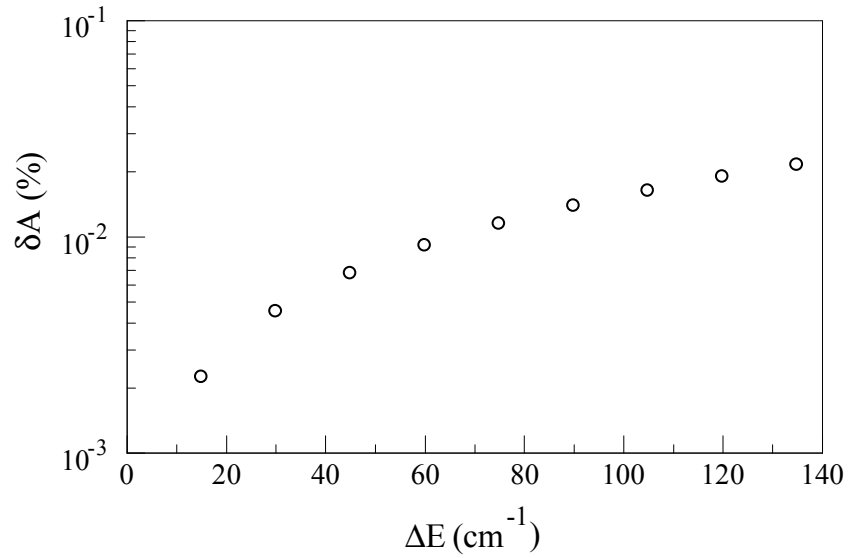
Figure 4.2: Amplitude error as a function of energy difference between computational states in a model system. Pulse amplitude is at $\varepsilon_\omega = 32\ a.u.$ Pulse width is $\sigma = 200\ cm^{-1}$.
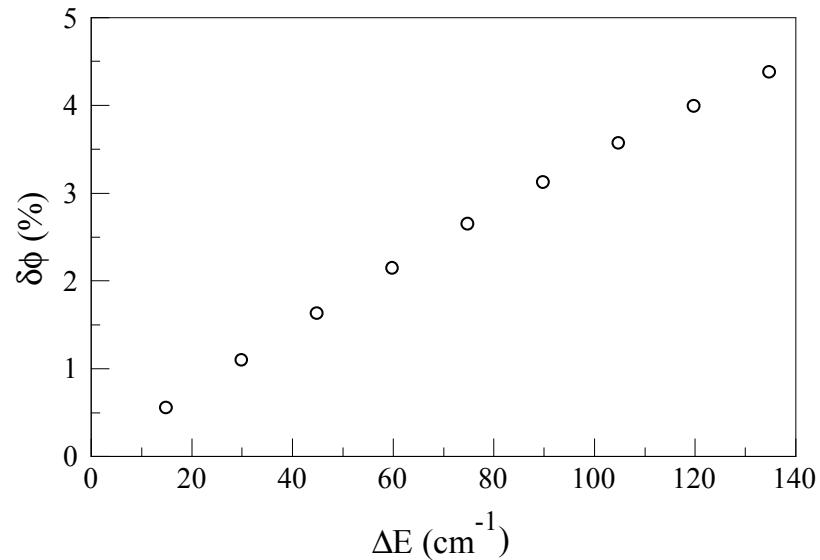
Figure 4.3: Phase error as a function of energy difference between computational states in a model system. Pulse amplitude is at $\varepsilon_\omega = 32\ a.u.$ Pulse width is $\sigma = 200\ cm^{-1}$.

In all those tests we found that phase error $\delta\varphi$ does not depend on the value of phase difference $\Delta\varphi$ itself, but depends on energy difference ΔE, and the dependence $\delta\varphi(\Delta E)$ is nearly identical to that in Fig. 4.3 (*i.e.*, close to linear). In order to check whether this non-negligible phase error $\delta\varphi$ depends on pulse parameters we then performed a series of fitting tests for a system with constant energy difference $\Delta E = 30 \ cm^{-1}$ by varying parameters of the readout pulse, such as width in the frequency domain σ and amplitude ε_ω. The quantum beat signals obtained in those calculations again were fitted using expression (4.1.1). The dependence of phase error on the pulse width σ is shown in Fig. 4.4A (for pulse amplitude fixed at $\varepsilon_\omega = 32 \ a.u.$) and one can see that pulses with larger σ give lower phase error in the fitting. According to Eq. (4.2.4) and (4.2.5), the pulse width σ in the frequency domain corresponds to the pulse width $1/\sigma$ in the time domain. Therefore, the value of inversed pulse width $1/\sigma$ is a parameter that describes duration of the pulse. The dependence of phase error $\delta\varphi$ on the inverse pulse width $1/\sigma$ is shown on Fig. 4.4B. The dependence is nearly linear and we can conclude that longer readout pulses with a narrower frequency profile result in a larger phase error.
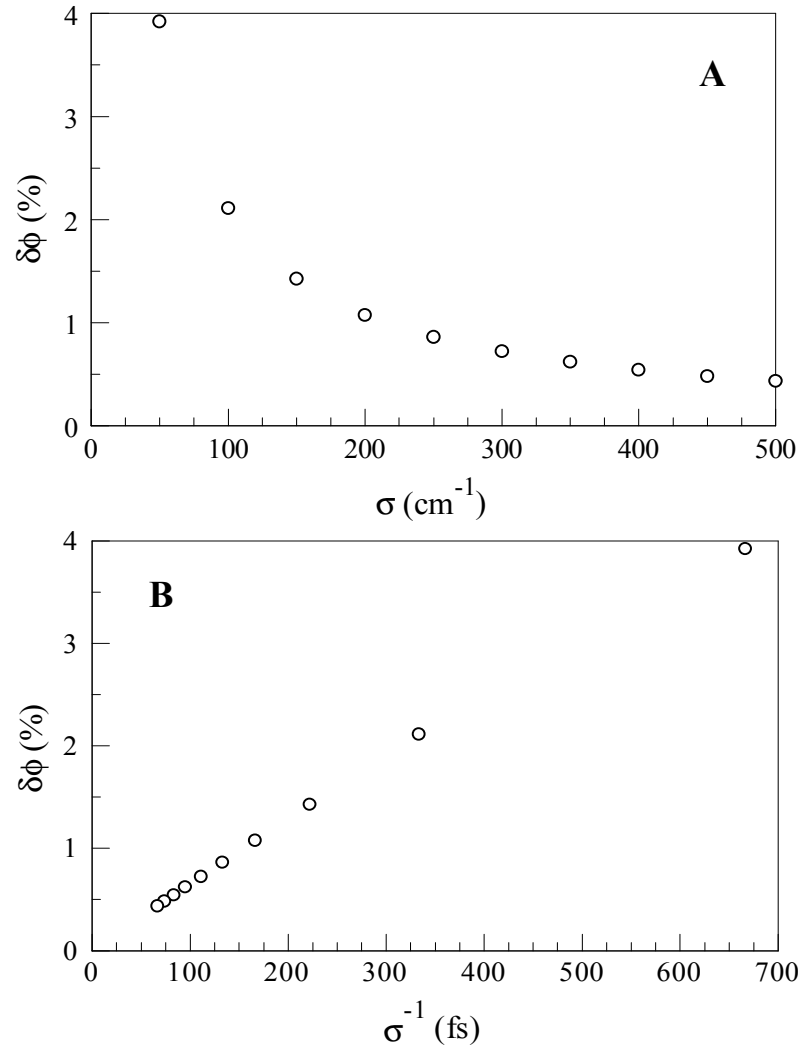
Figure 4.4: Phase errors obtained for different values of the width of the readout pulse (in the frequency domain). Frame A shows dependence of phase error on pulse width, while frame B shows dependence on the inversed width as a parameter of pulse duration (in time domain). Energy difference between the computational states is $\Delta E = 30\ cm^{-1}$. Pulse amplitude is fixed at $\varepsilon_\omega = 32\ a.u.$

In order to study dependence of the phase error $\delta\varphi$ on the pulse amplitude ε_ω we fixed the pulse width at $\sigma = 200\ cm^{-1}$, and varied the value of pulse amplitude ε_ω in Eq. (4.2.7) through the range shown in Fig. 4.5. For each case we carried out an independent calculation and determined the value of $\delta\varphi$. We found that pulses with larger amplitudes results in larger phase errors and, through the studied range of values, the dependence is close to exponential. The phase error is on the order of $\delta\varphi \approx 2\%$ for $\varepsilon_\omega < 40\ a.u.$, but it drastically increases for larger values of pulse amplitudes, and, reaches $\delta\varphi \approx 50\%$ for $\varepsilon_\omega = 65\ a.u.$ This illustrates that the phase error we observed and studied may be significant even for pulse energies relevant to experiment.
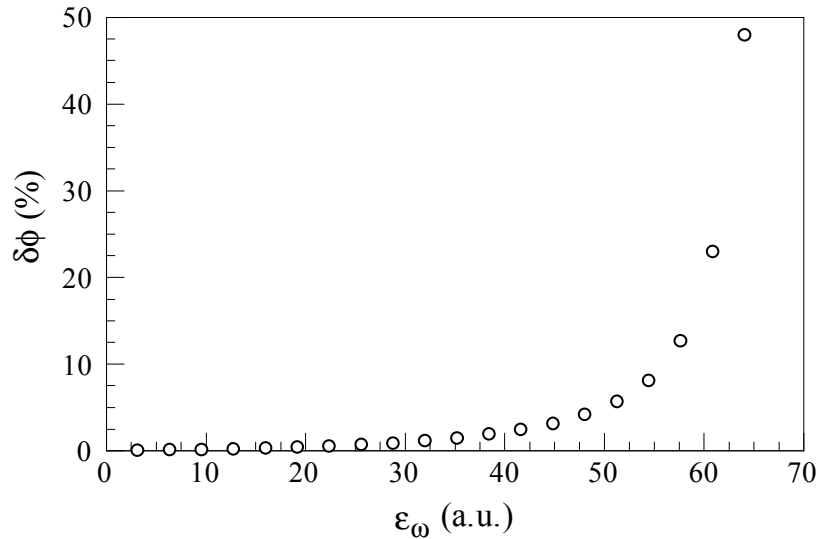
Figure 4.5: Phase errors obtained for different values of the amplitude of the readout pulse (in the frequency domain). Energy difference between the computational states is $\Delta E = 30\ cm^{-1}$. Pulse width is fixed at $\sigma = 200\ cm^{-1}$.

We conclude from these results that the origin of the phase error is in the fact that the readout pulse has non-zero duration and fluence, violating the assumptions of time-dependent perturbation theory used in Ref. [55]. According to Eq. (4.2.2) a phase shift should occur between states 1 and 2, and it would be more pronounced for longer pulses and larger energy differences ΔE, consistent with our observations. Therefore, the quantum beat signal obtained with a readout pulse of finite duration (rather than sudden pulse) in a system with non-degenerate levels ($\Delta E \neq 0$) includes an additional phase shift. There is no such a phase shift in Eq. (4.1.1), which results in a phase error during fitting. In order to decrease this error one may want to use shorter readout pulses, which corresponds to increasing pulse width σ in the frequency domain, as well as using pulses with lower amplitude or choosing states with smaller energy difference ΔE to represent qubits. However, the ideal case of an arbitrarily low pulse power and an arbitrarily short pulse duration cannot be achieved in real experiments. Typical to our experimental set up, and to gas-phase molecule fluorescence detection in general, are $10 - 100 \, \mu J$ pulses of duration $\sim 100 \, fs$ focused to a Gaussian waist of $w \sim 10 \, \mu m$. The peak electric field they produce is $E_{peak} \sim 10^{10} \, V/m$, which corresponds to $\varepsilon_\omega \sim 150 - 450 \, a.u.$ in Eqs. (4.2.4-4.2.5). From Fig. 4.5 we see that at such conditions the phase error is significant, unfortunately.

On a practical note, the readout scheme considered here has the advantage that background effects in the readout can be eliminated. The readout is a single photon, relatively low-field measurement, whose lowest power is determined by the signal-to-noise ratio required to detect fluorescence and fit the quantum beats. The measurements of jet-cooled thiophosgene $\tilde{X} \rightarrow \tilde{B}$ excitation in a time-of-flight mass spectrometer show

negligible ionization for 285 nm (tripled output of a regenerative amplifier) as well as for the visible pulses ~400 nm that have been proposed for readout of excited vibrational states in the $\tilde{X}$ electronic state to the $\tilde{B}$ electronic state [20]. The main practical problem for both ns and fs excitation pulses is the excited state absorption from the readout state in the $\tilde{B}$ electronic state. This reduces the population in the readout state that can be monitored by fluorescence or stimulated emission pumping [62]. It does not produce a fluorescence signal that interferes with readout because the highly excited states decay non-radiatively. For this reason, the calculations proposed here correspond to maximum E-fields in the time domain of $10^9 - 10^{10}$ V/m, close to experimental fields that produce strong fluorescence signals but not excessive ionization or excited state absorption. As discussed above, the low peak intensities are advantageous because they minimize the exponential growth of phase error with probe-pulse energy, but in practice they need to be high enough to allow fluorescence detection of quantum beats.

So, instead of reducing the pulse power, we propose to compensate for phase error by calculating it numerically for a given system (ΔE) and pulse parameters ($\varepsilon_\omega, \sigma$) and introducing it explicitly into the fitting expression (4.1.1) as a constant phase correction term φ_{corr}:

$$P(\tau) = K \cdot \left(\varepsilon_1{}^2 \mu_1{}^2 A_1{}^2 + \varepsilon_2{}^2 \mu_2{}^2 A_2{}^2 \right.$$

$$\left. + 2\varepsilon_1 \mu_1 A_1 \varepsilon_2 \mu_2 A_2 \cos(\Delta E \tau - \Delta \varphi + \varphi_{corr}) \right). \qquad (4.3.1)$$

Using the fitting expression (4.3.1) with phase correction φ_{corr} allows us to fit the phase $\Delta \varphi$ between the computational states with high precision. In order to do that we would need, first, to fit one quantum beats signal produced numerically for one arbitrary

set of initial conditions (A_1, A_2 and $\Delta\varphi$) using expression (4.1.1) in order to determine the phase error φ_{corr} specific to energy difference of computational states ΔE and parameters of the readout pulse ε_ω and σ. This phase error does not depend on state populations (A_1, A_2) or on their phase difference $\Delta\varphi$ and can be used in expression (4.3.1) to fit all the quantum beats signals produced from the given system with the given readout pulse. In particular, this procedure can be used to analyze the experimental quantum beats signal to derive A_1, A_2 and $\Delta\varphi$ in the experimentally implemented quantum computation, based on theoretically (numerically) derived value of φ_{corr}.

We tested the fitting approach proposed above using states 1 and 2 of thiophosgene, $\Delta E = 33.7\ cm^{-1}$ (see Table 4.1) and the pulse with $\Omega = 26811.15\ cm^{-1}$, $\varepsilon_\omega = 32\ a.u.$ and $\sigma = 200\ cm^{-1}$. First, using the amplitudes $A_1 = A_2 = \frac{1}{\sqrt{2}}$ and the phase difference $\Delta\varphi = 0$ we produced one quantum beat signal and fitted it by Eq. (4.1.1) to determine the value of $\varphi_{corr} = 4.42°$. Next, we produced a number of different quantum beat signals for the same qubit and pulse, but with various populations of qubit states and various phase differences. Many combinations of $A_1 = \sqrt{0.9},\ \sqrt{0.8},\ \sqrt{0.7}, ...\ ,$ $\sqrt{0.1}$ (and $A_2 = \sqrt{0.1},\ \sqrt{0.2},\ \sqrt{0.3}, ...\ ,\ \sqrt{0.9}$, respectively) with phase differences $\Delta\varphi = 0°,\ 22.5°,\ 45°, ...\ ,\ 180°$ were tried, which covers the surface of Bloch sphere with 81 sample points (by an 9×9 grid). All these quantum beat signals were fitted using the expression (4.3.1) with $\varphi_{corr} = 4.42°$. These tests confirmed that using the fitting expression (4.3.1), with properly determined phase correction, reduces phase error below $10^{-9}\%$ for any arbitrary state of vibrational qubit. Thus, our correction method is universally applicable to any output of the quantum computation procedure.

In order to test that this correction procedure will be valid for the pulses of higher intensities also, we have repeated all the tests described in the previous paragraph with several higher intensity readout pulses, up to the ionization limit estimated as $E_{peak} \sim 2.3 \times 10^{11} \ V/m$, or $\varepsilon_\omega = 1226 \ a.u.$ We found that the phase correction φ_{corr}, determined for a given pulse and one arbitrarily chosen state of the qubit, remains universal and works for any other state of the qubit, as long as the same readout pulse is used, up to ionization limit of thiophosgene.

The same approach of fitting the quantum beat signal with phase correction can be used in order to readout a state of a two-qubit system, implemented using four vibrational states. To perform readout from four vibrational states one would need to determine four amplitudes: $A_1, A_2, A_3,$ and A_4, and six phase differences between each pair of computational states: $\Delta\varphi_{12}$, $\Delta\varphi_{13}$, $\Delta\varphi_{14}$, $\Delta\varphi_{23}$, $\Delta\varphi_{24},$ and $\Delta\varphi_{34}$. The fitting expression for two-qubit system is:

$$P(\tau) = K \cdot \left(\sum_{i=1,4} \varepsilon_i^2 \mu_i^2 A_i^2 \right.$$

$$\left. +2 \sum_{i=1,3} \sum_{j=i+1,4} \varepsilon_i \mu_i A_i \varepsilon_j \mu_j A_j \cos\left(\Delta E_{ij}\tau - \Delta\varphi_{ij} + \varphi_{corr_{ij}}\right) \right), \quad (4.3.2)$$

where we introduced four phase corrections. Energies and transition dipole moments of vibrational states of thiophosgene we used in our calculations are given in Table 4.1. Parameters of the readout pulse were: $\Omega = 26788.53 \ cm^{-1}$ (average of four transition frequencies), $\varepsilon_\omega = 32 \ a.u.$ and $\sigma = 200 \ cm^{-1}$. First, we calculated the quantum beat signal for equally weighted superposition superposition $A_1 = A_2 = A_3 = A_4 = \frac{1}{\sqrt{2}}$, with

no phase differences $\Delta\varphi_{12} = \Delta\varphi_{13} = \Delta\varphi_{14} = \Delta\varphi_{23} = \Delta\varphi_{24} = \Delta\varphi_{34} = 0$. This signal was fitted using Eq. (4.3.2) in order to find the values of phase corrections for each oscillating term: $\varphi_{corr_{12}} = 12.59°$, $\varphi_{corr_{13}} = 18.87°$, $\varphi_{corr_{14}} = 27.83°$, $\varphi_{corr_{23}} = 6.28°$, $\varphi_{corr_{24}} = 15.23°$, $\varphi_{corr_{34}} = 8.95°$. Fitting with phase correction was then applied to a number of quantum beat signals, generated from an arbitrary superposition of computational states with different amplitudes and phase differences. Values of the phase error determined by fitting with Eq. (4.3.2) and numerically determined phase corrections were always below 10^{-9}%. These result confirm that accurate fitting of relative phases of computational states is possible in the case of the readout from a system of more than one vibrational qubit.

4.4. Conclusions

In this theoretical/computational work we explored the process of readout from vibrational qubits in thiophosgene molecule, SCCl₂, using quantum beat oscillations. It is assumed that the quantum beats are obtained by excitation of a superposition of the qubit states with time delayed pulses to the electronically excited readout state, followed by detecting oscillations of population of the readout state, through fluorescence, as a function of time delay of the readout pulse. We found that a significant phase error is obtained if the known analytic expression for quantum beats from time-dependent density matrix perturbation theory, Ref. [55], is used for extracting the values of probability amplitudes and relative phases of the vibrational qubit states. We discussed the source and the properties of this phase error and proposed an improved analytical expression, where a universal phase correction is introduced. Application of this new expression fixes

the phase problem and allows fitting the quantum beat signal very accurately. It should permit to readout the final states of vibrational qubits in the experiments using an approach in which the analytic expression for fitting is combined with numerical modelling of the readout process, for computing the phase correction. Thus real laser pulses of finite duration and fluence can, in principle, be used to readout vibrational qubits.

Appendix 4.1: Rabi oscillations and quantum beats

Population transfer from the computational states to the readout state depends on the choice of the laser pulse. We consider the readout pulse to be transform-limited Gaussian pulse. Our goal here is to develop an expression for computing a population of the readout state depending on populations of qubit states and parameters of the readout pulse.

As shown in Eq. (4.2.4 – (4.2.8) the Gaussian laser pulse is described as:

$$\varepsilon(t) = \varepsilon_0 f(t) \cos \Omega t, \qquad (A4.1.1a)$$

$$\varepsilon_0 = \varepsilon_\omega \frac{\sigma}{\sqrt{2\pi}}, \qquad (A4.1.1b)$$

$$f(t) = \exp\left(-\frac{\sigma^2 t^2}{2}\right), \qquad (A4.1.1c)$$

where ε_0 is the pulse amplitude, Ω is a carrier frequency, $f(t)$ is a Gaussian pulse envelope and σ is the width of the pulse in the frequency domain.

The molecule that interacts with a laser pulse can be described as a system of n states with energies E_n and dipole moments μ_n. The readout state will be indicated by a subscript 0. Wave function of the system in atomic units is:

$$\Psi(r,t) = \sum_n c_n(t) u_n(r) e^{-iE_n t}, \qquad (A4.1.2)$$

where E_n are energies of the eigenstates. Schrodinger's equation is:

$$i\dot{\Psi} = \hat{H}\Psi = (H_0 + V)\Psi, \tag{A4.1.3}$$

where V is the molecule-light interaction part of the Hamiltonian. Substitute Eq. (A4.1.2) into Eq. (A4.1.3):

$$i\sum_n (\dot{c}_n - iE_n c_n)|u_n\rangle e^{-iE_n t} = \sum_n (E_n + V)c_n|u_n\rangle e^{-iE_n t}. \tag{A4.1.4}$$

Projecting both parts of Eq. (A4.1.4) onto $\langle u_k|$ we obtain

$$i(\dot{c}_k - iE_k c_k)e^{-iE_k t} = E_k c_k e^{-iE_k t} + \sum_n c_n \langle u_k|V|u_n\rangle e^{-iE_n t}. \tag{A4.1.5}$$

$$\dot{c}_k = -i\sum_n c_n \langle u_k|V|u_n\rangle e^{-i(E_n - E_k)t}. \tag{A4.1.6}$$

$$\langle u_k|V|u_n\rangle = -\mu_{kn}\varepsilon(t) = -\mu_{kn}\varepsilon_0 f(t)\cos\Omega t. \tag{A4.1.7}$$

Combining Eq. (4.1.6) and Eq. (4.1.7) we obtain the system of coupled differential equations for coefficients c_k:

$$\dot{c}_k = i\varepsilon_0 f(t)\cos\Omega t \sum_n c_n \mu_{kn} e^{-iE_{nk}t}, \tag{A4.1.8}$$

where $\omega_{nk} = E_n - E_k$. Then we use conversion of cosine function into exponential form:

$$\cos\Omega t = \frac{1}{2}(e^{i\Omega t} + e^{-i\Omega t}) \tag{A4.1.9}$$

and using Eq. (A4.1.9) we can rewrite Eq. (A4.1.8) as

$$\dot{c}_k = \frac{i}{2}\varepsilon_0 f(t) \sum_n c_n \mu_{kn}(e^{-i(\omega_{nk}-\Omega)t} + e^{-i(\omega_{nk}+\Omega)t}). \tag{A4.1.10}$$

We can simplify the system of differential equations Eq. (A4.1.10) if we consider a particular quantum system.

Readout from a single state

The simplest case for the readout process consists of two states - one computational state and the readout state. For description of two-state case we will use subscript 0 for the readout state and subscript 1 for the qubit state. In a two-state system $\mu_{10} = \mu_{01} = \mu$ and $\omega_{01} = -\omega_{10} = \omega$. We can rewrite Eq. (A4.1.10) as a system of two coupled differential equations:

$$\dot{c}_0 = \frac{i}{2}\mu\varepsilon_0 c_1 f(t)\left(e^{i(\omega-\Omega)t} + e^{i(\omega+\Omega)t}\right), \qquad (A4.1.11)$$

$$\dot{c}_1 = \frac{i}{2}\mu\varepsilon_0 c_0 f(t)\left(e^{-i(\omega-\Omega)t} + e^{-i(\omega+\Omega)t}\right).$$

Here we use the rotating wave approximation (RWA): assuming $\omega \approx \Omega$ we can neglect rapidly oscillating terms $e^{\pm i(\omega+\Omega)t}$. With RWA and substituting $\omega - \Omega = \delta\omega$ for frequency detuning Eq. (13) becomes:

$$\dot{c}_0 = \frac{i}{2}\mu\varepsilon_0 c_1 f(t)e^{i\delta\omega t}, \qquad (A4.1.12a)$$

$$\dot{c}_1 = \frac{i}{2}\mu\varepsilon_0 c_0 f(t)e^{-i\delta\omega t}, \qquad (A4.1.12b)$$

To solve Eq. (A4.1.12) analytically we take a derivative of both parts of Eq. (A4.1.12a):

$$\ddot{c}_0 = \frac{i}{2}\varepsilon_0\mu\left(\dot{f} + i\delta\omega f\right)c_1 e^{i\delta\omega t} + \frac{i}{2}\mu\varepsilon_0 f\dot{c}_1 e^{i\delta\omega t}. \qquad (A4.1.13)$$

After substitution of c_1 from Eq. (A4.1.12a) and $\dot{c}_1$ from Eq. (A4.1.12b) into Eq. (A4.1.13) we obtain equation for c_0:

$$\ddot{c}_0 = \left(\frac{\dot{f}}{f} + i\delta\omega\right)\dot{c}_0 - \left(\frac{\mu\varepsilon_0 f}{2}\right)^2 c_0. \tag{A4.1.14}$$

Solution of Eq. (A4.1.14) can be found after the variable transformation:

$$z(t) = \frac{1}{2}\varepsilon_0\mu \int_{-\infty}^{t} f(t')dt' \tag{A4.1.15}$$

$$\dot{z} = \frac{1}{2}\varepsilon_0\mu f, \qquad \ddot{z} = \frac{1}{2}\varepsilon_0\mu\dot{f} \tag{A4.1.16}$$

In order to rewrite Eq. (A4.1.14) we need to express $\ddot{c}_0$ and $\dot{c}_0$ as functions of z. If we use notation $c_0' = \frac{dc_0}{dz}$ then

$$\dot{c}_0 = c_0'\dot{z} = c_0'\frac{1}{2}\varepsilon_0\mu f, \tag{A4.1.17a}$$

$$\ddot{c}_0 = \frac{d(c_0'\dot{z})}{dt} = c_0''(\dot{z})^2 + c_0'\ddot{z} = c_0''\left(\frac{1}{2}\varepsilon_0\mu f\right)^2 + c_0'\frac{1}{2}\varepsilon_0\mu\dot{f}. \tag{A4.1.17b}$$

Substituting Eq. (4.1.17) into Eq. (4.1.12) we obtain:

$$c_0''\left(\frac{1}{2}\varepsilon_0\mu f\right)^2 + c_0'\frac{1}{2}\varepsilon_0\mu\dot{f} = c_0'\frac{1}{2}\varepsilon_0\mu\dot{f} + i\delta\omega c_0'\frac{1}{2}\varepsilon_0\mu f - \left(\frac{\mu\varepsilon_0 f}{2}\right)^2 c_0. \tag{A4.1.18}$$

$$(c_0'' + c_0)\frac{1}{2}\varepsilon_0\mu f - i\delta\omega c_0' = 0. \tag{A4.1.19}$$

In a two-state case (one computing state + one readout state) we can chose laser pulse frequency to be in resonance with transition frequency, $\Omega = \omega$. In this case $\delta\omega = 0$ and Eq. (4.1.19) becomes

$$c_0'' + c_0 = 0. \tag{A4.1.20}$$

Solution of Eq. (A4.1.20) can be found in the general form

$$c_0(t) = \alpha \sin[z(t)] + \beta \cos[z(t)], \tag{A4.1.21}$$

where α and β are constants that can be determined from the initial conditions. Assuming that at $t = 0$ the readout state is not populated and all population is at the qubit state, or $c_0(-\infty) = 0$ and $c_1(-\infty) = 1$, we obtain:

$$c_0(t) = \alpha \sin[z(t)]. \tag{A4.1.22}$$

To find α we need to find the solution for c_1. Substitute Eq. (A4.1.22) into Eq. (A4.1.12a):

$$c_1 = \frac{\alpha}{i} \cos[z(t)] \implies c_1(0) = \frac{\alpha}{i} = 1 \implies \alpha = i. \tag{A4.1.23}$$

Therefore the solution is

$$c_0(t) = i \sin[z(t)]. \tag{A4.1.24}$$

The probability that the system is in the readout state at the time t is given by

$$P_0(t) = |c_0(t)|^2 = \sin^2\left[\frac{1}{2}\varepsilon_0\mu \int_{-\infty}^{t} f(t')dt'\right]. \tag{A4.1.25}$$

We can find expression for P_0 after pulse has interacted with the molecule, so that $t = +\infty$. Since the envelope of the laser pulse is a Gaussian function (see Eq. (A4.1.1)) we can find $z(\infty)$:

$$z(\infty) = \frac{1}{2}\varepsilon_0\mu \int_{-\infty}^{\infty} f(t')dt' = \frac{1}{2}\varepsilon_0\mu\frac{\sqrt{2\pi}}{\sigma} = \frac{1}{2}\varepsilon_\omega\mu. \qquad (A4.1.26)$$

Substituting Eq. (A4.1.26) into Eq. (A4.1.25) we will obtain the final expression of Rabi oscillations in the two-state system:

$$P_0(\infty) = \sin^2\left[\frac{1}{2}\varepsilon_0\mu\frac{\sqrt{2\pi}}{\sigma}\right] = \sin^2\left[\frac{1}{2}\varepsilon_\omega\mu\right]. \qquad (A4.1.27)$$

Population of the readout state in the two-state system interacting with the pulse in resonance with the transition depends only on pulse amplitude in the frequency domain.

As seen below, it is also desirable to have an analytic solution for the case of an arbitrary off-resonant (or a detuned) pulse. This requires solution of Eq. (A4.1.19) with $\delta\omega \neq 0$, which is not available at present. This problem needs further investigation.

We can check analytical result for population transfer computationally by propagating the system of differential equations Eq. (A4.1.6) in time. The laser pulse for numerical propagation is prepared in the frequency domain with the frequency resolution fixed at $2\ cm^{-1}$ (the value is taken from the experimental setup) and Fourier transformed into the time domain. Frequency resolution determines pulse duration $T = 16.68\ ps$, however duration of the effective part of the pulse is significantly shorter $(\sim 10^2\ fs)$. The

time grid for propagation was set in the range $\left(-{}^{T}\!/_{2}\,,\,{}^{T}\!/_{2}\right)$, where the pulse reaches its peak at $t = 0$.

Computational results for Rabi oscillations were obtained for a two-state system with the following parameters: $E_0 = 36025\ cm^{-1}$, $E_1 = 9197\ cm^{-1}$, $\mu = 0.174\ D$. Population transfer in this case does not depend on width of the pulse in the frequency domain (since the pulse is in exact resonance). We confirmed this by carrying out calculations for several values of σ in the range $10 - 1000\ cm^{-1}$. We calculated the population of the readout state after the pulse as a function of the pulse amplitude in the frequency domain ε_ω in the range $10 - 500\ a.u.$ and compared result to the analytical expression Eq. (29). For the two-state system agreement between analytical and computational results is perfect.

The lowest amplitude of the pulse that transfers all population of the computational state to the readout state is $\sim 46\ a.u.$ which corresponds to the pulse amplitude in time domain $4.3 \cdot 10^9\ V/m$ for pulse width $100\ cm^{-1}$. The period of observed Rabi oscillations is $\sim 92\ a.u.$ or $8.6 \cdot 10^9\ V/m$ for pulse width $100\ cm^{-1}$.

Readout of one-qubit system

Let's consider solving Eq. (A4.1.10) for a one-qubit system that consists of two computational states and a readout state. For description of the system we will use subscript 0 for the readout state and subscripts 1 and 2 for the qubit states.

In our model of the readout process transition between computational states is not excited by the laser pulse. Only transitions $0 \leftrightarrow 1$ and $0 \leftrightarrow 2$ between a readout state and

each of the computational states are considered. We will simplify notations as following:

$\mu_{01} = \mu_1$, $\mu_{02} = \mu_2$, $\mu_{12} = 0$ and $\omega_{01} = -\omega_{10} = \omega_1$, $\omega_{02} = -\omega_{20} = \omega_2$. After those simplifications and assuming RWA, Eq. (A4.1.10) becomes:

$$\dot{c}_0 = \frac{i}{2}\varepsilon_0 f(t)\left(c_1\mu_1 e^{i\delta\omega_1 t} + c_2\mu_2 e^{i\delta\omega_2 t}\right), \qquad (A4.1.28a)$$

$$\dot{c}_1 = \frac{i}{2}\varepsilon_0 f(t)c_0\mu_1 e^{-i\delta\omega_1 t}, \qquad (A4.1.28b)$$

$$\dot{c}_2 = \frac{i}{2}\varepsilon_0 f(t)c_0\mu_2 e^{-i\delta\omega_2 t}. \qquad (A4.1.28c)$$

To solve system (A4.1.28) we need to make an assumption that computational states are approximately degenerate $E_1 \approx E_2$ and therefore $\delta\omega_1 \approx \delta\omega_2 = \delta\omega$:

$$\dot{c}_0 = \frac{i}{2}\varepsilon_0 f(t)(c_1\mu_1 + c_2\mu_2)e^{i\delta\omega t}, \qquad (A4.1.29a)$$

$$\dot{c}_1 = \frac{i}{2}\varepsilon_0 f(t)c_0\mu_1 e^{-i\delta\omega t}, \qquad (A4.1.29b)$$

$$\dot{c}_2 = \frac{i}{2}\varepsilon_0 f(t)c_0\mu_2 e^{-i\delta\omega t}. \qquad (A4.1.29c)$$

Now we can solve Eq. (A4.1.29) the same way as the system (A4.1.12) for two-state case:

$$\ddot{c}_0 = \frac{i}{2}\varepsilon_0(\dot{f} + i\delta\omega f)(c_1\mu_1 + c_2\mu_2)e^{i\delta\omega t} + \frac{i}{2}\varepsilon_0 f(\dot{c}_1\mu_1 + \dot{c}_2\mu_2)e^{i\delta\omega t}. \quad (A4.1.30)$$

$$\ddot{c}_0 = \left(\frac{\dot{f}}{f} + i\delta\omega\right)\dot{c}_0 - \left(\frac{\varepsilon_0 f}{2}\right)^2 (\mu_1{}^2 + \mu_2{}^2)c_0. \qquad (A4.1.31)$$

Making the variable transformation:

$$z(t) = \frac{1}{2}\varepsilon_0\mu \int\limits_{-\infty}^{t} f(t')dt', \qquad (A4.1.32)$$

where $\mu = \sqrt{\mu_1^2 + \mu_2^2}$ is the effective transition moment for two states of one qubit. Analogous to Eq. (A4.1.17) we obtain:

$$(c_0'' + c_0)\frac{1}{2}\varepsilon_0\mu f - i\delta\omega c_0' = 0. \qquad (A4.1.33)$$

In the case of resonance $\delta\omega = 0$ we can rewrite Eq. (A4.1.33) as

$$c_0'' + c_0 = 0. \qquad (A4.1.34)$$

Clearly, this is an approximation. The pulse can't be in resonance with both transitions, but we neglect this difference.

Including initial condition $c_0(-\infty) = 0$ the solution of Eq. (A4.1.34) is again

$$c_0(t) = \alpha \sin[z(t)]. \qquad (A4.1.35)$$

The constant α depends on initial populations of both computing states, 1 and 2. From Eq. (A4.1.29a) and Eq. (A4.1.35):

$$\dot{c}_0 = \alpha\dot{z}\cos[z(t)] = \frac{i}{2}\varepsilon_0 f(t)(c_1\mu_1 + c_2\mu_2). \qquad (A4.1.36)$$

Using $\dot{z} = \frac{1}{2}\varepsilon_0\mu f$ Eq. (A4.1.36) becomes

$$\alpha\frac{1}{2}\varepsilon_0\mu f \cos[z(t)] = \frac{i}{2}\varepsilon_0 f(c_1\mu_1 + c_2\mu_2). \qquad (A4.1.38)$$

$$c_1 \mu_1 + c_2 \mu_2 = \frac{\alpha}{i} \mu \cos[z(t)]. \tag{A4.1.39}$$

$$c_1(-\infty)\mu_1 + c_2(-\infty)\mu_2 = \frac{\alpha}{i}\mu = \frac{\alpha}{i}\sqrt{(\mu_1{}^2 + \mu_2{}^2)}. \tag{A4.1.40}$$

From Eq. (A4.1.39) we can find parameter α for any population distribution between states 1 and 2. For example, for four typical states of the qubit:

$$c_1(-\infty) = 1, c_2(-\infty) = 0 \implies \alpha = i\frac{\mu_1}{\mu} \implies P = \frac{\mu_1{}^2}{\mu^2}\sin^2\left[\frac{1}{2}\varepsilon_\omega\mu\right], \tag{A4.1.40}$$

$$c_1(-\infty) = 0, c_2(-\infty) = 1 \implies \alpha = i\frac{\mu_2}{\mu} \implies P = \frac{\mu_2{}^2}{\mu^2}\sin^2\left[\frac{1}{2}\varepsilon_\omega\mu\right],$$

$$c_1(-\infty) = \frac{1}{\sqrt{2}}, \quad c_2(-\infty) = \frac{1}{\sqrt{2}} \implies \alpha = i\frac{(\mu_1 + \mu_2)}{\sqrt{2}\mu} \implies P = \frac{(\mu_1 + \mu_2)^2}{2\mu^2}\sin^2\left[\frac{1}{2}\varepsilon_\omega\mu\right],$$

$$c_1(-\infty) = \frac{1}{\sqrt{2}}, \quad c_2(-\infty) = -\frac{1}{\sqrt{2}} \implies \alpha = i\frac{(\mu_1 - \mu_2)}{\sqrt{2}\mu} \implies P = \frac{(\mu_1 - \mu_2)^2}{2\mu^2}\sin^2\left[\frac{1}{2}\varepsilon_\omega\mu\right].$$

All four expressions for Rabi oscillations in Eq. (A4.1.40) have different amplitude if $\mu_1 \neq \mu_2$. Therefore, even with a single readout pulse it may be feasible to get information about a population distribution and a relative phase between the computational states. For example, consider the readout from the states $|10\rangle$ and $|11\rangle$ (see Table 4.1). Those computational states have the largest difference in transition dipole moment in our model. We can choose the amplitude of the readout pulse ε_ω such as $\sin^2\left[\frac{1}{2}\varepsilon_\omega\mu\right] = 1$. In this case the population of the readout state for population distributions showed in Eq. (A4.1.40) would be respectively 0.554, 0.446, 0.997 and 0.003. The difference between those populations is significant, which means that we

could distinguish four important cases of population distribution of the computational states by intensity of fluorescence from the readout state. This method could be used to perform readout in simple cases when computational states have a limited number of distinguishable population distributions and transition dipole moments in the system are different.

Recall that we found the solution for the population of the readout state under the assumption that energies of computational states are equal. Numerical calculations of population of the readout state in the case of *equal* energies of computational states are expected to be in agreement with theoretical prediction of such model. Our tests confirm this.

However, the case of degenerate computational states is somewhat artificial since our physical system consists of two states with different energies. Energy splitting depends on which pair of computational states is chosen and varies in the range $\Delta E = 17 - 84 \, cm^{-1}$ (see Table 4.1). The question arises how well the formula (A4.1.40) will work in the case of non-degenerate qubit states, $\Delta E \neq 0$. Although we don't have analytic solution for this case, we can run numeric tests to see what effect the energy splitting has on population transfer.

Calculations were performed for the case of readout from computational states $|00\rangle$ and $|01\rangle$ with initial conditions $c_1(-\infty) = \frac{1}{\sqrt{2}}$, $c_2(-\infty) = \frac{1}{\sqrt{2}}$. The energy splitting between the computational states was $33.7 \, cm^{-1}$ (see Table 4.1). The center frequency of the readout pulse was set in the middle of two transition frequencies because for such a pulse the field intensities on both transition frequencies are equal. We varied both the

pulse amplitude ε_ω and the pulse width in the frequency domain σ to observe effect of pulse parameters on population transfer. Results of these calculations for non-degenerate states (Figure A4.1A) can be compared to the analytical model (Eq. (A4.1.40)) for degenerate Astates (Figure A4.1B). Overall they show similar periodic dependence on pulse amplitude ε_ω, but numeric results for non-degenerate case also show some dependence on pulse width σ (absent in the analytic model, compare Figs. A4.1A and A4.1B). Namely, at the first maximum of Rabi oscillations ($\varepsilon_\omega = 32.3 \, a.u.$) analytical model describes numerical results well for large pulse widths only, $\sigma > 70 \, cm^{-1}$. For narrower pulses numerical calculations show smaller population transfer and for pulse widths $\sigma < 20 \, cm^{-1}$ the calculations show no population transfer at all, while analytic model predicts the same constant value. At the second maximum of Rabi oscillations
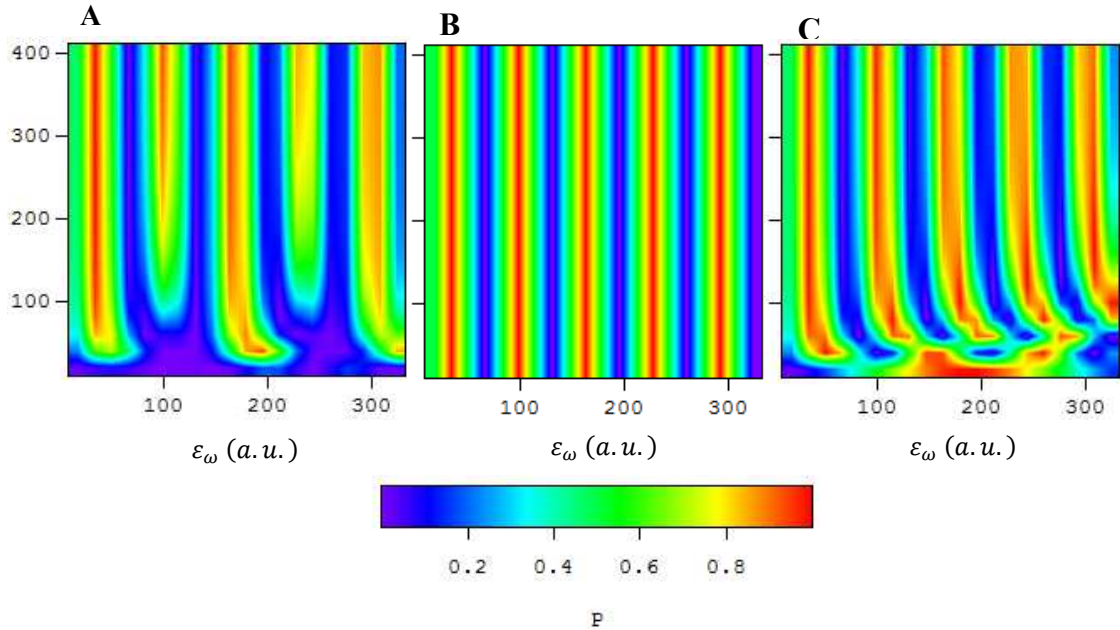
Figure A4.1: Population of the readout state in the one-qubit system as function of pulse amplitude ε_ω and pulse width σ. Plot A includes results of non-degenerate numerical calculations with energy splitting between computational states $\Delta E = 33.7 \, cm^{-1}$, plot B shows analytical dependence using a model of degenerate computational states (A4.1.40) and plot C shows semi-empirical dependence (A4.1.42).

$(\varepsilon_\omega = 96.8\ a.u.)$ good agreement is observed only for pulse width $\sigma > 300\ cm^{-1}$, while the population transfer diminishes for $\sigma < 70\ cm^{-1}$. And so on.

These results clearly indicate that the pulse width σ can be neglected only in the case of very broad pulses or very small splittings. When the pulse width σ is comparable to the energy splitting $\Delta E \neq 0$ the equation (A4.1.40) may lead to significant errors.

One may expect that dependence of population transfer P on pulse width σ comes from the fact that in the case of non-degenerate states the field intensities at transition frequencies, ε_1 and ε_2, are somewhat smaller than the field intensity at the central frequency ε_ω. One can express ε_1 and ε_2 through the pulse amplitude ε_ω and pulse width σ as follows (for a Gaussian pulse):

$$\varepsilon_1 = f(\varepsilon_\omega, \sigma) = \varepsilon_\omega \exp\left(-\frac{\left(\omega_1 - \frac{\omega_2 + \omega_1}{2}\right)^2}{2\sigma^2}\right), \qquad (A4.1.41a)$$

$$\varepsilon_2 = f(\varepsilon_\omega, \sigma) = \varepsilon_\omega \exp\left(-\frac{\left(\omega_2 - \frac{\omega_2 + \omega_1}{2}\right)^2}{2\sigma^2}\right). \qquad (A4.1.41b)$$

For ε_ω chosen in the middle between ω_1 and ω_2 we, obviously, obtain $\varepsilon_1 = \varepsilon_2$. Then, one can try to take this effect into account in an *ad hoc* fashion by introducing these reduced field intensities into Eq. (A4.1.40). For example:

$$P(\varepsilon_\omega, \sigma) = \frac{(\mu_1 + \mu_2)^2}{2\mu^2} \sin^2\left[\frac{1}{2}\varepsilon_1\mu\right]. \qquad (A4.1.42)$$

This semi-empirical model includes dependence of population transfer on the width σ for an off-resonant pulse. Figure A4.1C shows how this model compares to numerical calculations (Fig. A4.1A) and to the original expression (Eq. (A4.1.40)) having no dependence on σ (Fig. A4.1B). We see that Eq. (A4.1.42) gives some improvement over Eq. (A4.1.40), particularly in the range of narrow pulses, where the peak values of transfer probability P are shifted towards higher values of pulse amplitude ε_ω. This feature is evident in both Fig. A4.1A and A4.1C, but Fig. A4.1B lacks it. Still, some features Fig. A4.1A are missing in Fig. A4.1C.

We conclude that including dependence of P on pulse width σ in the case of non-degenerate qubit states may be important, particularly for narrower pulses and larger energy splittings. Overall, the semi-empirical expression (A4.1.42) describes the numerical results better, compared to the analytical expression (A4.1.40) obtained for degenerate states. Still, even Eq. (A4.1.42) is approximate and derivation of a rigorous expression for an off-resonant pulse and non-degenerate states would be beneficial.

Analytical expression for quantum beats

Our goal here is to derive expression for quantum beats signal obtained by excitation of superposition of two states with initial amplitudes $A_{1,2}$, phases $\varphi_{1,2}$ and energies $E_{1,2}$. We found that time delay τ can be introduced into our formalism by adding the phase term to the initial conditions:

$$c_1(-\infty) = A_1 e^{-i(E_1\tau + \varphi_1)}, \qquad c_2(-\infty) = A_2 e^{-i(E_2\tau + \varphi_2)}, \qquad \text{(A4.1.43)}$$

where $A_{1,2}$ arbitrary initial amplitudes that satisfy $A_1{}^2 + A_2{}^2 = 1$. Note that here we don't have to assume that the computational states are degenerate and $E_1 = E_2$. Here $E_1 \neq E_2$ analytically.

Substituting Eq. (A4.1.43) into Eq. (A4.1.39) we can obtain:

$$\alpha = \frac{i}{\sqrt{(\mu_1{}^2 + \mu_2{}^2)}} \left(\mu_1 A_1 e^{-iE_1\tau + \varphi_1} + \mu_2 A_2 e^{-iE_2\tau + \varphi_2} \right). \tag{A4.1.44}$$

Therefore Eq. (A4.1.35) becomes

$$c_0 = \frac{i}{\mu} \left(\mu_1 A_1 e^{-iE_1\tau + \varphi_1} + \mu_2 A_2 e^{-iE_2\tau + \varphi_2} \right) \sin[z]. \tag{A4.1.45}$$

Using trigonometrical notation of complex number we can rewrite Eq. (A4.1.45) as

$$c_0 = \frac{i}{\mu} \big(\mu_1 A_1 (\cos(E_1\tau - \varphi_1) + \sin(E_1\tau - \varphi_1))$$

$$+ \mu_2 A_2 (\cos(E_2\tau - \varphi_2) + \sin(E_2\tau - \varphi_2)) \big) \sin[z]. \tag{A4.1.46}$$

The probability that the system is in the state 0 after the interaction with a laser pulse is given by

$$P_0 = |c_0|^2 = \frac{\sin^2[z]}{\mu^2} \left(\mu_1{}^2 A_1{}^2 + \mu_2{}^2 A_2{}^2 + 2\mu_1 A_1 \mu_2 A_2 \cos(\Delta E\tau - \Delta\varphi) \right), \tag{A4.1.47}$$

where $\Delta E = E_1 - E_2$, $\Delta\varphi = \varphi_1 - \varphi_2$, and $z = \frac{1}{2}\varepsilon_\omega \mu$.

We would like to emphasize that expression (A4.1.47) was obtained in two steps. First we derived the expression for Rabi oscillations (A4.1.40) under the assumption of the degenerate computational states ($\Delta E = 0$). Then we introduced initial conditions

(A4.1.43), where we used the non-degenerate computational states $E_1 \neq E_2$ ($\Delta E \neq 0$). This is essential for quantum beats, because the readout from the degenerate states would not produce any beats since $\cos(\Delta E \tau - \Delta \varphi) = const$ for $\Delta E = 0$.

Expression (A4.1.47) is an analytical description of quantum beats oscillations of the population of the readout state. An example of quantum beats is shown in Figure A4.2 for the case $c_1(0) = c_2(0) = \frac{1}{\sqrt{2}}$ and pulse parameters $\sigma = 300 \, cm^{-1}$, $\varepsilon_\omega = 32.26 \, a.u.$ Both numerical and analytical results are presented. We can see that theoretical prediction describes numerical result fairly well, although the agreement is not perfect due to the approximation we made neglecting energy splitting between the computational states (small differences will be discussed below).
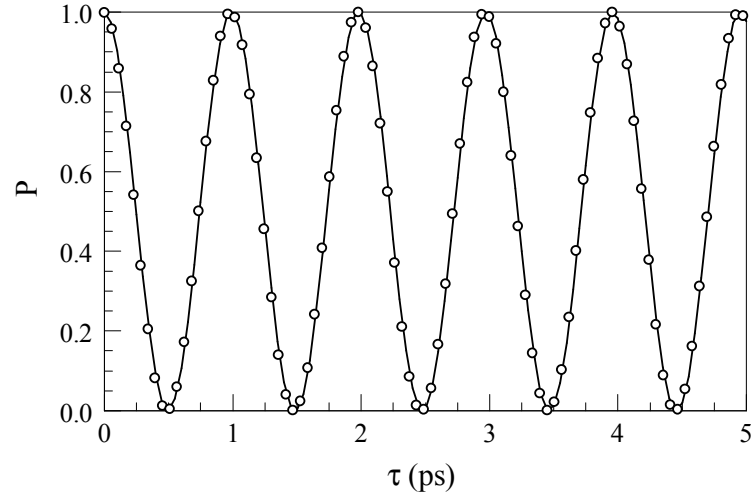
Figure A4.2: Quantum beats in the readout of the superposition of states $|00\rangle$ and $|01\rangle$ with equal populations. Analytical result is shown with a solid line and numerical result is shown with circles.

We can compare Eq. (A4.1.47) to the expression for quantum beats known from literature:

$$I(\tau) \sim \varepsilon_1{}^2\mu_1{}^2A_1{}^2 + \varepsilon_2{}^2\mu_2{}^2A_2{}^2 + 2\varepsilon_1\mu_1A_1\varepsilon_2\mu_2A_2\cos(\Delta E\tau - \Delta\varphi). \qquad \text{(A4.1.48)}$$

where $\varepsilon_{1,2}$ are laser pulse intensities at transitions from two computational states to the readout state. We can bring Eq. (A4.1.47) to a form similar to Eq. (A4.1.48) by expanding $\sin^2[z(t)]$ in Taylor series:

$$\sin^2[z] = \sin^2\left[\frac{1}{2}\varepsilon_\omega\mu\right] \approx \left(\frac{1}{2}\varepsilon_\omega\mu\right)^2. \qquad \text{(A4.1.49)}$$

Substituting Eq. (A4.1.49) into Eq. (A4.1.47) we obtain:

$$P_0 = \frac{1}{4}\left(\varepsilon_\omega{}^2\mu_1{}^2A_1{}^2 + \varepsilon_\omega{}^2\mu_2{}^2A_2{}^2 + 2\varepsilon_\omega{}^2\mu_1A_1\mu_2A_2\cos(\Delta E\tau - \Delta\varphi)\right). \qquad \text{(A4.1.50)}$$

The general form of the expression is similar to Eq. (A4.1.48), but we can see that Eq. (A4.1.50) includes the peak pulse amplitude ε_ω, while Eq. (A4.1.48) includes intensities on the transition frequencies $\varepsilon_{1,2}$.

Quantum beats from frequency shifted non-resonant readout pulse

Analytical model (A4.1.47) for quantum beats oscillations includes the peak amplitude of the readout pulse ε_ω unlike the expression (A4.1.48), that contains pulse amplitudes on each transition frequency ε_1 and ε_2. Expression (A4.1.47) describes computational results well when $\varepsilon_{1,2} \approx \varepsilon_\omega$, Therefore Eq. (A4.1.47) provides good description of quantum beats oscillations when readout pulse is centered between the transition frequencies and the pulse width is large compared to ΔE.

We discovered that expression (A4.1.47) does not describe computational results well when the center frequency of the readout pulse is shifted away from the average of the transition frequencies. This disagreement is illustrated in Figure A4.3 for energy splitting $\Delta E = 33.7 \; cm^{-1}$ and the readout pulse with width $\sigma = 200 \; cm^{-1}$ and center frequency shifted by $67 \; cm^{-1}$, so the central frequency of the pulse is higher than both transition frequencies. In this case the values of pulse intensities at the transition frequencies $\varepsilon_{1,2}$ are smaller than ε_0, therefore amplitude of quantum beats oscillations decreases as well. Expression (A4.1.47) does not describe this effect.
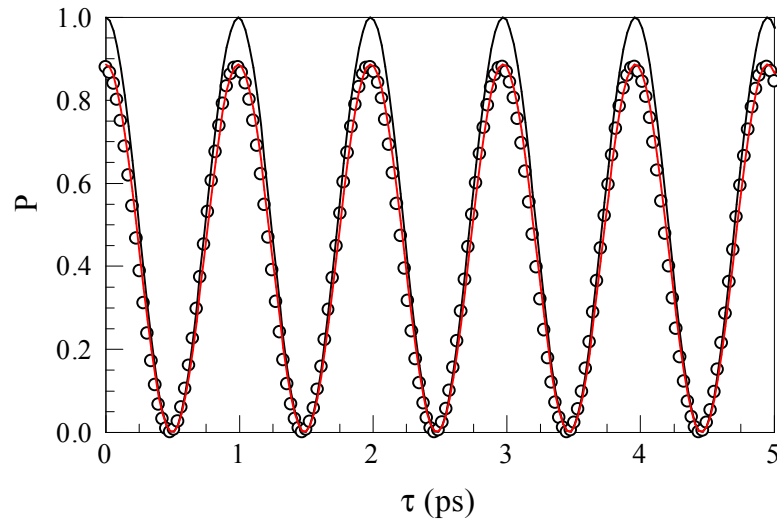
Figure A4.4: Oscillation of the population of the readout state as a function of time delay. Center frequency of the readout pulse is shifted by 67 cm⁻¹. Computational results is shown in circles, analytical model (A4.1.45) is shown by black line, analytical model (A4.1.51) is shown by red line.

We found that it is possible to modify Eq. (A4.1.47) empirically in order to obtain better agreement with computational results for frequency shifted pulses. If we introduce ε_1 and ε_2 in Eq. (A4.1.47) and divide it by ε_ω for normalization we will obtain:

$$P(\tau) = \frac{\sin^2\left[\frac{1}{2}\varepsilon_\omega\mu\right]}{\varepsilon_\omega{}^2\mu^2}\left(\varepsilon_1{}^2\mu_1{}^2A_1{}^2 + \varepsilon_2{}^2\mu_2{}^2A_2{}^2\right.$$

$$\left. +2\varepsilon_1\mu_1A_1\varepsilon_2\mu_2A_2\cos(\Delta E\tau - \Delta\varphi)\right). \qquad (A4.1.51)$$

We found that this model (A4.1.51) gives better agreement with computational results in case of frequency shifted readout pulse (Figure A4.4). We don't have a rigorous derivation of Eq. (A4.1.51) but we can use this semi-empirical expression for analyzing quantum beats signals.

References for Chapter 4

1. J. P. Palao, and R. Kosloff. Phys. Rev. Lett. **89**, 188301 (2003).

2. J. P. Palao, and R. Kosloff, Phys. Rev. A **68**, 062308 (2003).

3. C. M. Tesch, L. Kurtz, and R. de Vivie-Riedle, Chem. Phys. Lett. **343**, 633 (2001).

4. C. M. Tesch, and R. de Vivie-Riedle, Phys. Rev. Lett. **89**, 157901 (2002).

5. U. Troppmann, C. M. Tesch, and R. de Vivie-Riedle, Chem. Phys. Lett. **378**, 273 (2003).

6. C. M. Tesch, and R. de Vivie-Riedle, J. Chem. Phys. **121**, 12158 (2004).

7. B. Korff, U. Troppmann, K. Kompa, and R. de Vivie-Riedle, J. Chem. Phys. **123**, 244509 (2005).

8. U. Troppmann and R. de Vivie-Riedle, J. Chem. Phys. **122**, 154105 (2005).

9. U. Troppmann, C. Gollub, and R. de Vivie-Riedle, New J. Phys. **8**, 100 (2006).

10. Z. Amitay, R. Kosloff, and S.R. Leone, Chem. Phys. Lett. **359**, 8 (2002).

11. D. Babikov, J. Chem. Phys. **121**, 7577 (2004).

12. J. Vala, Z. Amitay, B. Zhang, S.R. Leone, and R. Kosloff, Phys. Rev. A **66**, 062316 (2002).

13. Y. Ohtsuki, Chem. Phys. Lett. **404**, 126 (2005).

14. Y. Ohtsuki, New J. Phys. **12**, 045002 (2005).

15. Y. Teranishi, Y. Ohtsuki, K. Hosaka, H. Chiba, H. Katsuki, and K. Ohmori, J. Chem. Phys. **124**, 114110 (2006).

16. S. Suzuki, K. Mishima, and K. Yamashita, Chem. Phys. Lett. **410**, 358 (2005).

17. K. Shioya, K. Mishima, and K. Yamashita, Molecular Physics **105**, 1283 (2007).

18. K. Mishima, and K. Yamashita, Chem. Phys. **361**, 106 (2009).

19. K. Mishima, and K. Yamashita, J. Chem. Phys. **130**, 034108 (2009).

20. K. Mishima, and K. Yamashita, Chem. Phys. **367**, 63 (2010).

21. K. Mishima, and K. Yamashita, Chem. Phys. **379**, 13 (2011).

22. Q. Wei, S. Kais, and Y. P. Chen, J. Chem. Phys. **132**, 121104 (2010).

23. Q. Wei, S. Kais, B. Friedrich, and D. Herschbach, J. Chem. Phys. **134**, 121107 (2011).

24. Q. Wei, S. Kais, B. Friedrich, and D. Herschbach, J. Chem. Phys. **135**, 154102 (2011).

25. J. Zhu, S. Kais, Q. Wei, D. Herschbach, and B. Friedrich, J. Chem. Phys. **138**, 024104 (2013).

26. D. Weidinger, and M. Gruebele, Chem. Phys. **350**, 139 (2008).

27. T. Cheng, and A. Brown, J. Chem. Phys. **124**, 34111 (2006).

28. T. Cheng, and A. Brown, J. Chem. Phys. **124**, 034111 (2006).

29. M. Schröder, and A. Brown, J. Chem. Phys. **131**, 034101 (2009).

30. R. R. Zaari, and A. Brown, J. Chem. Phys. **132**, 014307 (2010).

31. R. R. Zaari, and A. Brown, J. Chem. Phys. **135**, 044317 (2011).

32. R. R. Zaari, and A. Brown, J. Chem. Phys. **137**, 104306 (2012).

33. M. Ndong, D. Lauvergnat, X. Chapuisat, and M. Desouter-Lecomte, J. Chem. Phys. **126**, 244505 (2007).

34. L. Bomble, D. Lauvergnat, F. Remacle, and M. Desouter-Lecomte, J. Chem. Phys. **128**, 064110 (2008).

35. P. Pellegrini, S. Vranckx, and M. Desouter-Lecomte, Phys. Chem. Chem. Phys. **13**, 18864 (2011).

36. P. Pellegrini, and M. Desouter-Lecomte, Eur. Phys. J. D **64**, 163 (2011).

37. A. Jaouadi, E. Barrez, Y. Justum, abd M. Desouter-Lecomte, J. Chem. Phys. **139**, 014310 (2013).

38. M. Tsubouchi, and T. Momose, Phys. Rev. A **77**, 052326 (2008).

39. C. Menzel-Jones, and M. Shapiro, Phys. Rev. A **75**, 052308 (2007).

40. M. Zhao, and D. Babikov, J. Chem. Phys. **126**, 204102 (2007).

41. Y. Y. Gu, and D. Babikov, J. Chem. Phys. **131**, 034306 (2009).

42. D. Weidinger, and M. Gruebele, Mol. Phys. **105**, 1999 (2007).

43. E. Berrios, M. Gruebele, D. Shyshlov, L. Wang, and D. Babikov, J. Phys. Chem. A, **116**, 46 (2012).

44. D. Shyshlov, and D. Babikov, J. Chem. Phys. **137**, 194318 (2012).

45. E. Berrios, and M. Gruebele, J. Phys. Chem. A, **117**, 7535 (2013).

46. E. Berrios, S. Pratt, P. Tripathi, and M. Gruebele, J. Phys. Chem. A, **117**, 12082 (2013).

47. M. Gruebele, and A. H. Zewail, J. Chem. Phys. **98**, 2 (1993).

48. E. Hack, and J. R. Huber, Int. Rev. Phys. Chem., **10**, 287 (1991).

49. M. Hayashi at al., Tamkang J. Sci. Eng., **3**, 145 (2000).

50. H. Goto, H. Katsuki, H. Ibrahim, H. Chiba, and K. Ohmori, Nature Physics, **7**, 383 (2011).

Chapter 5: Computational study of cold ions trapped in a double-well potential

5.1 Introduction

In a typical ion-cooling and trapping experiment [1-5] a string of multiple ions is confined along the axis of the trap. Each ion interacts strongly with its neighbor ions, and with potential of the trap, which leads to collective vibrational motion of the quasi-linear ion-string. The typical ion-ion distance in such architecture is on order of a few micron, and the trapping potential is perfectly parabolic (harmonic) at this length-scale. Several ions, up to 9 per trap [6-7], can be trapped, cooled and entangled, to create a quantum information register/processor [2,4,8-14]. Further scaling can be achieved by bringing together several traps and shuttling individual ions between the traps [15-18].

In recent years new opportunity was explored, both experimentally [19,20] and computationally [21,22], where a strongly-unharmonic double-well trapping potential is created along the axis of the trap:

$$V(z) = \beta z^4 - \alpha z^2. \qquad (5.1.1)$$

In experiments the goal was to keep ions in two separate wells, at a significant distance, in order to reduce their Coulomb interaction and create two almost independent weakly-coupled quantum oscillators. This is qualitatively illustrated by Fig. 5.1A for the case of
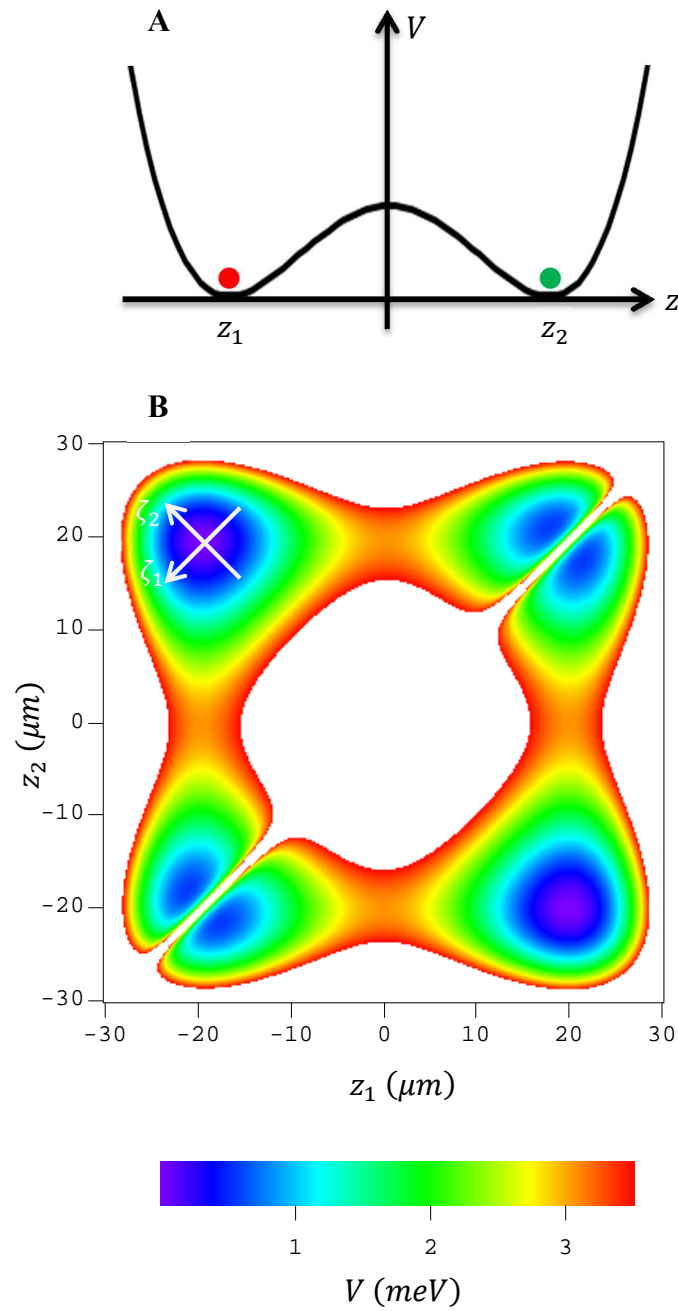
Figure 5.1: A) Qualitative illustration of the double-well potential with two ions trapped in the separated wells; B) Two-dimensional PES of the system in the Be$^+$ experiment. Two white axis inserted in the top left corner indicate the normal mode coordinates.

Table 5.1: Parameters of the double-well potential and comparison of the system properties in our model with those in the experiments of Ref. [19] and [20].

		Be+ experiment		Ca+ experiment	
		Measured[19]	Model	Measured[20]	Model
$\alpha \cdot 10^3$, meV/ μm^2		—	15.525	—	1.167
$\beta \cdot 10^7$, meV/ μm^4		—	205.3	—	8.525
Ion-ion distance d, μm		40	38.920	54	52.546
Potential barrier V_0, meV		3	2.935	0.5	0.399
Normal mode frequency	$\omega_1/2\pi$	4111.8	4111.375	540	536.928
	$\omega_2/2\pi$	4114.9	4114.600	543	539.177
Mode splitting $\delta\omega/2\pi$, kHz		3.226	3.22515	2.25	2.249
Energy swap time τ_{swp}, μs		155	155.11	222	222.25

two trapped ions, one in each well of the double-well trap. In this architecture the ion-ion distance can exceed 50 micron. The group at NIST used Be+ ions [19], while the Innsbruck group used Ca+ ions [20]. Other properties of their traps are listed in Table 5.1. Note that in each case the potential barrier between the wells is very high. Simple estimates indicate that each well is capable of maintaining on the order of $\sim 10^5$ quanta of vibrational excitation. One could expect that, if the vibrational excitation is low (say within 10 quanta), the dynamics of the ion motion in two wells should be entirely independent. However, both NIST and Innsbruck groups observed very efficient coherent transfer of vibrational energy from one well to another, despite the seemingly weak coupling [19,20].

The goal of this chapter is to understand this interesting result by modelling quantum dynamics of the system of two ions in the double-well potential as accurately as possible, without making any assumptions concerning the coupling strength or the energy spectrum of the double-well system. Such rigorous theoretical tools are often used by computational chemists [21,22]. First, we consider an accurate potential energy surface of the system, without Taylor series expansion of the Coulomb interaction, and without truncation of any higher order terms. Then we numerically search for the minimum energy point on the surface and perform the normal mode analysis. Harmonic approximation is avoided, and the normal mode frequencies are used only to set up an efficient basis set for accurate representation of the wave function. The Hamiltonian matrix is computed and numerically diagonalized in order to determine accurate eigenstates of the system (energies and wave functions). Those are used to study time-evolution of the vibrational wave packets in time and space. The initial conditions are chosen to mimic the experiments conducted at NIST and Innsbruck [19,20].

5.2 Theory

5.2.1 Parameters of the model

The double-well trap potential is described by a combination of terms of the second and fourth orders, as in Eq. (5.1.1), where α and β are two parameters. One of the goals of our computational work is to reproduce experimental results by calculations, which requires an appropriate choice of α and β. Unfortunately, their values are not directly measurable in the experiment. So, we have to find the values of α and β that

reproduce other measurable characteristics of the experiment, such as equilibrium distance between the ions d, height of the potential barrier between the ions V_0 and, most importantly, the system frequencies ω_1 and ω_2. These can be described by the average frequency $\omega_{ave} = (\omega_1 + \omega_2)/2$ and the splitting $\delta\omega = \omega_2 - \omega_1$.

For this, we carried out calculations of d, V_0, ω_{ave} and $\delta\omega$ (as explained in the next section) using different values of α and β. We considered 20 values of α and 20 values of β, covering 400 combinations total, separately for the Be^+ and Ca^+ experiments. Then we analyzed the two-dimensional functions $d(\alpha,\beta)$, $V_0(\alpha,\beta)$, $\omega_{ave}(\alpha,\beta)$ and $\delta\omega(\alpha,\beta)$ using their contour plots and trying to identify the values of α and β that will reproduce all four experimental characteristics.

For example, in Figure 5.2A one contour line (green) is given for the $d(\alpha,\beta)$ dependence to represent the experimental value of $d = 40~\mu m$ in the Be^+ experiment. This line shows a significant slope, which indicates that the equilibrium ion-ion distance d is quite sensitive to both α and β, and that many combinations of α and β in a broad range of values can reproduce the experimental value of d.

In the same manner we plotted one contour line of the (α,β)-dependence for the experimental value of $V_0 = 3~meV$ (light blue), one contour line for $\omega_{ave} = 2\pi \times 4.113~MHz$ (dark blue) and one contour line for $\delta\omega = 2\pi \times 3.226~kHz$ (red) in the Be^+ experiment, all four lines together in Fig. 5.2A. From this picture we see that different pairs of curves intersect (six points total) which means that we can identify the values of α and β that will reproduce exactly any two experimental characteristics, but not all four

characteristics at the same time, simply because four curves in Fig. 5.2A do not intersect at the same point.
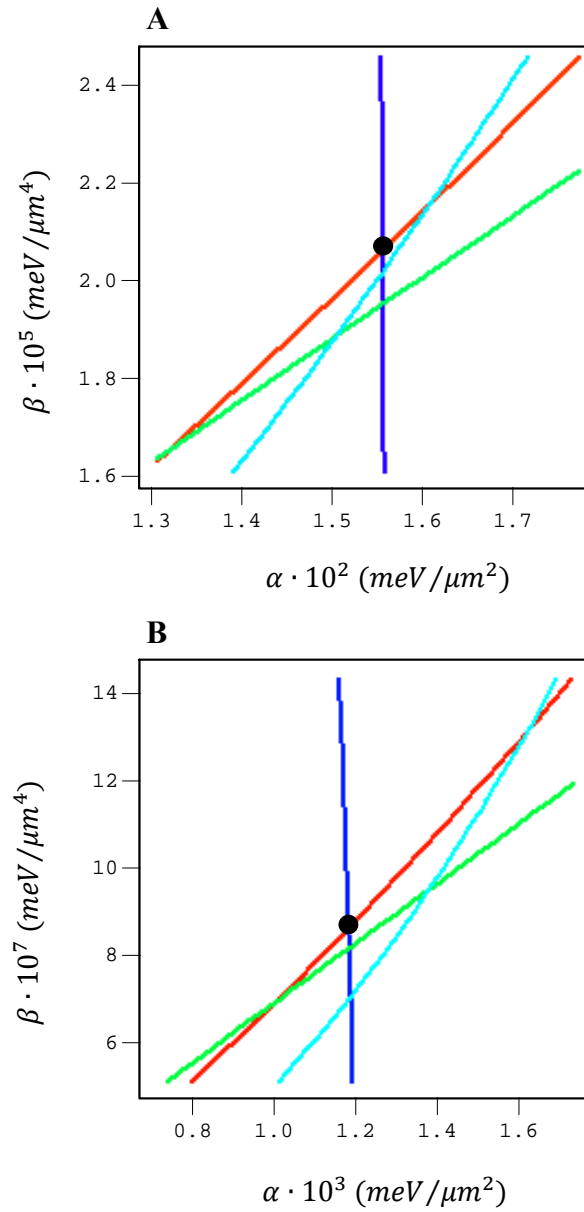
Figure 5.2: Dependence of system properties on parameters of the double-well potential in the cases of: A) Be^+ experiment; and B) Ca^+ experiment. In each case only one contour line is given that correspond to the experimental value of the distance between ions d (green), potential barrier V_0 (cyan), average vibration frequency ω_{ave} (blue), and frequency splitting $\delta\omega$ (red). Black dot indicates the values of potential parameters α and β that were chosen to represent the trap in our model.

However, we can see that in the range of values $\alpha = 1.52 - 1.58 \cdot 10^2\ meV/\mu m^2$ and $\beta = 1.93 - 2.05 \cdot 10^5\ meV/\mu m^4$ all four lines pass close together. Furthermore, different experimental characteristics have different importance and were reported with different accuracies [19]. Namely, the vibration frequencies are measured more accurately than geometric parameters of the trap d and V_0. So, we decided to choose the values of α and β to reproduce nearly exactly the experimental values of ω_{ave} and $\delta\omega$, while the values of d and V_0 are reproduced approximately. The corresponding point in the (α, β)-space is indicated by the black dot in Fig. 5.2A for the Be[+] experiment, and, similarly, in Fig. 5.2B for the Ca^{+} experiment. The values of α and β chosen for the model are listed in the Table 5.1. Deviations of the model values of d and V_0 from the experiment can also be estimated using Table 5.1. Thus, in the case of Be[+] experiment we have ~3% deviation of the distance d and ~2% deviation of the potential barrier V_0. In the case of Ca^{+} experiment we have ~3% deviation of d and ~20% deviation of V_0. Larger deviation of the potential barrier V_0 in the case of Ca^{+} can be explained by the fact that the experimental value was not really reported in the paper by the Innsbruck group [20]. We derived it approximately from the schematic plot in that paper. So, one can say, that all parameters of our models are within experimental ranges of accuracy.

5.2.2 Hamiltonian of the system

When the trap parameters have been chosen, the potential energy of two ions in the double-well potential can be expressed as follows (in atomic units):

$$V(z_1, z_2) = \beta z_1^4 - \alpha z_1^2 + \beta z_2^4 - \alpha z_2^2 + \frac{1}{|z_2 - z_1|}, \qquad (5.2.1)$$

where z_1 and z_2 are Cartesian coordinates of the ions along the axis of the trap. Equation 5.2.1 represents a two-dimensional potential energy surface (PES) of the system, $V(z_1, z_2)$. The PES for the Be^+ experiment is visualized in Fig. 5.1B using a color map. It is symmetric with respect to the line $z_1 = z_2$ where the energy is infinite, due to Coulomb repulsion of two ions sitting in the same position. Overall, there are six potential energy wells on the PES. Two global minima correspond to the case of two ions sitting in two different wells, one ion per well. Two possibilities, $z_1 < z_2$ and $z_1 > z_2$, arise from permutation of two ions. Four local minima correspond to the ions sitting in the same well. Four possibilities arise from permutation and the presence of two wells. The PES for the Ca^+ experiment exhibits similar features.

We focus on the global minimum in the top left corner of Figure 5.1B to perform the normal mode analysis. It corresponds to $z_1 < z_2$ (first ion on the left, second ion on the right). First we need to find the equilibrium coordinates of the ions z_{e1} and z_{e2} that correspond to this global minimum, but they can't be determined analytically. For numerical minimization we employed the Newton-Raphson method [23]. The results are $(z_{e1}, z_{e2}) = (-19.46 \, \mu m, \ 19.46 \, \mu m)$ for the Be^+ experiment and $(z_{e1}, z_{e2}) = (-26.27 \, \mu m, \ 26.27 \, \mu m)$ for the Ca^+ experiment. The values of potential energy at the minimum were $V^{eq} = -5.8331 \, meV$ for the Be^+ experiment and $V^{eq} = -0.7713 \, meV$ for the Ca^+ experiment.

At the stationary point we can perform the normal mode analysis. Both experiments considered here use the ions of identical masses (either two Be^+, or two Ca^+ ions). Therefore, the mass-weighted Hessian matrix can be written as:

$$F = \begin{vmatrix} m & 0 \\ 0 & m \end{vmatrix}^{-\frac{1}{2}} \begin{vmatrix} \dfrac{\partial^2 V}{\partial z_1{}^2} & \dfrac{\partial^2 V}{\partial z_1 \partial z_2} \\ \dfrac{\partial^2 V}{\partial z_1 \partial z_2} & \dfrac{\partial^2 V}{\partial z_2{}^2} \end{vmatrix} \begin{vmatrix} m & 0 \\ 0 & m \end{vmatrix}^{-\frac{1}{2}}. \tag{5.2.2}$$

From Eq. (5.2.1), and taking into account that $z_1 < 0$ and $z_2 > 0$, the elements of the matrix are computed analytically:

$$\frac{\partial^2 V}{\partial z_{1,2}{}^2} = -2\alpha + 12\beta z_{1,2}{}^2 + \frac{2}{(z_2 - z_1)^3}, \tag{5.2.3a}$$

$$\frac{\partial^2 V}{\partial z_1 \partial z_2} = -\frac{2}{(z_2 - z_1)^3}. \tag{5.2.3b}$$

Using Eq. (5.2.2-5.2.3) matrix F at the equilibrium point and (z_{e1}, z_{e2}) is obtained:

$$F = \frac{1}{m} \begin{vmatrix} -2\alpha + 12\beta z_{e1}{}^2 + \dfrac{2}{(z_{e2} - z_{e1})^3} & -\dfrac{2}{(z_{e2} - z_{e1})^3} \\ -\dfrac{2}{(z_{e2} - z_{e1})^3} & -2\alpha + 12\beta z_{e2}{}^2 + \dfrac{2}{(z_{e2} - z_{e1})^3} \end{vmatrix}. \tag{5.2.4}$$

Diagonalization of this matrix produces frequencies ω_1 and ω_2 of the normal modes (given in Table 5.1) and the corresponding eigenvectors:

$$A = \begin{vmatrix} -\dfrac{\sqrt{2}}{2} & -\dfrac{\sqrt{2}}{2} \\ -\dfrac{\sqrt{2}}{2} & \dfrac{\sqrt{2}}{2} \end{vmatrix}. \tag{5.2.5}$$

Table 5.2: Predicted energy spectra of two ions in the double-well experiments of Ref. [19-20].

Energy level	Normal mode	Be$^+$ experiment, kHz		Ca$^+$ experiment, kHz	
		Harmonic	Matrix	Harmonic	Matrix

	assignment (n_1, n_2)	approximation	diagonalization	approximation	diagonalization
1	(0,0)	4112.9875	4112.9860	538.05245	538.05227
2	(1,0)	8224.3623	8224.3564	1074.9800	1074.9793
3	(0,1)	8227.5875	8227.5816	1077.2298	1077.2290
4	(2,0)	12335.7372	12335.7247	1611.9076	1611.9061
5	(1,1)	12338.9624	12338.9476	1614.1573	1614.1556
6	(0,2)	12342.1875	12342.1750	1616.4071	1616.4056
7	(3,0)	16447.1121	16447.0907	2148.8352	2148.8326
8	(2,1)	16450.3372	16450.3114	2151.0849	2151.0818
9	(1,2)	16453.5624	16453.5366	2153.3346	2153.3316
10	(0,3)	16456.7876	16456.7662	2155.5844	2155.5818

The first column of matrix $\boldsymbol{A}$ corresponds to the center-of-mass motion mode, $\Delta z_1 = \Delta z_2$, while the second column corresponds to the symmetric stretching mode, $\Delta z_1 = -\Delta z_2$. Here we defined displacements of ions from their equilibrium positions:

$$\Delta z_1 = z_1 - z_{e1}, \qquad \Delta z_2 = z_2 - z_{e2}. \tag{5.2.6}$$

Based on the normal mode frequencies ω_1 and ω_2 we can predict an approximate energy spectrum of the system using a harmonic model. This is included in Table 5.2, for both experiments, with Be^+ and Ca^+ ions, respectively.

The Hamiltonian of the system is written initially in Cartesian coordinates as:

$$\widehat{H}(z_1, z_2) = -\frac{1}{2m}\frac{\partial^2}{\partial z_1{}^2} - \frac{1}{2m}\frac{\partial^2}{\partial z_2{}^2} + V(z_1, z_2) - V^{eq}, \tag{5.2.7}$$

where $V(z_1, z_2)$ is the potential energy from Eq. (5.2.1) and V^{eq} is the potential energy of equilibrium configuration. In order to study dynamics of the system near the equilibrium point it is convenient, instead of Cartesian coordinates (z_1, z_2), to employ the normal mode coordinates (ζ_1, ζ_2) defined as:

$$\begin{pmatrix} \zeta_1 \\ \zeta_2 \end{pmatrix} = A^T \begin{pmatrix} \Delta z_1 \\ \Delta z_2 \end{pmatrix}, \tag{5.2.8}$$

where A^T is transposed matrix A from Eq. (5.2.5). Coordinate ζ_1 describes the center-of-mass motion mode and coordinate ζ_2 describes the symmetric stretching mode as shown in Figure 1B. From Eqs. (5.2.6-5.2.8) the Hamiltonian operator in the normal mode coordinates can be derived:

$$\hat{H}(\zeta_1, \zeta_2) = -\frac{1}{2m}\frac{\partial^2}{\partial \zeta_1^2} - \frac{1}{2m}\frac{\partial^2}{\partial \zeta_2^2} + V(\zeta_1, \zeta_2) - V^{eq}, \tag{5.2.9}$$

$$V(\zeta_1, \zeta_2) = \beta \left(z_{e1} - \frac{\zeta_1 + \zeta_2}{\sqrt{2}} \right)^4 - \alpha \left(z_{e1} - \frac{\zeta_1 + \zeta_2}{\sqrt{2}} \right)^2 + \beta \left(z_{e2} + \frac{\zeta_2 - \zeta_1}{\sqrt{2}} \right)^4$$

$$-\alpha \left(z_{e2} + \frac{\zeta_2 - \zeta_1}{\sqrt{2}} \right)^2 + \frac{1}{\left| \sqrt{2}\zeta_2 + z_{e2} - z_{e1} \right|}. \tag{5.2.10}$$

Note that the Coulomb term in Eq. (5.2.10) depends on the symmetric stretching coordinate ζ_2 only, and does not depend on ζ_1, which is consistent with the property that the center-of-mass motion, described by ζ_1, does not change distance between the ions. By removing parentheses in Eq. (5.2.10) one can check that potential $V(\zeta_1, \zeta_2)$ contains coupling terms between the two vibration modes and therefore is non-separable.

5.2.3 Basis set expansion and matrix diagonalization

The direct product basis set expansion is used to represent wave functions of the system:

$$\psi^{\nu}(\zeta_1, \zeta_2) = \sum_{i,j}^{N} c_{ij}^{\nu} \varphi_i(\zeta_1) \varphi_j(\zeta_2), \qquad (5.2.11)$$

where $\varphi_i(\zeta_1)$ and $\varphi_j(\zeta_2)$ are one dimensional basis sets for the normal mode coordinates ζ_1 and ζ_2, N is the number of basis functions, index ν labels states of the two-ion system and has values in the range from 1 to N^2, c_{ij}^{ν} are coefficients of linear combination. For each coordinate we employ the basis set of eigenfunctions of harmonic oscillator with the corresponding normal mode frequency:

$$\varphi_j(\zeta_{1,2}) = A_j \cdot e^{-y_{1,2}^2} \cdot H_j(y_{1,2}), \qquad (5.2.12a)$$

$$A_j = \frac{1}{\sqrt{2^j j!}} \left(\frac{m\omega_{1,2}}{\pi}\right)^{1/4}. \qquad (5.2.12b)$$

Here $\omega_{1,2}$ are the frequencies of the normal modes, H_j are Hermite polynomials. The standard notations are used: $y_{1,2} = \gamma_{1,2}\zeta_{1,2}$, where $\gamma_{1,2} = \sqrt{m\omega_{1,2}}$. The number of basis functions included in our calculations is $N = 40$.

Elements of the Hamiltonian matrix should be calculated as:

$$H_{ij,kl} = \langle \varphi_i(\zeta_1)\varphi_j(\zeta_2)|\hat{H}|\varphi_k(\zeta_1)\varphi_l(\zeta_2)\rangle. \qquad (5.2.13)$$

The kinetic energy part of the Hamiltonian matrix can be derived from Eqs. (5.2.9) and (5.2.13):

$$T_{ij,kl} = -\frac{1}{2m}\left\langle \varphi_i(\zeta_1)\varphi_j(\zeta_2)\left|\frac{\partial^2}{\partial\zeta_1{}^2} + \frac{\partial^2}{\partial\zeta_2{}^2}\right|\varphi_k(\zeta_1)\varphi_l(\zeta_2)\right\rangle$$

$$= -\frac{1}{2m}\delta_{jl}\left\langle\varphi_i(\zeta_1)\left|\frac{\partial^2\varphi_k(\zeta_1)}{\partial\zeta_1{}^2}\right.\right\rangle - \frac{1}{2m}\delta_{ik}\left\langle\varphi_j(\zeta_2)\left|\frac{\partial^2\varphi_l(\zeta_2)}{\partial\zeta_2{}^2}\right.\right\rangle \qquad (5.2.14)$$

Second derivative of the basis functions can be calculated analytically from Eq. (5.2.12):

$$\frac{\partial^2\varphi_k(\zeta_1)}{\partial\zeta_1{}^2} = A_k\left(\frac{\partial^2 H_k(y_1)}{\partial\zeta_1{}^2}\cdot e^{-y_1^2/2} + 2\frac{\partial H_k(y_1)}{\partial\zeta_1}\cdot\frac{\partial}{\partial\zeta_1}\left(e^{-y_1^2/2}\right)\right.$$

$$\left. +H_k(y_1)\cdot\frac{\partial^2}{\partial\zeta_1{}^2}\left(e^{-y_1^2/2}\right)\right) \qquad (5.2.15)$$

Derivatives of Hermite polynomials can be calculated using the property:

$$H_k'(y_1) = 2kH_{k-1}(y_1). \qquad (5.2.16)$$

From Eq. (5.2.16) we can obtain:

$$H_k'(y_1) = \gamma_1 H_k'(\gamma_1\zeta_1) = \gamma_1\cdot 2kH_{k-1}(\gamma_1\zeta_1), \qquad (5.2.17)$$

$$H_k''(y_1) = \left(\gamma_1 H_k'(\gamma_1\zeta_1)\right)' = 2k\gamma_1\left(H_{k-1}(\gamma_1\zeta_1)\right)' =$$

$$= 4k(k-1)\gamma_1{}^2 H_{k-2}(\gamma_1\zeta_1). \qquad (5.2.18)$$

Substituting Eqs. (5.2.15, 5.2.17-18) into Eq. (5.2.14) we obtain the final expression for matrix elements of the kinetic energy operator:

$$T_{ij,kl} = -\frac{1}{2m}\delta_{jl}\left\langle\varphi_i(\zeta_1)\left|A_k\left(4k(k-1)\gamma_1{}^2 H_{k-2}(\gamma_1\zeta_1)\right)e^{-\gamma_1^2\zeta_1^2/2}\right.\right\rangle$$

$$-\frac{1}{2m}\delta_{ik}\langle\varphi_j(\zeta_2)|A_l\big(4l(l-1)\gamma_2{}^2H_{l-2}(\gamma_2\zeta_2)\big)e^{-\gamma_2^2\zeta_2^2/2}\rangle. \qquad (5.2.19)$$

Matrix elements of the potential energy operator are:

$$V_{ij,kl} = \langle\varphi_i(\zeta_1)\varphi_j(\zeta_2)|V(\zeta_1,\zeta_2)|\varphi_k(\zeta_1)\varphi_l(\zeta_2)\rangle. \qquad (5.2.20)$$

Integrals in Eqs. (5.2.19-5.2.20) are computed numerically using Gauss-Hermite quadrature method [23]. The potential energy $V(\zeta_1,\zeta_2)$ is, again, not separable, so, we have to compute double integrals in Eq. (21).

Diagonalization of the Hamiltonian matrix $\boldsymbol{H} = \boldsymbol{T} + \boldsymbol{V}$ produces energy spectrum of the system. We performed diagonalization numerically using subroutine DSYEV [24]. The resultant energy spectra for both Be^+ and Ca^+ experiments are presented in Table 5.2. We can see that for both systems the energies predicted by harmonic approximation are very close to the energies obtained accurately by diagonalizing the Hamiltonian matrix, with difference at seventh significant figure.

In order to quantify anharmonicities of the system we fitted the lower ten energy levels of the accurate spectrum with Dunham expansion:

$$E_{v_1 v_2} = D + \omega_1\left(v_1 + \frac{1}{2}\right) + \omega_2\left(v_2 + \frac{1}{2}\right) - \Delta_1\left(v_1 + \frac{1}{2}\right)^2 - \Delta_2\left(v_2 + \frac{1}{2}\right)^2$$

$$-\Delta_{12}\left(v_1 + \frac{1}{2}\right)\left(v_2 + \frac{1}{2}\right). \qquad (5.2.21)$$

Table 5.3: Coefficients of Dunham expansion (including intra- and inter-mode anharmonicities) obtained by fitting lower ten energy levels for the Be^+ and Ca^+ ions in the double-well traps.

	Be^+	Ca^+

	experiment	experiment
$\omega_1/2\pi$, kHz	4111.375	536.928
$\omega_2/2\pi$, kHz	4114.600	539.177
$\Delta_1/2\pi$, Hz	1.0993	0.1292
$\Delta_2/2\pi$, Hz	1.1082	0.1339
$\Delta_{12}/2\pi$, Hz	0.18632	0.02364
$D/2\pi$, Hz	4.4278	0.5346
$\delta\omega/2\pi$, kHz	3.22515	2.249

The values of six fitting coefficients are given in Table 5.3. One can see that anharmonicites of two normal modes, Δ_1 and Δ_2, are very similar and are tiny compared to the normal mode frequencies, $\Delta_{1,2}\sim10^{-6}\omega_{1,2}$. This result is consistent with the data of Table 5.2. It appears that the spectrum of the system is very harmonic, at least at the level of low vibrational excitation (say, 10 quanta), despite the fact that anharmonic Coulomb interaction is included exactly, without any truncation. The origin and consequences of this property are further discussed in Sec. 5.3. Here we would like to mention that we carried

out a very detailed convergence study to ensure that accuracy of our predictions of the frequency values ($\sim10^{-12}\omega$) is well below the magnitude of anharmonicities.

5.2.4 Time-evolution of the system

Numerically accurate wave functions of the system $\psi^\nu(\zeta_1, \zeta_2)$ and the values of energies E_ν can be used to model time-evolution of vibrational wave packets. The time-dependent wave function of the system can be expressed as:

$$\psi^t(\zeta_1, \zeta_2) = \sum_\nu b^\nu \psi^\nu(\zeta_1, \zeta_2) e^{-iE_\nu t}, \qquad (5.2.22)$$

where b^ν are probability amplitudes determined by projecting the initial wave packet $\psi^{in}(\Delta z_1, \Delta z_2)$ onto eigenfunctions of the system:

$$b^\nu = \langle \psi^\nu(\zeta_1, \zeta_2) | \psi^{in}(\Delta z_1, \Delta z_2) \rangle. \qquad (5.2.23)$$

Integration of Eqs. (5.2.23) is carried out numerically using Gauss-Hermite quadrature method [23]. When probability amplitudes b^ν are known, the time-dependent wave function of the system $\psi^{t=0}(\zeta_1, \zeta_2)$ can be propagated in time analytically using Eq. (5.2.22).

5.3 Results and analysis

5.3.1 Initial state preparation

In the experiment the double-well potential is initially made asymmetric (by applying an additional field) in order to detune vibrational frequencies of two wells and effectively remove coupling between the motion of two ions. The initial states of the ions are prepared by first Doppler cooling *both* ions, with subsequent sideband cooling of only *one* of the ions. As the result, vibrational states of one ion (say #1) is in the lower vibrational state than the other ion (say #2). After that, two potential wells are brought in

resonance for time t during which ions exchange vibrational energy. After time t potential wells are brought off resonance and vibrational state of the ion #1 is measured.

In order to model this experimental procedure we have to consider states of individual ions, rather than states of the overall system. Those are appropriately described by two *local* vibration modes (rather than normal modes) and are characterized by displacement coordinates Δz_1 and Δz_2. The corresponding wave functions $\psi^{loc}(\Delta z_1)$ and $\psi^{loc}(\Delta z_2)$ are introduced, and the initial state of the system in the experiment is defined as:

$$\psi^{in}(\Delta z_1, \Delta z_2) = \psi^{loc}(\Delta z_1)\psi^{loc}(\Delta z_2). \tag{5.3.1}$$

Harmonic approximation is used to define the local mode states. The local mode harmonic frequency ω_0, same for two wells, is defined by the shape of the PES in the vicinity of the minimum:

$$\omega_0 = \frac{1}{m} \cdot \frac{\partial^2 V}{\partial z_1^2} = \frac{1}{m} \cdot \frac{\partial^2 V}{\partial z_2^2}. \tag{5.3.2}$$

In fact, this is a diagonal element of the Hessian matrix before diagonalization (see Eq. (5.2.2)). The value of ω_0 is $2\pi \times 4112.988\ kHz$ for the Be^+ and $2\pi \times 538.054\ kHz$ for the Ca^+ experiments, respectively. The initial wave function in each well is a wave packet, a linear superposition of harmonic oscillator functions $\varphi^{loc}(\Delta z)$:

$$\psi^{loc}(\Delta z_1) = \sum_i a_i \varphi_i^{loc}(\Delta z_1), \tag{5.3.3a}$$

$$\psi^{loc}(\Delta z_2) = \sum_j a_j \varphi_j^{loc}(\Delta z_2). \tag{5.3.3b}$$

This gives the initial wave function of the system, expressed as:

$$\psi^{in}(\Delta z_1, \Delta z_2) = \sum_{i,j} a_{ij} \varphi_i^{loc}(\Delta z_1) \varphi_j^{loc}(\Delta z_2), \qquad (5.3.4)$$

where $a_{ij} = a_i \cdot a_j$ are coefficients of linear combination, determined by experimental conditions. This initial wave function $\psi^{in}(\Delta z_1, \Delta z_2)$ should be projected onto accurate eigenstates of the system $\psi^v(\zeta_1, \zeta_2)$ according to Eq. (5.2.23), in order to determine the probability amplitudes b^v for the initial wave packet $\psi^{t=0}(\zeta_1, \zeta_2)$. Such projection can be easily computed, since the initial wave function expressed in the local mode coordinates is analytic. Its value can be determined at the same quadrature points in the (ζ_1, ζ_2)-space where the numeric wave function $\psi^{t=0}(\zeta_1, \zeta_2)$ should be defined.

Initial conditions of the experiment are given in terms of the mean occupation numbers for each well [19,20] that can be defined as:

$$\langle n_1 \rangle = \sum_i i \cdot a_i^2, \qquad (5.3.5a)$$

$$\langle n_2 \rangle = \sum_j j \cdot a_j^2. \qquad (5.3.5b)$$

At the initial moment of time in the Be$^+$ experiment $\langle n_1 \rangle = 0.35$ and $\langle n_2 \rangle = 2.3$, while in the Ca$^+$ experiment $\langle n_1 \rangle = 4$ and $\langle n_2 \rangle = 9$. Obviously, those values of mean occupations can be obtained with different combinations of coefficients a_i and a_j, and the experimental distributions are not known. We decided to test, by calculations, two methods of generating the initial conditions.

In the first method we chosen the *minimal* number of states to be included into the linear superposition: two states in each well, closest to the mean value. For example, to mimic the Be^+ experiment we set $a_{i=0}^2 = 0.7$ and $a_{i=1}^2 = 0.3$ in order to have $\langle n_1 \rangle = 0.35$, while we set $a_{j=2}^2 = 0.65$ and $a_{j=3}^2 = 0.35$ in order to have $\langle n_2 \rangle = 2.3$. This choice generates the following values of probability amplitudes for Eq. (5.3.3): $a_{02} = \sqrt{0.7} \cdot \sqrt{0.65}$, $a_{12} = \sqrt{0.7} \cdot \sqrt{0.35}$, $a_{03} = \sqrt{0.3} \cdot \sqrt{0.65}$, and $a_{13} = \sqrt{0.3} \cdot \sqrt{0.35}$. All other amplitudes are set to zero. The resultant distribution of the initial state populations is illustrated by Figure 5.3A.
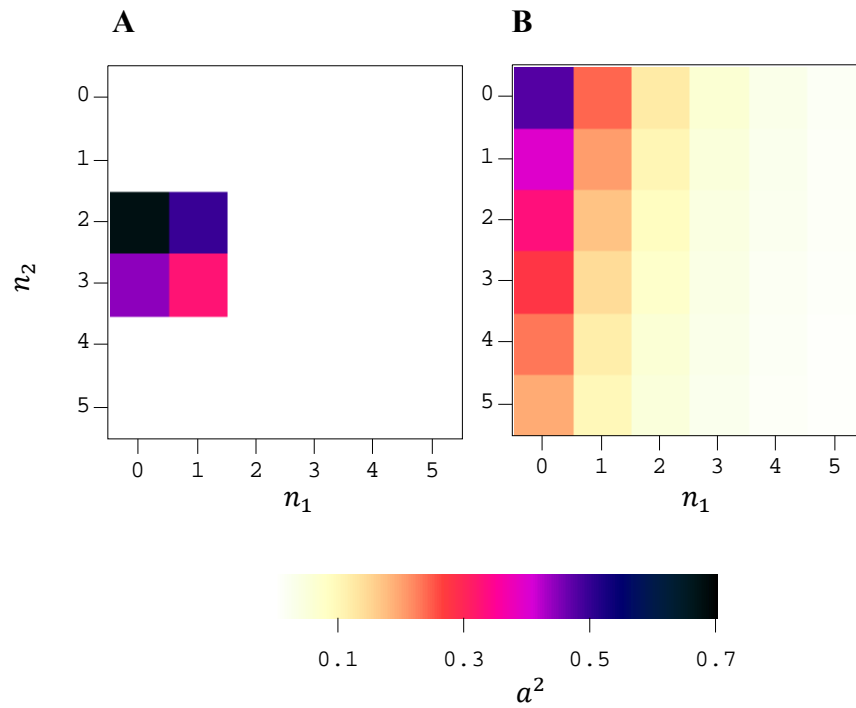
Figure 5.3: Initial populations of the local mode states in the Be^+ experiment obtained by two methods: A) superposition of small number of close-lying states; B) Boltzmann distribution of state populations.

In the second method we set up the *thermal* Boltzmann distribution of states in each well, typical to what is produced by Doppler cooling in the experiment. For the well #1:

$$a_i^2 = e^{-\frac{E_i}{kT}}/q(T), \tag{5.3.6a}$$

$$q(T) = \sum_i e^{-\frac{E_i}{kT}}, \tag{5.3.6b}$$

where E_i is the energy of the local mode state, k is Boltzmann's constant, T is thermodynamic temperature (very low in the experiment), and q is the partition function. And similar for the well #2. The value of temperature T was tuned numerically to reproduce the experimental value of the mean occupation in each well, as defined by Eqs. (5.3.5). For example, in order to mimic the Be^+ experiment we had to set $T_1 = 146\ \mu K$ for

the well #1 and $T_2 = 546\ \mu K$ for the well #2. After this, the probability amplitudes for Eq. (5.3.4) were obtained as:

$$a_{ij} = \sqrt{a_i^2 a_j^2}. \tag{5.3.7}$$

The resultant distribution of the initial state populations is illustrated by Figure 5.3B.

Comparing Fig. 5.3A *vs.* 5.3B one sees that in the second case the number of initially populated vibrational states is significantly larger, while the most populated state is less excited (in fact, it is the ground vibrational state).

Same procedures were applied to mimic the initial conditions of the Ca$^+$ experiment. First method gave $a_{40} = \sqrt{0.5}$ and $a_{09} = \sqrt{0.5}$. Second method resulted in $T_1 = 883\ \mu K$ and $T_2 = 1871\ \mu K$.

5.3.2 Wave packet analysis

At every time step we project system's wave function $\psi^t(\zeta_1, \zeta_2)$ onto the eigenfunctions of the local vibrational modes:

$$a_{ij}^t = \langle \varphi_i^{loc}(\Delta z_1)\varphi_j^{loc}(\Delta z_2)e^{-iE_{ij}t}|\psi^t(\zeta_1,\zeta_2)\rangle, \tag{5.3.8}$$

where $E_{ij} = (i + j + 1)\omega_0$ is energy of the local-mode state. From these probability amplitudes the instantaneous occupations of two wells, $\langle n_1^t \rangle$ and $\langle n_2^t \rangle$, can be computed as:

$$\langle n_1^t \rangle = \sum_i i \cdot \sum_j |a_{ij}^t|^2. \tag{5.3.9a}$$

$$\langle n_2^t \rangle = \sum_j j \cdot \sum_i |a_{ij}^t|^2. \tag{5.3.9b}$$

We performed calculations with 101 time steps up to $t = 800\ \mu s$ for the Be$^+$ experiment and up to $t = 1000\ \mu s$ for the Ca$^+$ experiment to obtain dependence of the mean occupation $\langle n_1 \rangle$ as a function of time (on resonance). Figure 5.4 compares our results with experimental data. In both experiments the value of mean occupation for one of the wells $\langle n_1 \rangle$ changes periodically with time on resonance t, which demonstrates that the ions in two wells of the double-well trap swap their vibrational energy. Importantly, the amplitude of these swaps is quite significant. For example, in the case of Be$^+$

experiment, where the initial occupations are only $\langle n_1 \rangle = 0.35$ and $\langle n_2 \rangle = 2.3$, the amplitude of the swap is close to 2, which means that ions exchange *almost all* of their vibrational energy! In the Ca^+ experiment the ions swap close to 5 quanta of energy, out of only 9 excitation quanta available in the system. Although experimental error bars are significant, particularly in the case of Be^+ experiment, the number of measurements (snapshots) is also large, which allows fitting experimental data by analytic expression (see Eq. (5.3.10) below and Appendix 1). Note that in both experiments a non-negligible heating of the system was observed, and the heating rates were measured and reported.
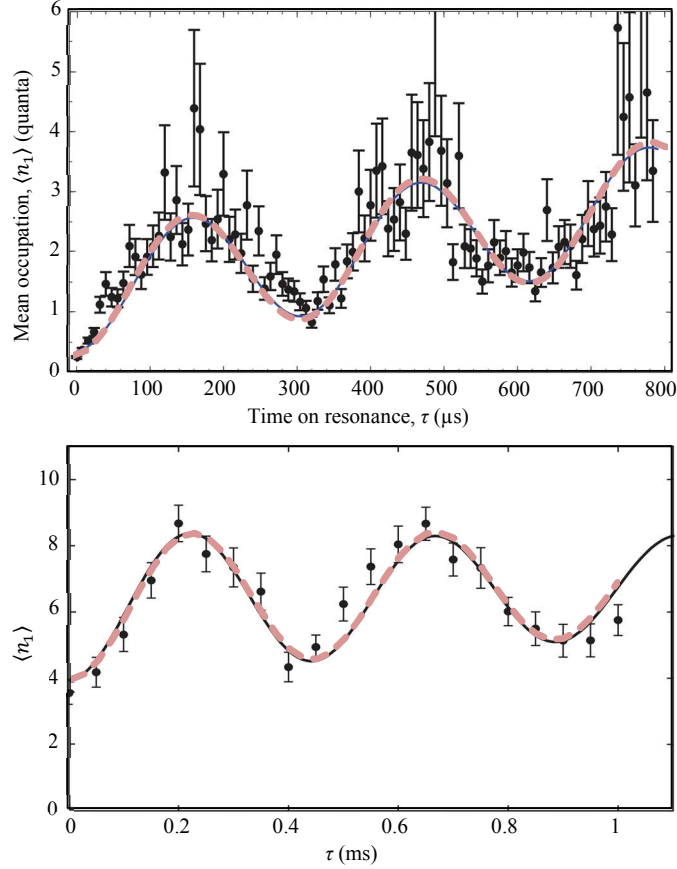
Figure 5.4: Vibrational energy swap between two ions in: A) the Be^+ experiment [19]; B) the Ca^+ experiment [20], as a function of time on resonance. Experimental error bars are indicated. Solid blue line on plot A and solid black line on plot B show the fits of experimental data. Pink dashed lines represent our computational results for each case.

We also added heating to the time-dependence of $\langle n_1^t \rangle$ presented in Fig. 5.4, in an *ad hoc* way, using experimental values of the rates, as explained in Appendix 5.1.

Figure 5.4 demonstrates that our results (dashed pink line) follow the fit of experimental data (solid black line) nearly perfectly, for both Be$^+$ and Ca$^+$ experiments. Both amplitude and frequency of the vibrational energy exchange are well reproduced. Numerical value of the energy swap time τ_{swp} for each case is reported in Table 5.1, where the experimentally measured values of this important characteristic of the process are also given. To obtain the value of τ_{swp} from our calculations we fitted the rigorously computed $\langle n_1^t \rangle$ dependence by a simple analytic expression:

$$\langle n_1^t \rangle = \langle n_1^0 \rangle \cos^2\left(\pi t / 2\tau_{swp}\right) + \langle n_2^0 \rangle \sin^2\left(\pi t / 2\tau_{swp}\right), \tag{5.3.10}$$

where the initial well occupations $\langle n_1^0 \rangle$ and $\langle n_2^0 \rangle$ and the exchange time τ_{swp} were fitting parameters. For the Be$^+$ experiment we obtained $\tau_{swp} = 155.11\ \mu s$, while for Ca$^+$

Figure 5.5: High-frequency low-amplitude oscillations of the mean occupation $\langle n_1 \rangle$ for the case of Be$^+$ experiment.

experiment we obtained $\tau_{swp} = 222.25\,\mu s$. These numbers are very close to the experimental values of $155\,\mu s$ and $222\,\mu s$, respectively.

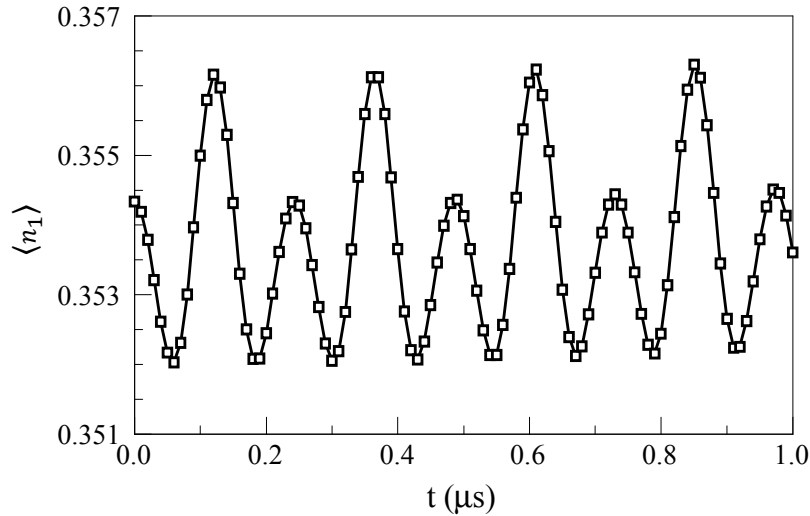Interestingly, analysis of our results revealed a feature that was not described in the experimental papers. We found that in addition to the large-amplitude small-frequency swaps discussed above (Fig. 5.4), there is also a higher-frequency lower-amplitude energy exchange process going on. This is illustrated by Fig. 5.5 for the case of Be^+ experiment.

From this picture one can see that the amplitude of this energy exchange process is only on order of 0.004 quanta, which would be impossible to identify in the experiment. The characteristic time-length of this process is $\sim 0.25\,\mu s$, which is on order of $10^{-3} \times 2\tau_{swp}$. This time-scale corresponds to the vibration period and characterizes the *intra-well* wave packet dynamics, in contrast to the *inter-well* dynamics presented in Figure 5.4. On this time scale the vibrationaly excited wave packet moves between the turning points on the PES and the real and imaginary parts of it evolve according to the phases acquired by its components.

Concerning the way of setting up the initial conditions, we found that it does not affect the energy swap dynamics, and we find that this is also quite surprising. Two types of the initial conditions illustrated by Fig. 5.3A and 5.3B lead to almost identical time-dependencies of the average occupation $\langle n_1^t \rangle$, despite the fact that the underlying dynamics, in terms of time-dependence of state occupations, is very different. Figure 6 illustrates this feature, for the case of Be^+ experiment. Here we plotted separately the contribution of every state ($i = 0, 1, 2, 3, 4$ and 5) to the average value of $\langle n_1^t \rangle$. Namely,

we plotted time evolution of different terms in the sum over i in Eq. (5.3.9a), after summation over j in each term has already been done and the result has been pre-multiplied by the value of i. Two frames of Fig. 5.6 correspond to two different initials conditions visualized by two frames of Fig. 5.3. From this analysis we see clearly that although evolutions of state populations are very different in two cases (thin lines), the overall evolutions of average occupations $\langle n_1^t \rangle$ are nearly identical. The differences we found are very small, at the level of 0.005 quanta, which is indistinguishable at the scale of Figs. 5.4 and 5.6. We did run more calculations, with various arbitrarily chosen initial conditions and they all support the following conclusion: the distribution of state-populations at the initial moment of time does not affect time evolution of the average occupation $\langle n_1^t \rangle$. However, we saw that the initial value of $\langle n_1^0 \rangle$ does affect the *amplitude* of energy swaps. This finding may have some implications for experimental studies of the process.

Figure 5.7 illustrates evolution of the accurate two-dimensional wave function of the system $\psi^t(\zeta_1, \zeta_2)$ in the Be$^+$ experiment on the time-scale of two swap times, $0 < t < 2\tau_{swp}$. The initial conditions of Fig. 5.3A are used, which gives the initial wave packet presented in Fig. 5.7A. The nodal structure of this wave packet reveals distribution of its energy over two local models, rather than normal modes. The contour lines of the PES are also shown in Fig. 5.7A (one contour line per $\hbar\omega_0$), and one can see that at this length scale the PES is nearly harmonic and symmetric. We can also see that the initial wave packet is significantly displaced from the minimum energy point. Five snapshots of $\psi^t(\zeta_1, \zeta_2)$ are shown in Fig. 5.7B. During its evolution the shape of wave function can become rather unusual and diffused, as one sees at $t = \tau_{swp}/2$ and at $t = 3\tau_{swp}/2$.
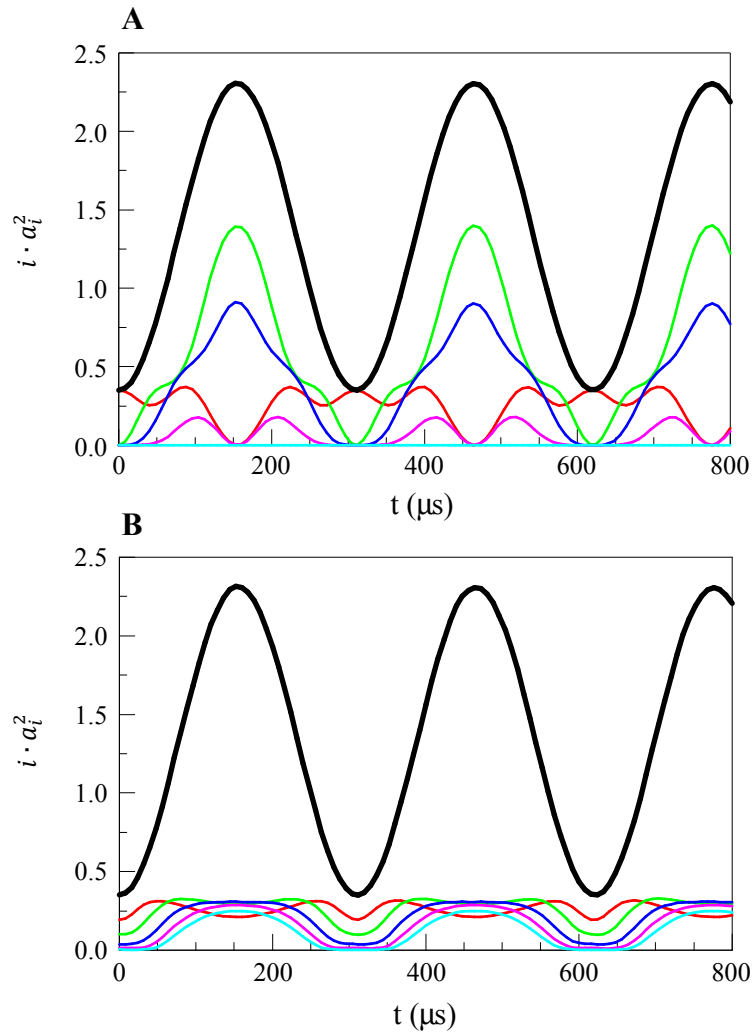
Figure 5.6: Evolution of average occupation (black) for the well #1 of the Be^+ system when the initial state was prepared by creating: A) superposition of four vibrational states; B) Boltzmann distribution of states; as indicated in Fig. 5.3. Thin colored lines represent contributions from five exited states to the mean occupation. Red, green, blue, magenta and cyan correspond to 1, 2, 3, 4 and 5 quanta of excitation, respectively.

This shape corresponds to reduction of excitation along one local mode, and increase of the excitation along the other local mode. One can notice that at $t = \tau_{swp}$ the wave function becomes simple again. It represents a mirror image of the initial wave packet and describes the state at which the local modes (or the wells) have exchanged their initial states (or excitations). At the final time $t = 2\tau_{swp}$ the wave function returns to its original shape, as excitation returns to the well #1.

In order to better represent this process we created animation of evolution of the wave packet $\psi^t(\zeta_1, \zeta_2)$ during the characteristic time τ_{swp} for the Be$^+$ experiment. The video file is available for download from Supplementary Materials [25]. Two versions of the process were visualized, that correspond to two choices of the initial conditions, as illustrated by Figs. 5.3A and 5.3B and discussed above.

Figure 5.7: A) Initial wave packet for the Be$^+$ system prepared as a superposition of small number of states, as illustrated by Fig. 5.3A. Contour lines represent the PES of the system; B) Evolution of this wave packet over the time period $2\tau_{swp}$. Snapshots of wave function are taken at the points indicated by black dots.

5.3.3 Other computational experiments

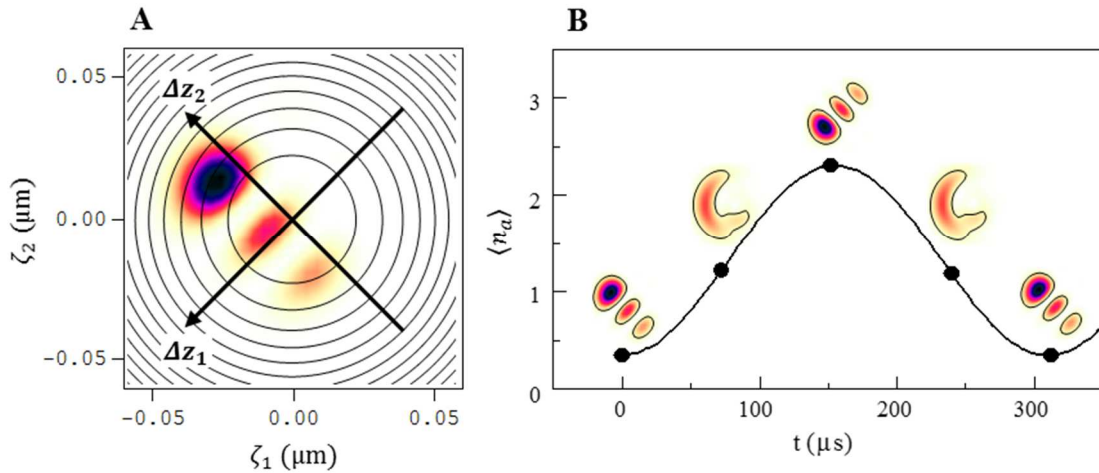Trying to identify origin of the energy swaps we carried out several additional calculations. In one of these we set up the idealized initial conditions, quite different from conditions of the experiments. Namely, we considered the double-well system in which one Be^+ ion has no excitation at all (i.e., is in the ground vibrational state $i = 0$ with $\langle n_1 \rangle = 0$ exactly) while the other ion is highly excited, but again, to an eigenstate $j = 10$ (rather than to a superposition of states), so that $\langle n_2 \rangle = 10$ exactly. By analyzing evolution of $\psi^t(\zeta_1, \zeta_2)$ we found that such choice of the initial conditions has eliminated completely the low-amplitude high-frequency oscillations of the average well populations that correspond to the intra-well dynamics (like those presented in Fig. 5.5). This makes sense, since eigenstates do not evolve in time. However, the energy swaps between the wells on the time-scale τ_{swp} have survived, and, in this case we observed a complete transfer of 10 quanta of excitation from one well to the other, and back. Animation of a rather impressive wave packet dynamics for this case is also available from the Supplementary Materials [25]. This demonstrates that the choice of initial conditions has no fundamental influence on the energy swaps.

In the second computational experiment we eliminated the effect of *anharmonicities* in the system. For this we replaced the accurately computed spectrum and wave functions by those obtained from the normal mode analysis. This is equivalent to approximating the PES by a 2D paraboloid, a harmonic system with two normal mode frequencies ω_1 and ω_2 and analytic wave functions. In this case we still observed the inter-well energy swaps, characterized by basically the same value of τ_{swp}. This also

makes sense since, as one can see from Table 5.3, the values of vibrational anharmonicities in the system are negligible, even when compared to the relatively small frequency splitting: $\Delta \approx \delta\omega \times 10^{-3}$, where $\delta\omega \approx \omega_{1,2} \times 10^{-3}$.

Finally, we eliminated the effect of *frequency splitting* $\delta\omega$ by setting $\omega_1 = \omega_2 = \omega_0$, using the corresponding degenerate energy spectrum and exactly the same wave functions for both normal modes, which is equivalent to approximating the PES by a paraboloid of revolution. This last change has, finally, shut-off the inter-well energy swaps.

Trying to understand this result we computed evolution of a Gaussian wave packet for two cases mentioned above: a perfectly symmetric well ($\omega_1 = \omega_2$) and a weakly asymmetric well ($\omega_1 \neq \omega_2$). In each case the shape of the initial Gaussian was equivalent to the ground vibrational state, while the displacement off the equilibrium position was chosen to give $\langle n_1 \rangle = 0$ exactly and a large value of $\langle n_2 \rangle \sim 12$. This is illustrated by Fig. 5.8, where the initial position of the Gaussian wave packet is in the upper left corner, on the axis Δz_2 (compare to Fig. 5.7A). Again these conditions are quite different from the

experiment, but they result in a simple dynamics which allows seeing the underlying principle.

Figure 5.8A explains evolution of such wave packet in the case of a symmetric well ($\omega_1 = \omega_2$). The wave packet starts in the upper left corner, moves to the center of the well, then climbs up to the turning point (lower right corner), where it is reflected. Since the PES is perfectly round in this case, the wave packet is reflected straight back

(along the diameter) and returns exactly to its initial location. This cycle repeats again and again, and the wave packet stays on the Δz_2 infinitely long. No motion along Δz_2 occur, which means that no energy is transferred to the other well, and the value of $\langle n_1 \rangle = 0$ remains unchanged.

Figure 5.8B explains evolution of the same initial Gaussian wave packet in the case of an asymmetric well with $\omega_1 < \omega_2$. Asymmetry of the contour lines of the PES is exaggerated in Fig. 5.8B, for the purpose of clarity only. Importantly, the initial wave packet will follow the gradient of the PES, and its trajectory will start deviating from the axis Δz_2, simply because in the case of $\omega_1 \neq \omega_2$ the contour lines are ovals, rather than circles (compare Figs. 5.8A and 5.8B). When the wave packet comes to its first turning point (in the lower right corner) it will be reflected towards its initial position, but, not quite. Notice that at the turning point the contour line of the PES is not perpendicular to the momentum vector. Even if you think classically (angle of incidence equals to the angle of reflection) you come to conclusion that the wave packet will not return to its original position, but to a slightly different point. Namely, its new position will be slightly below the axis Δz_2, which corresponds to some motion along Δz_1, which also means some increase of $\langle n_1 \rangle$ and some energy transfer to the other well.
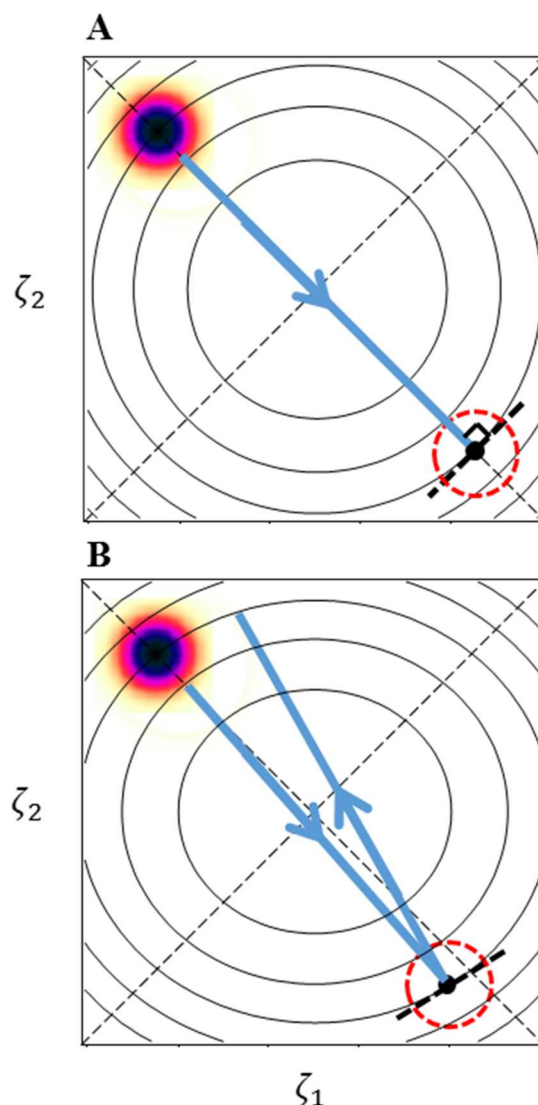
Figure 5.8: Explanation of the Gaussian wave packet dynamics in the cases of: A) a perfectly symmetric well with $\omega_1 = \omega_2$; and B) an asymmetric well with $\omega_1 \neq \omega_2$. Contour lines of the PES are shown schematically by thin lines. The local mode axis Δz_1 and Δz_2 are indicated by dashed lines along the diagonals of the (ζ_1, ζ_2)-space of the normal mode coordinates (compare to Fig. 5.7A). The initial wave packet is shown by color. Red dashed circle shows the wave packet at the time of its reflection at the turning point. Upper frame illustrates that trajectory of the wave packet remains restricted to the diagonal line (the axis Δz_2) because the contour lines are perpendicular to the incidence vector. Lower frame shows that trajectory does not follow the axis Δz_2, due to potential gradient, and, when reflected back, does not return to the initial point.

Notice that each reflection gives the wave packet some angular momentum with respect to the origin $\Delta z_1 = \Delta z_2 = 0$. As time goes the trajectory evolves from a nearly straight line (along axis Δz_2 at the initial moment of time) into an elliptic orbit in the $(\Delta z_1, \Delta z_2)$-space, with longer principal axis positioned along Δz_2, and the shorter axis positioned along Δz_1. Figure 5.8B suggests that the wave packet follows this orbit in the counter clockwise direction. When the time reaches $t = \tau_{swp}/2$ the orbit becomes perfectly circular, after which it starts losing the angular momentum (again, due to the classical reflection principle), which transforms it into an elliptic orbit, but now with longer principal axis positioned along Δz_1, and the shorter axis positioned along Δz_2. When the time reaches $t = \tau_{swp}$ this ellipse degenerates into a nearly straight line along Δz_1 (because all the angular momentum is lost), which corresponds to a complete energy transfer to the other well. Then the process plays back, with wave packet rotating clockwise. In order to make this description of the process clear we created animation of the Gaussian wave packed dynamics for the case $\omega_1 \neq \omega_2$. It is also available from the Supplemental Material [25].

Since the frequency difference in the system is very small, $\delta\omega \approx \omega_{1,2} \times 10^{-3}$, the asymmetry of the PES is also very small. One reflection of the wave packet makes very little change. It takes more than 10^3 reflection cycles to "turn" the trajectory by 90 degrees, from the axis Δz_2 at $t = 0$ to the axis Δz_1 at $t = \tau_{swp}$, which means that the energy transfer is, in fact, *very inefficient*. Importantly, all this dynamics can be understood based on the classical principle: the angle of incidence equals to the angle of reflection. No tunneling phenomenon is involved in the explanation of the process.

5.4 Conclusions

We developed a rigorous computational treatment for quantum dynamics of cold ions in a double-well trap using a numerically accurate approach, without making any assumptions concerning the coupling strength between the ions, and without involving the harmonic approximation for energy spectrum of the system. The goal was to reproduce, from first principles, a process of energy swaps between the wells observed in the experiments at NIST [19] and Innsbruck [20]. The model parameters were carefully chosen to reproduce experimental observables. Vibrational anharmonicities (due to Coulomb interaction and a strongly anharmonic trapping potential) were accurately computed and were found to be very small, which is explained by small amplitude of the vibrational motion of ions. Experimental results of both NIST and Innsbruck groups were reproduced in detail. In addition, new insight was provided by analysis of wave packet motion and time-evolution of state populations.

The most surprising result is interpretation of energy swaps. Such phenomena are often explained by the tunneling splitting $\delta\omega$, but we feel that involvement of the tunneling into interpretation of the process is quite artificial, if not to say misleading, because the potential barrier between the wells is very high, the distance between the wells is almost macroscopic, and the ions are heavy. In contrast, we showed that the energy swaps are, basically, a classical phenomenon. They can be understood using the principle of trajectory reflection. Rigorous solution of time-dependent Schrodinger equation supports this interpretation.

The model developed in this work can be used to study theoretically/computationally the new experiments at NIST [26,27]. It can also help explore opportunities for coherent and optimal control of the ionic motion in the double-trap architectures [28,29].

Appendix 5.1: Calculation of energy swap frequency with perturbation theory

In the experiments at NIST [19] and Innsbruck [20] the frequency of the vibrational energy swap between the ions with mass m and electric charge q at resonance was predicted using the expression:

$$\Omega_{swp} = \frac{q^2}{4\pi\varepsilon_0 d^3 m\omega_0},$$
(A5.1.1)

where d is distance between the ions, ω_0 is motional frequency and ε_0 is the permittivity of free space. The swap frequency Ω_{swp} is also related to the splitting between the frequencies of vibrational normal modes of the system:

$$\Omega_{swp} = \frac{1}{2}(\omega_2 - \omega_1).$$
(A5.1.2)

Here we demonstrate the derivation of the Eq. (A5.1.1) by using the perturbation theory to find splitting $\omega_2 - \omega_1$.

First we consider the full potential of the system as a sum of two harmonic potentials of each well and a Coulomb term:

$$V(x_1, x_2) = \frac{1}{2}k_0 x_1^2 + \frac{1}{2}k_0 x_2^2 + \frac{\gamma}{d + x_1 - x_2},$$
(A5.1.3)

where $x_{1,2}$ are displacements of the ions and we use the notations $k_0 = m\omega_0^2$ and $\gamma = q^2 / 4\pi\varepsilon_0$.

Expanding the Coulomb term in Eq. (A5.1.3) in Taylor series and truncating it after first three terms we will obtain:

$$\frac{\gamma}{d + x_1 - x_2} \approx \frac{\gamma}{d}\left(1 + \frac{x_2 - x_1}{d} + \frac{x_1^2 + x_2^2}{d^2} - \frac{2x_1 x_2}{d^2}\right). \qquad \text{(A5.1.4)}$$

Combining Eq. (A5.1.3) and (A5.1.4) we can obtain:

$$V(x_1, x_2) = \frac{1}{2}k(x_1 - \delta)^2 + \frac{1}{2}k(x_2 + \delta)^2 - \frac{2\gamma}{d^2}x_1 x_2 + U, \qquad \text{(A5.1.5)}$$

where $k = k_0 + {}^\gamma/_{2d^3}$, $\delta = {}^\gamma/_{kd^2}$ and the constant term $U = {}^\gamma/_d - k\delta^2$.

The full Hamiltonian of the system is then

$$H = T + V_0 + V', \qquad \text{(A5.1.6a)}$$

$$T = -\frac{\hbar^2}{2m}\left(\frac{d^2}{dx_1^2} + \frac{d^2}{dx_2^2}\right), \qquad \text{(A5.1.6b)}$$

$$V_0 = \frac{1}{2}k(x_1 - \delta)^2 + \frac{1}{2}k(x_2 + \delta)^2, \qquad \text{(A5.1.6c)}$$

$$V' = -\frac{2\gamma}{d^2}x_1 x_2. \qquad \text{(A5.1.6d)}$$

We can consider Hamiltonian in Eq. (A5.1.6a) as a sum of the Hamiltonian of the unperturbed system $H_0 = T + V_0$ and the perturbation term V'. H_0 is the Hamiltonian of the two-dimensional harmonic oscillator with known eigenfunctions and energy spectrum. The eigenfunctions of H_0 are:

$$\varphi_{ij}(x_1, x_2) = \varphi_i(x_1)\varphi_j(x_2), \qquad \text{(A5.1.7)}$$

where $\varphi_i(x_1)$ and $\varphi_j(x_2)$ are calculated accordingly to Eq. (5.2.12).

The energy spectrum of the system of two harmonic oscillators is

$$E_{ij} = \hbar\omega\left(i + \frac{1}{2}\right) + \hbar\omega\left(j + \frac{1}{2}\right), \tag{A5.1.8}$$

where i and j is the number of quanta of excitation in each well.

The first order correction for the ground state energy can be calculated as following:

$$V_{00} = \langle\varphi_{00}|V'|\varphi_{00}\rangle. \tag{A5.1.9}$$

From Eq. (A5.1.7) the unperturbed wave function of the ground state is

$$\varphi_{00}(x_1, x_2) = \varphi_0(x_1)\varphi_0(x_2) = A_0^2 e^{-\frac{\beta}{2}(x_1-\delta)^2} e^{-\frac{\beta}{2}(x_2+\delta)^2}, \tag{A5.1.10}$$

where we use notations $A_0 = \sqrt[4]{m\omega/\pi\hbar}$ and $\beta = m\omega/\hbar$. Combining Eq. (A5.1.9) and (A5.1.10) we will obtain

$$V_{00} = -\frac{2\gamma A_0^4}{d^3}\int x_1 e^{-\beta(x_1-\delta)^2}dx_1 \int x_2 e^{-\beta(x_2+\delta)^2}dx_2. \tag{A5.1.11}$$

The first integral in Eq. (A5.1.11) can be solved after substitution $z = x_1 - \delta$:

$$\int x_1 e^{-\beta(x_1-\delta)^2}dx_1 = \int (z+\delta)e^{-\beta z^2}dz =$$

$$= \int_{-\infty}^{\infty} z e^{-\beta z^2}dz + \delta \int_{-\infty}^{\infty} e^{-\beta z^2}dz. \tag{A5.1.12}$$

The first integral in Eq. (A5.1.12) equals zero as it is an integral over an odd function with symmetric borders and the second integral is the Gaussian integral and equals $\sqrt{\frac{\pi}{\beta}}$. The final result of integration is

$$\int x_1 e^{-\beta(x_1-\delta)^2} dx_1 = \delta\sqrt{\frac{\pi}{\beta}}. \qquad (A5.1.13)$$

In a similar manner we can solve the second integral in Eq. (A5.1.11) and obtain

$$\int x_2 e^{-\beta(x_2+\delta)^2} dx_2 = -\delta\sqrt{\frac{\pi}{\beta}}. \qquad (A5.1.14)$$

From Eq. (A5.1.13) – (A5.1.14) we determine that $V_{00} = 0$ so the perturbation V' does not change the ground state energy of the system.

The first two excited states of the system are degenerate according to Eq. (A5.1.8):

$$E_{10} = E_{01} = 2\hbar\omega. \qquad (A5.1.15)$$

Therefore we need to apply the perturbation theory in case of degenerate levels. For that we consider the wave function of the system as a linear superposition of the eigenfunctions of the two degenerate levels:

$$\psi = a\psi_1 + b\psi_2, \qquad (A5.1.16)$$

where a and b are constant coefficients and the eigenfunctions $\psi_{1,2}$ can be calculated from Eq. (A5.1.7):

$$\psi_1(x_1, x_2) = \varphi_{10}(x_1, x_2) = \varphi_1(x_1)\varphi_0(x_2) =$$

$$= A_1(x_1 - \delta)e^{-\frac{\beta}{2}(x_1-\delta)^2} A_0 e^{-\frac{\beta}{2}(x_2+\delta)^2}, \qquad (A5.1.17a)$$

$$\psi_2(x_1, x_2) = \varphi_{01}(x_1, x_2) = \varphi_0(x_1)\varphi_1(x_2) =$$

$$= A_0 e^{-\frac{\beta}{2}(x_1-\delta)^2} A_1(x_2 + \delta)e^{-\frac{\beta}{2}(x_2+\delta)^2}, \qquad (A5.1.17b)$$

where $A_1 = A_0\sqrt{2\beta} = \sqrt[4]{4m^3\omega^3/\pi\hbar^3}$.

Schrodinger's equation can then be written as

$$(H_0 + V' - E)(a\psi_1 + b\psi_2) = 0, \qquad (A5.1.18)$$

where E is the energy of the degenerate states in the presence of perturbation V'.

Projection of Eq. (A5.1.18) onto the functions ψ_1 and ψ_2 leads to the system of two linear equations:

$$(H_{11} - E)a + H_{12}b = 0, \qquad (A5.1.19a)$$

$$H_{12}a + (H_{22} - E)b = 0, \qquad (A5.1.19b)$$

where H_{ij} are the elements of the Hamiltonian matrix, $H_{ij} = \langle\psi_i|H_0|\psi_j\rangle$. We can rewrite H_{ij} as following:

$$H_{11} = V_{11} + E_0, \quad H_{22} = V_{22} + E_0, \quad H_{12} = V_{12}, \quad H_{21} = V_{21}, \qquad (A5.1.20)$$

where V_{ij} are the elements of the perturbation matrix, $V_{ij} = \langle\psi_i|V'|\psi_j\rangle$.

Combining Eq. (A5.1.19) – (A5.1.20) we can find the values of energy E from the determinant

$$\begin{vmatrix} V_{11} + E_0 - E & V_{12} \\ V_{21} & V_{22} + E_0 - E \end{vmatrix} = 0. \tag{A5.1.21}$$

For solving Eq. (A5.1.21) we need to calculate elements of the perturbation matrix. For V_{11} we will obtain:

$$V_{11} = \langle \psi_1 | V' | \psi_1 \rangle =$$

$$= -\frac{2\gamma A_0^2 A_1^2}{d^3} \int_{-\infty}^{\infty} x_1(x_1 - \delta)^2 e^{-\beta(x_1 - \delta)^2} dx_1 \int_{-\infty}^{\infty} x_2 e^{-\beta(x_2 + \delta)^2} dx_2. \tag{A5.1.22}$$

The second integral in Eq. (A5.1.22) equals $-\delta \sqrt{\frac{\pi}{\beta}}$ (see Eq. (A5.1.14)) and the first integral can be solved with substitution $x_1 - \delta = z$:

$$\int_{-\infty}^{\infty} x_1(x_1 - \delta)^2 e^{-\beta(x_1 - \delta)^2} dx_1 = \int_{-\infty}^{\infty} z^2(z + \delta) e^{-\beta z^2} dz =$$

$$= \int_{-\infty}^{\infty} z^3 e^{-\beta z^2} dz + \delta \int_{-\infty}^{\infty} z^2 e^{-\beta z^2} dz. \tag{A5.1.23}$$

The first integral in Eq. (A5.1.23) equals to zero and the second integral is a known Gaussian integral:

$$\int_{-\infty}^{\infty} z^2 e^{-\beta z^2} dx_1 = \frac{1}{2\beta} \sqrt{\frac{\pi}{\beta}}. \tag{A5.1.24}$$

Combining Eq. (A5.1.22) – (A5.1.24) we obtain:

$$V_{11} = \frac{\gamma A_0^2 A_1^2}{d^3} \delta^2 \frac{\pi}{\beta^2}. \tag{A5.1.25}$$

Similarly for V_{22} we will obtain:

$$V_{22} = \langle \psi_2 | V' | \psi_2 \rangle = \frac{\gamma A_0^2 A_1^2}{d^3} \delta^2 \frac{\pi}{\beta^2} = V_{11}. \tag{A5.1.26}$$

For V_{12} we will obtain:

$$V_{12} = \langle \psi_1 | V' | \psi_2 \rangle = \iint A_0 e^{-\frac{\beta}{2}(x_1 - \delta)^2} A_1 (x_2 + \delta) e^{-\frac{\beta}{2}(x_2 + \delta)^2} \left(-\frac{2\gamma}{d^3} x_1 x_2 \right) \times$$

$$\times A_1 (x_1 - \delta) e^{-\frac{\beta}{2}(x_1 - \delta)^2} A_0 e^{-\frac{\beta}{2}(x_2 + \delta)^2} dx_1 dx_2 =$$

$$= -\frac{2\gamma}{d^3} A_0^2 A_1^2 \int_{-\infty}^{\infty} x_1 (x_1 - \delta) e^{-\beta(x_1 - \delta)^2} dx_1 \int_{-\infty}^{\infty} x_2 (x_2 + \delta) e^{-\beta(x_2 + \delta)^2} dx_2. \tag{A5.1.27}$$

The first integral in Eq. (A5.1.27) can be solved with substitution $x_1 - \delta = z$ and using Eq. (A5.1.24):

$$\int_{-\infty}^{\infty} x_1 (x_1 - \delta) e^{-\beta(x_1 - \delta)^2} dx_1 = \int_{-\infty}^{\infty} z(z + \delta) e^{-\beta z^2} dx_1 =$$

$$= \int_{-\infty}^{\infty} z^2 e^{-\beta z^2} dx_1 + \delta \int_{-\infty}^{\infty} z e^{-\beta z^2} dx_1 = \frac{1}{2\beta} \sqrt{\frac{\pi}{\beta}}. \tag{A5.1.28}$$

Similarly for the second integral in Eq. (A5.1.27) we can obtain:

$$\int_{-\infty}^{\infty} x_2 (x_2 + \delta) e^{-\beta(x_2 + \delta)^2} dx_2 = \frac{1}{2\beta} \sqrt{\frac{\pi}{\beta}}. \tag{A5.1.29}$$

Combining Eq. (A5.1.27) – (A5.1.29) we will obtain:

$$V_{12} = -\frac{\gamma A_0^2 A_1^2}{d^3} \frac{\pi}{2\beta^3}. \tag{A5.1.30}$$

For V_{21} we will obtain:

$$V_{21} = \langle \psi_2 | V' | \psi_1 \rangle = \langle \psi_1 | V' | \psi_2 \rangle = V_{12}. \tag{A5.1.31}$$

Now we can rewrite the determinant from Eq. (A5.1.21) using Eq. (A5.1.25) – (A5.1.25) and (A5.1.30) – (A5.1.31):

$$\begin{vmatrix} V_{11} + E_0 - E & V_{12} \\ V_{12} & V_{11} + E_0 - E \end{vmatrix} = 0. \tag{A5.1.32}$$

$$E^2 - 2E(V_{11} + E_0) + (V_{11} + E_0)^2 - V_{12}^2 = 0. \tag{A5.1.33}$$

$$E_{1,2} = E_0 + V_{11} \pm V_{12}. \tag{A5.1.34}$$

The energy difference is therefore

$$E_2 - E_1 = 2|V_{12}| = 2\frac{2q^2}{4\pi\varepsilon_0 d^3} \frac{m\omega_0}{\pi\hbar} \frac{\pi\hbar^2}{2m^2\omega_0^2} = 2\hbar \frac{q^2}{4\pi\varepsilon_0 d^3 m\omega_0}, \tag{A5.1.35}$$

and the frequency splitting is

$$\omega_2 - \omega_1 = \frac{E_2 - E_1}{\hbar} = 2\frac{q^2}{4\pi\varepsilon_0 d^3 m\omega_0} = 2\Omega_{swp}. \tag{A5.1.36}$$

Thus we obtained frequency of vibrational energy swap from Eq. (A5.1.1).

We obtained the result for frequency splitting using Taylor expansion of the Coulomb potential, which we truncated after second order terms in Eq. (A5.1.4). We also

looked at the effect of higher order terms (up to fourth order) of the value of frequency splitting. The perturbation potential becomes:

$$V' = \frac{\gamma}{d^4}(x_2^3 - x_1^3) + \frac{3\gamma}{d^4}(x_1^2 x_2 - x_2^2 x_1) + \frac{\gamma}{d^5}(x_2^4 + x_1^4)$$

$$+ \frac{6\gamma}{d^5}x_1^2 x_2^2 + \frac{4\gamma}{d^5}(x_1^3 x_2 - x_2^3 x_1). \qquad (A5.1.37)$$

Using the same procedure as described above we can obtain

$$E_2 - E_1 = 2|V_{12}| = \Delta E \cdot \frac{3\delta}{d}\left(1 - \frac{2\delta}{d}\right), \qquad (A5.1.38)$$

where ΔE is splitting from Eq. (A5.1.35). Here we can use the fact that distance between the ions is much larger than ion displacement from Coulomb interaction. With this condition, $d \gg \delta$, the energy splitting in Eq. (A5.1.38) becomes zero. Thus we can conclude that energy correction from higher order terms in Taylor expansion of the Coulomb potential is negligible.

Appendix 5.2: Including the heating rates of the trap

In the Be$^+$ experiment at NIST [19] the vibrational energy exchange between the wells was accompanied by a linear growth of the mean occupation with time, due to heating of the ions. This heating was included in the expression that was used to fit the experimental data as follows:

$$\langle n_1^t \rangle_{\text{exp}} = \langle n_1^0 \rangle \cos^2\left(\Omega_{\text{swp}}t\right) + \langle n_2^0 \rangle \sin^2\left(\Omega_{\text{swp}}t\right) + \langle \dot{n} \rangle t, \qquad (A5.2.1)$$

where $\langle \dot{n} \rangle$ is the heating rate, same for both wells, $\Omega_{\text{swp}} = \pi/2\tau_{\text{swp}}$ is experimental swap frequency. The fit of experimental data was done with four free parameters: the initial average occupations of two wells $\langle n_1^0 \rangle$ and $\langle n_2^0 \rangle$, the exchange frequency Ω_{swp} and the heating rate $\langle \dot{n} \rangle$. The value of the heating rate obtained from the fit was $\langle \dot{n} \rangle = 1,885$ quanta per second.

In our calculations the heating of the ions can't be directly included in the time propagation of the wave function of the system. But we could mimic the experiment by computing:

$$\langle n_1^t \rangle_{\text{exp}} = \langle n_1^t \rangle + \langle \dot{n} \rangle t, \qquad (A5.2.2)$$

where $\langle n_1^t \rangle$ is the result of our calculations without heating, as defined by Eq. (5.3.9a) and fitted by Eq. (5.3.10), and $\langle \dot{n} \rangle$ is the experimental heating rate. This moiety, $\langle n_1^t \rangle_{\text{exp}}$, was computed and presented in Fig. 5.4A for comparison with experimental results.

Likewise, the heating of the ions was observed in the Ca$^+$ experiments in Innsbruck [20] with the heating rate of $\langle \dot{n} \rangle = 1.3$ quanta per millisecond. But in addition,

their data were also affected by exponential damping of the energy swap efficiency with time. Their fitting expression included both these factors as follows:

$$\langle n_1^t \rangle_{\text{exp}} = \langle n_1^0 \rangle + \frac{1}{2}(\langle n_2^0 \rangle - \langle n_1^0 \rangle)(1 - \cos(2\Omega_{\text{swp}}t))e^{-t/\tau_{\text{dmp}}} + \langle \dot{n} \rangle t, \quad (\text{A5.2.3})$$

where τ_{dmp} is the damping constant. The value of this parameter obtained from the fit of experimental data was $\tau_{\text{dmp}} = 3\ ms$.

Expression (A5.2.3) can be rewritten as follows:

$$\langle n_1^t \rangle_{\text{exp}} = \langle n_1^0 \rangle + (\langle n_2^0 \rangle - \langle n_1^0 \rangle)\sin^2(\Omega_{\text{swp}}\tau)\,e^{-t/\tau_{\text{dmp}}} + \langle \dot{n} \rangle \tau =$$

$$= (\langle n_1^0 \rangle \cos^2(\Omega_{\text{swp}}t) + \langle n_2^0 \rangle \sin^2(\Omega_{\text{swp}}t))e^{-t/\tau_{\text{dmp}}} +$$

$$\langle n_1^0 \rangle(1 - e^{-t/\tau_{\text{dmp}}}) + \langle \dot{n} \rangle \tau. \quad (\text{A5.2.4})$$

From Eq. (A5.2.4) we see that we can take into account both damping and heating terms as follows:

$$\langle n_1^t \rangle_{\text{exp}} = \langle n_1^t \rangle\, e^{-t/\tau_{\text{dmp}}} + \langle n_1^0 \rangle\left(1 - e^{-t/\tau_{\text{dmp}}}\right) + \langle \dot{n} \rangle t. \quad (\text{A5.2.5})$$

Again, here $\langle n_1^t \rangle$ is the result of our calculations without heating, as defined by Eq. (5.3.9a) and fitted by Eq. (5.3.10), while $\langle \dot{n} \rangle$ is the experimental heating rate and τ_{dmp} is the experimental damping constant. This moiety $\langle n_1^t \rangle_{\text{exp}}$ corresponds to the Innsbruck experiment. It was presented in Fig. 5.4B for comparison with experimental results.

References for Chapter 5

1. D. J. Larson, J. C. Bergquist, J. J. Bollinger, W. M. Itano and D. J. Wineland, Phys. Rev. Lett. **57**, 70 (1986).

2. J. I. Cirac and P. Zoller, Phys. Rev. Lett. **74**, 4091 (1995).

3. R. Blatt and D. Wineland, Nature **453**, 1008 (2008).

4. H. Häffner, C. F. Roos and R. Blatt, Phys. Rep. **469**, 155 (2008).

5. J. D. Jost *et al*, Nature **459**, 683 (2009).

6. R. Islam *et al*, Nature Commun. **2**, 377 (2011).

7. K. Kim *et al*, New J. Phys. **13**, 105003 (2011).

8. A. Steane, Appl. Phys. B **64**, 623 (1997).

9. S. Gulde *et al*, Nature **421**, 48 (2003).

10. D. Leibfried *et al*, Nature **422**, 412 (2003).

11. J. Benhelm, G. Kirchmair, C. F. Roos and R. Blatt, Nat. Phys. **4**, 463 (2008).

12. J. P. Home *et al*, Science **325**, 1227 (2009).

13. D. J. Wineland, Phys. Scr. **2009**, 014007 (2009).

14. D. Hanneke *et al*, Nat. Phys. **6**, 13 (2012).

15. J. I. Cirac and P. Zoller, Nature **404**, 579 (2000).

16. D. Kielpinski, C. Monroe and D. Wineland, Nature **417**, 709 (2002).

17. J. M. Amini *et al*, New J. Phys. **12**, 033031 (2010).

18. C. Monroe and J. Kim, Science **339**, 1164 (2013).

19. K. R. Brown *et al*, Nature **471**, 196 (2011).

20. M. Harlander, R. Lechner, M. Brownnutt, R. Blatt and W. Hansel, Nature **471**, 200 (2011).

21. L. Wang and D. Babikov, Phys. Rev. A **83**, 022305 (2011).

22. L. Wang and D. Babikov, Phys. Rev. A **83**, 052319 (2011).

23. W. Press, S. Teukolsky, W. Vetterling and B. Flannery, *Numerical recipes in Fortran 90* (Cambridge University Press, New York, 1996).

24. E. Anderson, Z. Bai, C. Bischof, S. Blackford, J. Demmel, J. Dongarra, J. Du Croz, A. Greenbaum, S. Hammarling, A. McKenney and D. Sorensen, *LAPACK Users' Guide* (Society for Industrial and Applied Mathematics, Philadelphia, 1999).

25. See Supplemental Material at [URL] for animations of the wave packet dynamics in the Be^+ double-well experiment.

26. T. R. Tan, J. P. Gaebler, R. Bowler, Y. Lin, J. D. Jost, D. Leibfried, and D. J. Wineland, Phys. Rev. Lett. **110**, 263002 (2013).

27. A. C. Wilson, Y. Colombe, K. R. Brown, E. Knill, D. Leibfried and D. J. Wineland, Nature **512**, 57 (2014).

28. M. Zhao and D. Babikov, Phys. Rev. A **77**, 012338 (2008).

29. L. Wang and D. Babikov, J. Chem. Phys. **137**, 064301 (2012).

Summary

For practical realization of quantum information processing we need a quantum system that provides reliable preparation of the initial state, high-fidelity quantum gate operations, error tolerance, readout of the result of quantum computation and scalability of the system to increase the number of qubits. In this work we show how these requirements can be addressed for molecular quantum computer.

In our computational study of quantum information processing with thiophosgene molecule we investigated the gateway scheme of control of transitions between the vibrational states of the molecule. In this scheme qubits are encoded in highly excited vibrational states of the molecule chosen from the energy spectrum and without focusing on particular normal modes of vibration. State-to-state transitions are only allowed through the intermediate "gateway" state in B electronic state, so the transitions can be controlled with UV/vis laser pulses. This scheme of control also provides reliable preparation of the initial state [Mol. Phys. **105**, 1999 (2007)].

Fault-tolerant quantum computing requires 0.9999 fidelity of each quantum gate to enable quantum error correction algorithms. We demonstrated that such high-fidelity gates are possible to achieve in molecular quantum computer using the gateway scheme in thiophosgene molecule. We applied OCT optimization to obtain a shape of a laser pulse in time domain that performs CNOT gate with high fidelity.

We demonstrated error tolerance of the optimal pulse with respect to pulse modifications in frequency domain. We showed that the same high fidelity of optimal pulse can be achieved with the pulse prepared with only 64 frequency channels with

resolution 2 cm^{-1}, which is typical for the experiment. We found that small errors in amplitudes and phases of frequency components do not affect gate fidelity drastically.

We explored the process of readout of quantum information from vibrational qubits in thiophosgene molecule using quantum beat spectroscopy. In this approach the final superposition of qubit states is excited to a single readout state in B electronic state with time-delayed Gaussian pulses. The detected fluorescence from the readout state exhibits quantum beats, e.g. oscillations that depend on the time delay of the readout pulse. By fitting the quantum beat signal we can extract the information about the populations of the qubit states and the phase differences between them.

We found that fitting the quantum beat signal allows us to obtain populations of the qubit states with high precision. However we discovered the non-negligible phase error. The analysis of this error showed that it comes from the fact that the standard fitting expression does not account for non-zero duration of the readout pulse. We proposed a new fitting expression that includes the phase correction term and showed that we can fit quantum beat signals very accurately with the corrected expression.

The problem of scalability of molecular quantum computer could be addressed by using trapped molecular ions instead of neutral molecules. The initial step towards this approach is to study dynamics of the system of trapped atomic ions. We studied coupling between atomic ions trapped in separated wells of double-well potential which is a key feature for scalable quantum computation.

The experiments with the system of two atomic ions trapped in a double-well potential demonstrated vibrational energy exchange between the ions [Nature **471**, 196

(2011), Nature **471**, 200 (2011)]. We developed rigorous computational treatment to study quantum dynamics of this system. We successfully reproduced the vibrational energy exchange observed in the experiments. We also studied the time evolution of the wave packets of the system and showed how the energy transfer can be explained in terms of wave packet dynamics in an asymmetric potential.

Combining the advantages of molecular quantum computer with the achievements in the field of ion traps could allow using trapped molecular ions for quantum information processing. In this approach we could use multiple vibrational states of each molecular ion for encoding quantum information, be able to access individual molecular ions and control interaction between them.